Spin-Orbit Coupling and Magnetism in Multilayer Graphene

Omslag: ©lupobianco/Masterfile

PhD thesis, Utrecht University, the Netherlands (2013).
Printed by Ipskamp Drukkers BV.
ISBN: 978-94-6191-734-8

Spin-Orbit Coupling and Magnetism in Multilayer Graphene

Spin-Baan Interacties en Magnetisme in Meerlaags Grafeen
(met een samenvatting in het Nederlands)

Proefschrift

ter verkrijging van de graad van doctor aan de Universiteit Utrecht op gezag van de rector magnificus, prof.dr. G.J. van der Zwaan, ingevolge het besluit van het college voor promoties in het openbaar te verdedigen op vrijdag 7 juni 2013 des middags te 4.15 uur

door

Ralph van Gelderen

geboren op 8 juni 1985 te Dordrecht

Promotor: Prof.dr. C. Morais Smith

Dit proefschrift werd mogelijk gemaakt met financiële steun van de Nederlandse Organisatie voor Wetenschappelijk Onderzoek (NWO).

Publications

This thesis is based on the following publications:

- R. van Gelderen and C. Morais Smith, *Rashba and intrinsic spin-orbit interactions in biased bilayer graphene*, Phys. Rev. B **81**, 125435 (2010).
- D. Makogon, R. van Gelderen, R. Roldán, and C. Morais Smith, *Spin-density-wave instability in graphene doped near the van Hove singularity*, Phys. Rev. B **84**, 125404 (2011).
- R. van Gelderen, L.-K. Lim, and C. Morais Smith, *Spin and band ferromagnetism in trilayer graphene*, Phys. Rev. B **84**, 155446 (2011).
- R. Olsen, R. van Gelderen, and C. Morais Smith, *Ferromagnetism in ABC-stacked trilayer graphene*, Phys. Rev. B **87**, 115414 (2013).
- R. van Gelderen, R. Olsen, and C. Morais Smith, *Screening in multilayer graphene*, Arxiv:1304.5501 (2013).

Contents

Chapter 1

Introduction

In 2004 a discovery was made that many thought to be impossible [1]. In the 1930's, Landau and Peierls established that strictly two-dimensional crystals are unstable [2, 3]. Thermal fluctuations should be so large in these systems, that the atoms get displaced over distances larger than the interatomic distance, ruining the crystal structure. Mermin and Wagner extended these arguments 30 years later and the theorem stating that in one- and two-dimensional systems continuous symmetries cannot be broken is named after them [4, 5]. In particular, translational symmetry cannot be broken for such systems. Therefore atoms cannot arrange themselves in periodic patterns, i.e. crystal structures cannot form.

Although the Mermin-Wagner theorem was proven mathematically a long time ago, experimentally the field of low dimensional systems has always been thriving. It were Konstantin Novoselov and André Geim, together with their group in Manchester, who found the first truly two-dimensional material: *Graphene*. They used a process called the *micromechanical exfoliation method*, i.e. using adhesive tape to peel off a one-atom-thick layer of carbon from graphite, also known as the Scotch-tape method. After this achievement, the field of graphene exploded, resulting in almost $15,000$ papers with the word graphene in the title among many different branches of science. Close to 9000 of these articles cited the fundamental work of Novoselov and Geim and in 2010 they were awarded the Nobel Prize in Physics for their achievement. In this first Chapter, a qualitative introduction on and a brief history of graphene is given, in order to explain the reader what this material is and why it is so special. For a more mathematical description of graphene, the reader is referred to Chapter 2.

1.1 One-atom-thick carbon layer

There exist several materials that consist of pure carbon. Fullerenes and carbon nanotubes are two examples, but the two most well-known pure carbon materials

are diamond and graphite. The difference between these two materials is the way the carbon atoms arrange themselves (crystal structure). In diamond, the four valence electrons of the carbon atoms hybridize into four sp^3 orbitals, after which they form covalent sigma bonds with electrons on neighboring atoms. Since there are no free electrons left, diamond is an insulator. In graphite on the other hand, only three electrons hybridize (into three sp^2 orbitals). These three electrons form sigma bonds with electrons on neighboring atoms, while the remaining valence electron (p_z orbital) forms a much weaker pi bond. When the sigma bonds are formed in this way, a crystal structure is created in which the atoms are located in a plane and where all angles are 120°. This is called a *honeycomb lattice* (see Fig. 1.1a). When these planes stack on top of each other, graphite is formed, because neighboring layers bind by the Van der Waals force (see Fig. 1.1b). This force is much weaker than the covalent bonds and therefore the planes slide easily off one another. This atomic structure explains how a pencil works: The graphite in your pencil is dragged along the paper and since the carbon layers slide off easily they stick to the paper. The electrons in the pi bonds become delocalized and graphite is conducting within the planes. The electronic band structure of graphite is such that the conduction and valence bands overlap, making graphite a semimetal.

Graphene is obtained from graphite by isolating a single plane. Putting it the other way around, graphite is nothing more than stacked graphene layers. Since a graphene plane is only one atom thick, this material is truly two-dimensional. The two-dimensionality of graphene makes that the electrons behave very differently than in graphite. As is shown in Chapter 2, a few stacked graphene planes also behave as a 2D system. Few-layer graphene is different than both graphite and a single layer of graphene.

Not only graphene [1], but also single layers of other crystals were isolated [6] by the group in Manchester. The electronic properties of the graphene samples were of such high quality however, that these other monolayer materials were mostly ignored. It is not unthinkable that they will get their share of attention in the near future.

Although there are some doubts that the Mermin-Wagner theorem is applicable for graphene systems [7], the general believe is that graphene is stable because it can ripple in the third dimension [8, 9]. Such rippling, which leads to a gain in elastic energy and a suppression of the thermal vibrations, was indeed observed in freely suspended (i.e. not on a substrate) graphene [9]. However, for most purposes these ripples can be ignored and graphene can be described as a two-dimensional honeycomb lattice of carbon atoms, where the atoms are separated by a distance $a = 1.42$ Å. This lattice constant is considerable smaller than the interplane distance in graphite, which equals $d = 3.4$ Å, reflecting the stronger covalent inplane bonds compared with the weaker Van der Waals force between

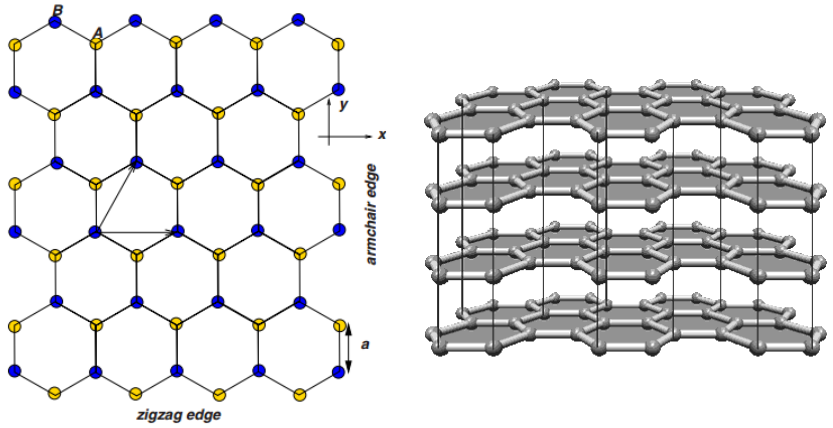

(a) (b)

Figure 1.1: (a) Honeycomb lattice with two types of edges (zigzag/armchair). Sublattices are coded by color (blue/yellow). Figure extracted and edited from Ref. [10]. (b) Graphite consists of layers of graphene stacked upon each other. Picture from Ref. [11].

the planes.

Experimentalists did try to grow single layer graphene before 2004, but only graphite films thicker than 100 layers were found [12], or samples were investigated using surface techniques like scanning tunnel microscope (STM) and were never tested on electronic or transport properties [13, 14, 15]. The major achievement in 2004 was not only the production of monolayers which do only weakly interact with the underlying substrate, but also finding a way to detect them. Mechanical exfoliation results in many small flakes of few-layered graphene. To detect a single layer fragment with, for example, a scanning tunneling microscope (STM) is almost impossible, because it takes too much time to scan a typical sample (1 cm^2) for the tiny ($\sim \mu$m) one-layered flakes produced. The possibility to detect monolayers of graphene with an optical microscope was the real breakthrough. One monolayer of graphene absorbs roughly 2.3% of the incoming light in very broad frequency domain and this percentage increases linearly with the number of layers [16]. Although this opens up the possibility to distinguish optically between flakes with different numbers of layers, the substrate used is critical. As Geim and Novoselov explain in a status update on graphene, written two years after its realization [17], a difference of 5% in the thickness of the SiO_2 substrate (315 nm instead of 300 nm) can render a graphene monolayer invisible. Later, other methods were found to identify easily the number of layers in graphene samples, for example Raman spectroscopy [18, 19] and contrast spectroscopy [20], which

uses the difference in the reflection spectra of white light that graphene samples with a different number of layers on a SiO_2 substrate exhibit.

1.2 Graphene electronics

There were many layered materials already known and soon after the realization of graphene it turned out to be possible to make 2D crystals out of them using the same techniques [6]. Nevertheless, the academic community mostly ignored these results and focussed en masse on graphene. There are a few good reasons why graphene drew so much more attention.

First of all, the very high quality of the graphene crystals. Even the micrometer sized flakes obtained by the Scotch-tape method exhibit very good electronic transport properties. In the pioneering article [1] mobilities up to $10,000$ cm^2/V·s were obtained at room temperature. These mobilities are to a great extend insensitive to electron doping levels and chemical doping [17, 21]. Although an intrinsic limit of $200,000$ cm^2/V·s for the mobility in graphene was claimed to exist in 2008 [22], there have been measurements on suspended graphene samples at low temperatures finding mobilities of $230,000$ cm^2/V·s [23] and even as large as 10^6 cm^2/V·s [24], depending on the electron doping level. At room temperature it is now possible to reach mobilities over $100,000$ cm^2/V·s [25], beating InSb, the semiconductor with the highest mobility known ($77,000$ cm^2/V·s).

In semiconductor physics, high mobility leads in general to better device performance. Since silicon based electronics is reaching its limits, people search for alternatives. Graphene is a very promising material to improve electronic circuits in the near future, due to its good conductance. However, it is characterized as a *zero-gap semiconductor*, with which is meant that the conduction and the valence bands touch, resulting in some disadvantages for electronic devices, e.g. it is very hard to make transistors out of graphene. The point where the conduction and valence bands touch is called the *Dirac point*, *charge neutrality point*, or K point. Usually one defines this point to be at zero energy. If the system is filled up to this point, it is exactly half filled which means one free electron per carbon ion, hence the system is charge neutral. Naively, one would expect the conductivity to vanish at exactly half filling, but it turns out that graphene has a minimum conductivity in the order of e^2/h [26]. Due to the rippling of graphene it is impossible to make the graphene locally charge neutral. Electron and hole puddles will form and they allow for current to flow [27].

This nonzero conductivity is a disadvantage for electronic applications. Nevertheless, it is now possible to produce graphene transistors with a cutoff frequency as high as 100 GHz [28], to produce electrodes with very high surface area and very low resistance [29], and progress has been made into fast rechargeable batteries

which could potentially be used in electric cars [30]. The fact that graphene is almost transparent and a good conductor makes it perfect for touchscreens, not only replacing the rare and expensive indium tin oxide (ITO), but also allowing the screens to be flexible [31]. These are only a few examples of graphene's applications and although there are a lot of difficulties in realizing these applications, very fast progress has been made in the last decade and there is little doubt that graphene devices will become commercially favorable to produce. These many applications explain the graphene research boom and the Nobel Prize for Geim and Novoselov in 2010.

1.3 Fundamental physics

There is more, however. Also for fundamental physics there is a lot that graphene has to offer. It is due to the honeycomb lattice that the conduction and valence bands touch each other in reciprocal space. If one expands the energy spectrum around these Dirac points, it becomes clear that this crossing is linear [10]. Hence, for graphene systems, which are around half filling, the energy of the electrons scales linearly with their momentum, making them behave as massless relativistic Dirac fermions. However, the slope of the dispersion, which is the velocity the electrons move with, is 300 times smaller than the speed of light. Low-energy electrons in graphene are described by the massless Dirac equation instead of the Schödinger equation. This is due to an additional pseudo-spin degree of freedom, connected to the honeycomb lattice structure. The honeycomb lattice has two atoms per unit cell. The two sublattices can not be connected by a lattice vector, as can be seen in Fig. 1.1a. It is obvious that the two lattice sites are geometrical inequivalent by looking at the position of the nearest neighbors. They are placed in a triangle either pointing north or pointing south. The sublattice structure makes the electrons behave as chiral particles, i.e. there is a pseudo-spin quantum number (sublattice index), which is coupled to the momentum of the particle. Hence, there is a similarity between graphene and quantum electrodynamics (QED) for massless

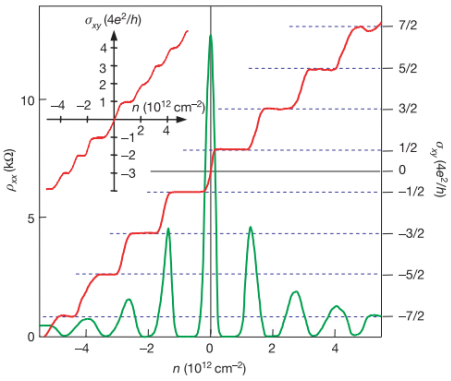

Figure 1.2: Integer anomalous quantum Hall effect in monolayer graphene for a magnetic field $B = 14$T and at a temperature $T = 4$K. Figure extracted from Ref. [26].

fermions [32]. However, the unusual properties of QED show up at much lower speeds in graphene.

An interesting consequence of the chirality of the electrons in graphene is that they can tunnel through a classically impenetrable barrier with probability one. This is called the Klein paradox. It is due to the fact that chirality is linked with momentum and also a conserved quantity. Therefore, depending on the incident angle, the electrons cannot scatter back and pass through the barrier [33, 34].

The two-dimensional nature of graphene allows for the realization of the integer quantum Hall effect. Because of the presence of both electron and holes in combination with the valence and conduction bands touching, the integer quantum Hall effect in graphene is unconventional. Unconventional in the sense that all plateaus are shifted by half an integer of the conduction quantum away from zero with respect to the quantum Hall effect in conventional 2D electron gases [26, 35]. This shift is explained by the presence of a Landau level at zero energy, which is half filled with electrons for a charge-neutral system. Hence, if one starts out with undoped graphene and fill up the zero-energy Landau level with electrons, the first plateau in the transverse conductance will show up at one half times the conductance quantum. The conductance quantum in graphene is $4e^2/h$. The factor four comes from a twofold spin degeneracy combined with a twofold valley degeneracy. The concept of valley degeneracy is explained in more detail in Chapter 2, but basically comes from the fact that the conduction and valence bands touch at two inequivalent points in reciprocal space. Because of the massless relativistic charge carriers and low scattering in graphene, the quantum Hall effect can be observed at room temperature (300 K) at a magnetic field of $B = 29$ T [36]. The energy of the Landau levels scales with $\sqrt{B}$ [26]. This is unique for a single layer of graphene and can be used to identify monolayers.

If a system exhibits the integer quantum Hall effect, the next natural question to ask is whether the fractional quantum Hall effect (FQHE) also occurs. This phenomena is driven by interactions and for a long time it was unclear whether the massless chiral electrons are correlated enough to form composite fermions, resulting in quantum Hall plateaus at fractional filling factors. Recently, the groups of Eva Andrei and Philip Kim independently observed a quantum Hall plateau in the conductivity for a filling factor of $1/3$ in ultraclean suspended graphene samples [37, 38].

Another particularity of a finite-sized graphene sample is that, due to the honeycomb lattice structure, the edges of a sample can terminate in different ways. The most common ones are the *zigzag* edge and the *armchair* edge. They behave very differently. Zigzag edges allow for spin polarized edge states, while armchair edges do not [10]. The dispersion of these edge states can be tuned by potentials applied on the boundary [39].

These are only a few examples of the interesting physics that graphene has

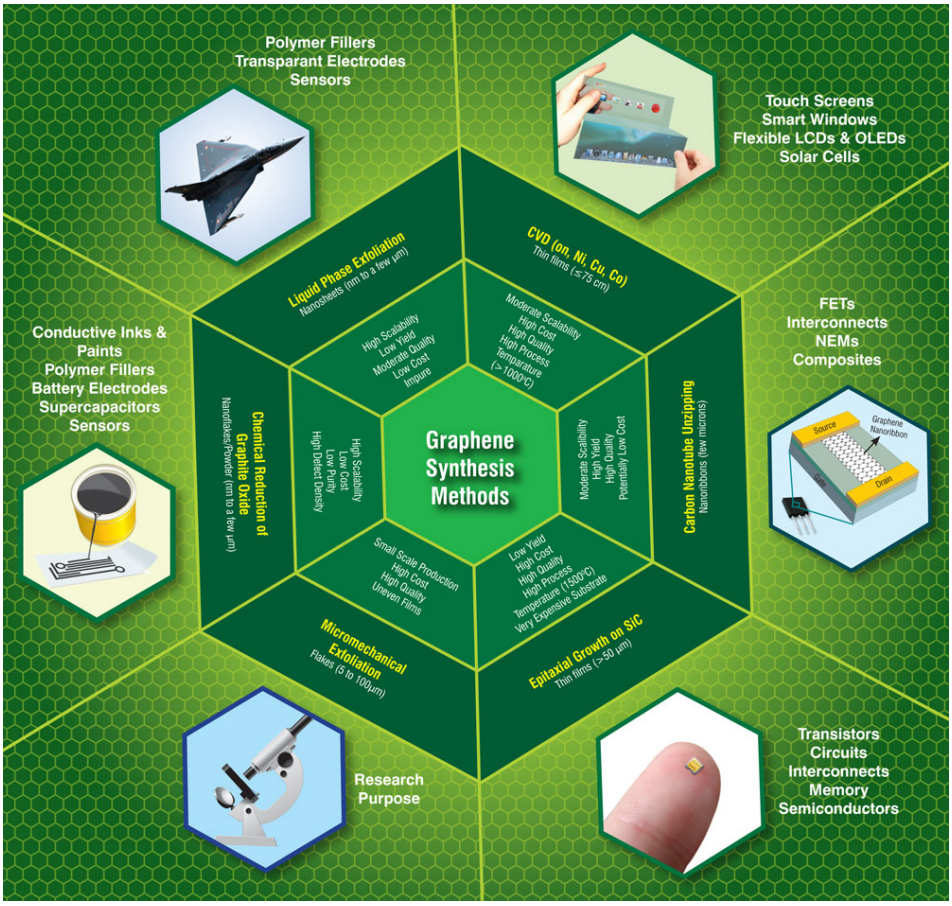

Figure 1.3: Overview of production methods for graphene and its applications. Picture extracted from Ref. [40].

to offer. There are many more and for more qualitative examples the reader is referred to Ref. [17]. A very broad quantitative review of many phenomena in graphene, some of which are also discussed in Chapter 2 of this thesis, is given in Ref. [10].

1.4 Production methods

It is easy to create single-layer graphene by using the Scotch tape method, but the drawback is that the flakes found are typically micrometer sized. For most applications much larger samples are needed. Since 2004, the search for macroscopic samples has resulted in several methods for producing graphene; the two

most important of these are discussed in the following. In Fig. 1.3 an overview is shown of the different production methods, the advantages and disadvantages, and the (possible) applications.

Chemical vapor deposition

The method that produces the largest graphene sheets to date is chemical vapor deposition (CVD). Graphene is grown on transition metals (e.g. Ruthenium, Iridium, Cobalt, Nickel, Platinum, Copper) via thermal decomposition. In this process, a metal substrate and a gas of hydrocarbons (usually methane), are heated to 1000° Celsius at low pressures. The hydrocarbons decompose and the carbon atoms are deposited on the metal. When the metal is cooled, these carbon atoms form graphene on the metal surface. After dissolving the metal surface, the graphene can be deposited on another substrate [41]. Some promising results have been obtained by growing graphene on Nickel [42, 43, 44], but large scale production has been realized with chemical vapor deposition on copper [45]. First, samples of several square centimeters and mobilities around 4000 $cm^2/V{\cdot}s$ were realized [46]. Not much later, a 30 inch graphene film was grown on flexible copper foil, after which it was successfully moved to a different substrate (by dissolving the copper), and a working graphene-based touchscreen panel was produced [31]. These samples have sheet resistances comparable with usual ITO touchscreens, and transparencies are over 97%. The half-integer quantum Hall effect was observed, indicating that the sample is indeed mainly a monolayer. In fact, since the process is self-terminating, over 95% is a monolayer of carbon atoms, independent of growth time or heating and cooling rates [45, 46].

Epitaxial growth on silicon carbide

Epitaxial growth is the process where a carbon rich material is heated to $1200 - 2000°$ Celsius, such that the non-carbon atoms desorb from the system and the carbon forms a graphene lattice (*epitaxy*: Growing a crystal layer of one mineral on the crystal base of another mineral in such a manner that its crystalline orientation is the same as that of the substrate). Silicon carbide (SiC) is very well suited for this type of graphene fabrication, but the end result depends heavily on the production details [47, 48, 49, 50].

Graphene can be grown on the silicon-terminated (SiC(0001)) face and on the carbon-terminated ($SiC(000\bar{1})$) face of SiC. For graphene on the Si-terminated face, the first layer grown interacts very strongly with the substrate. This layer is called the zeroth- or buffer-layer. The zeroth layer has no observable energy bands on its own [50]. The bonding with the substrate induces an energy gap and this layer does not contribute to transport properties. Moreover, it decouples the next layer(s) from the substrate. If an additional layer is grown, one can observe the linear

spectrum of graphene by angle resolved photoemission spectroscopy (ARPES), while for two additional layers a parabolic spectrum, characteristic for a graphene bilayer (as discussed below), is present [50]. It is also possible to intercalate the sample with hydrogen. By doing so, the hydrogen atoms bond with the substrate and the buffer layer decouples, creating quasi-free standing graphene [51].

Graphene films grow much faster on the C-side of the SiC crystal. Additional layers orient themselves in a way that is unique. Subsequent layers are rotated within a distribution of angles, which is very different than the usual stacking configurations of multilayer graphene. Although the rotation angle between the layers can appear random, it was shown that the stacking is in fact highly ordered [50].

Other methods

There are several other methods for producing graphene. Some of them may be interesting for future applications. They include unzipping of carbon nanotubes [52], reduction of graphite oxide [53], and ball milling pristine graphite [54]. The field is still developing fast and the success of the different production methods will be determined by scalability and applicability.

1.5 Multilayer graphene

When monolayers of graphene could be constructed, a natural step was to see what happens if you stack these single layers onto each other. It is evident that at some point you create graphite, but it turns out that few-layer graphene systems behave in a way that is different from both a monolayer and graphite. Although a system of, for example, two layers of graphene (bilayer) is no longer strictly two-dimensional, it can be treated as if it is. In general, electrons can jump between the different layers of the system, but the momenta with which we describe these

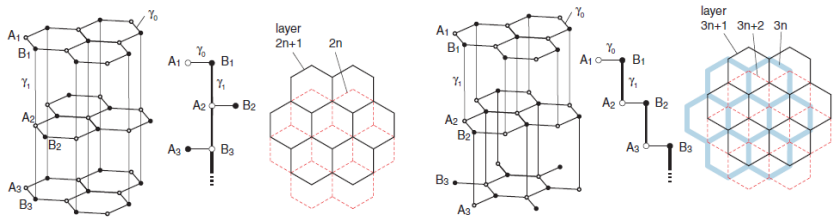

Figure 1.4: (a) Bernal (ABA) and (b) rhombohedral (ABC) stacked graphene multilayer. Picture extracted from Ref. [55].

Stacking 1		Stacking 2		Stacking 3	
Bottom	Top	Bottom	Top	Bottom	Top
A	A	A	HC	A	B
B	B	B	A	B	HC
HC	HC	HC	B	HC	A
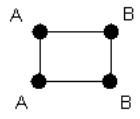		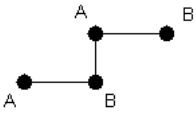		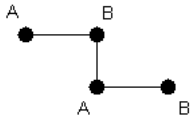	

Table 1.1: Three different stacking possibilities. The table indicates which points of the lattice are placed on top of each other. HC indicates the honeycomb center.

electrons have components only in the plane. The exact behavior of the electrons (the dispersion) depends on how the different layers are stacked.

Although it is possible to stack two layers of graphene onto each other with a relative orientation that is random (named the *twisted bilayer*) [56], usually an additional layer on a graphene sample can orient itself in three different ways with respect to the layer beneath it. Recall that the honeycomb lattice has two atoms per unit cell and therefore has two (triangle) sublattices, namely the A (yellow) en B (blue) lattice sites in Fig. 1.1a. The orientation of nearest neighbors of a particular lattice site determines whether it is part of the A or B sublattice and the convention chosen is assumed to be the same in all layers. The honeycomb centers (HC) are also points of rotational symmetry. The three ways of stacking are shown in Table. 1.1

In the first stacking of Table. 1.1, the two layers are placed exactly on top of each other. This is energetically unfavorable compared to the other two stackings and is rarely seen in experiment. Natural grown few-layer graphene, most often, stacks itself in configuration two or three. The A (or B) sublattice of the top layer is on top of the B (or A) sublattice of the layer beneath it and the remaining lattice sites lie opposite to a honeycomb center. For bilayer graphene these two stackings are equivalent, since in that case they are related by mirror symmetry. For a multilayer system, however, it is very important how the layers are oriented and is convenient to look at the orientation with respect to the first layer, which by definition has orientation `A` (not to be confused with sublattice A). If a subsequent layer is stacked according to "stacking 1" it has configuration `A` as well. If a next layer has "stacking 2" with respect to the bottom one, we define it to have orientation `B`, if it has "stacking 3", again with respect to the bottom layer, it is defined to have orientation `C`. Although the stacking pattern of a multilayer graphene system could have a random order, there are two configurations very

dominantly present in experiment and they have gotten a separate name. There is *Bernal* stacking (or AB-stacking) in which all the odd and all the even layers have the same orientation, hence the configurations of the layers is `ABAB`.... There is also *rhombohedral* (or ABC stacked) graphene, which has a cyclic structure through the three different orientation (`ABCA`...). The two configurations are schematically drawn in Fig. 1.4. Note that for bilayers there is no difference between the two, since the difference comes in the orientation of the third layer. In the literature the bilayer is referred to as Bernal (or AB) stacked.

Bilayer graphene

The most common form of multilayer graphene is the (Bernal stacked) bilayer. The unit cell contains four lattice sites instead of two, as was the case for monolayer graphene. Next to the usual sublattice index, there is a layer index and it is natural to label the (sub)-lattice sites in bilayer graphene as A_1, B_1, A_2, and B_2. The A_2 sites are located on top of the B_1 sites, while the remaining A_1 and B_2 sites do not have a direct neighbor in the other layer ("stacking 2" in Table. 1.1). With four atoms per unit cell there will be four energy bands, instead of the two in monolayer graphene. In a first approximation, the electrons can hop to nearest neighbors only, both to neighbors in the same plane, as to direct neighbors in the other plane, hence between B_1 and A_2 sites. The electronic orbitals of these two 'dimer' sites are coupled together by an interlayer hopping energy ($t_\perp \approx 0.3$ eV) which is roughly ten times smaller than the inplane hopping energy ($t \approx 3$ eV). This dimerization is responsible for the fact that two of the energy bands are shifted away from the Dirac point (see Fig. 1.5). The low-energy physics takes place on the sites that do not have a direct neighbor in the opposite layer. It is possible (see Chapter 2) to construct an effective low-energy model that takes into account the hopping between A_1 and B_2 sites. This hopping is not a direct one. It encounters two inplane hoppings (from A_1 to B_1 and later from A_2 to B_2) and one interplane hopping (from B_1 to A_2). An inplane hopping contributes a factor $v_F p$, where p is momentum and the Fermi velocity $v_F = (3/2)at$ is related to inplane hopping and the lattice constant a. The transition between the B_1 and A_2 dimer sites gives the electrons an effective mass $m \sim t_\perp$. In the interplane hopping process no momentum factor comes in, because the sites lie exactly on top of each other and the momentum of the electrons is

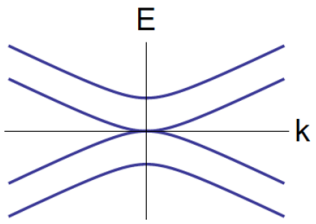

Figure 1.5: Sketch of the dispersion of bilayer graphene. The energy bands are parabolic close to the Dirac point, but become linear for momenta further away from the K point.

two-dimensional. In Chapter 2, more details will be provided, but for now it is plausible that the effective hopping between A_1 and B_2 sites will give a dispersion $E = \pm p^2/(2m)$, where $m = t_\perp/(2\hbar v_F)^2$, hence a parabolic spectrum. One has to be aware that the dispersion relation becomes linear again for momenta further away from the Dirac point (see Fig. 1.5). Nevertheless, this quadratic dispersion makes the quasi-particles in bilayer graphene a totally new species, namely *massive chiral fermions*. The particles are massive because of the quadratic dispersion and chiral because, for low energies, the pseudo-spin structure (related to sublattice index) is still present. Since the pseudo spin is related to two lattice sites on different layers, i.e A_1 and B_2, it is equally valid to say that chirality is a code for layer index. Recall that for chiral electrons the pseudo-spin is coupled to the momentum, i.e. for every momentum the pseudo-spin vector points in a certain direction.

There are many more features that distinguish bilayer graphene from its single-layer counterpart. The zero energy Landau level has an extra degeneracy, shifting the plateaus of the transverse conductivity in the integer quantum Hall effect by half an integer times the conductance quantum [57, 58, 59]. Moreover, if one rotates an electron adiabatically around the Dirac point in k-space, the electron wave function can acquire a phase $\exp(i\phi)$. This phase ϕ is called the Berry phase. For monolayer graphene $\phi = \pi$, but for bilayer graphene $\phi = 2\pi$ [57]. A very important property of bilayer graphene is the possibility to open a gap of a few hundred meV at the Dirac point by creating a voltage difference between the layers [60]. This makes bilayer graphene a *tuneable-gap semiconductor*. All these properties together make bilayer graphene a completely other system than monolayer graphene and therefore a very different material.

Trilayer graphene

There are two natural ways to place a third layer on top of a (Bernal) bilayer. The third layer can have the same orientation as the first, creating ABA-stacked trilayer graphene, or it can have the third possible orientation, resulting in ABC-stacked trilayer graphene. The orientation of the third layer makes an enormous difference.

ABC-stacked trilayer graphene (in general any ABC-stacked multilayer) belongs to the same family as bilayer graphene. Of course, ABC-stacked trilayer graphene has its own particularities, but there are also quite some characteristics that are generalizations of monolayer and bilayer graphene. In the following discussion electrons that hop between next-nearest neighbors are still ignored.

Due to the dimerization of electronic orbitals belonging to lattice sites that lie directly opposite to each other and the corresponding energy shift accompanying this effect, the low-energy physics takes place on the outer layers. In the convention

used here, this are the A_1 and B_3 sublattice sites. With a similar reasoning as was performed in the bilayer section, one can argue that the low-energy dispersion should behave as $E \sim (\hbar v_F p)^3/t_\perp^2$, i.e. the energy dispersion is cubic (it is p^N for an N-layered ABC-stacked sample). The Berry phase of these electrons turns out to be $\phi = 3\pi$ ($N\pi$ for an N-layer system) [61], it is possible to open a gap by applying a bias voltage between the layers, and the degeneracy of the zero-energy Landau level is now three times the one of graphene [62] (N times for N-layered ABC systems). Although these examples might give the indication that ABC-stacked trilayers are fairly easy to describe, this is not necessarily true. For example, the full Hamiltonian of the ABC-stacked trilayer is no longer analytically diagonalizable. Moreover, if one abandons the simplified assumptions that electrons can only hop between nearest neighbors, the graphene trilayer has more possible next-nearest-neighbor hopping parameters than the bilayer has [63, 64], making it a more complex, but also a much richer system.

The ABA-stacked trilayer system behaves very differently. There are three sublattice sites (A_1, B_2, and A_3) that have no neighbor in opposite layers. It is possible, through a change of basis, to bring the Hamiltonian in block diagonal form, where the blocks are the monolayer Hamiltonian and a bilayer Hamiltonian with a modified interlayer hopping constant [65]. These blocks are uncoupled as long as the mirror symmetry in the middle plane is preserved, i.e no next-nearest-neighbor hopping between the planes or an external voltage is present. As a consequence, there are two energy bands at the Dirac point, both a linear one and a parabolic one. Hence, there are both massless and massive quasi-particles. An interesting result of this band structure, among others, is that the Landau levels of ABA-stacked trilayer graphene cross as a function of the magnetic field [66]. In an ABA-stacked graphene trilayer a gap is not easily opened when a bias voltage is applied [67], in contrast to its ABC-stacked counterpart.

More than three layers

When adding more layers, the different stacking possibilities grow exponentially. A theoretical study of mixed stacking structures, i.e. an interplay between Bernal and rhombohedral stacking, has recently been performed by Koshino and McCann [55]. It was found that it is possible to create a wide variety of linear bands, parabolic bands and bands of higher order. Fully Bernal and rhombohedral stacked multilayers behave quite similar as their trilayer relatives. For Bernal stacked multilayers, the Hamiltonian can be brought in block form. For an even number of layers $2N$ this results in N bilayer blocks, and therefore N parabolic bands at the Dirac point, all with a different prefactor (effective mass). For an odd number of layer $2N + 1$, an additional monolayer block is present and, as a consequence, an additional linear-dispersive energy band is observed with the same slope as in

monolayer graphene [66].

It has to be pointed out that if one includes the next-nearest-neighbor hopping parameters of the so called Slonczewski-Weiss-McClure (SWMc) model [63, 64], the energy spectra are much more complicated. The conduction and valence bands do overlap. By increasing the number of layers, the two-dimensional nature of the sample will at some point be lost and the system will behave very much like graphite. It is estimated that few layer graphene becomes graphite if the number of layers is in the order of 10 [68]. Note that the screening length in graphite is only 5 Å [69, 70], which is less than two times the interplane distance. One has to distinguish between the surface and the bulk in interacting systems for multilayered systems as thin as five layers [17].

1.6 Magnetic properties

In this thesis the focus is put on magnetic properties of monolayer, bilayer, and trilayer graphene. The topics covered include magnetic phase transitions in highly doped monolayer graphene (Chapter 3), the effect of spin-orbit interactions on the energy dispersion in bilayer graphene (Chapter 4), ferromagnetism due to long-range Coulomb interaction in both ABA-stacked (Chapter 5) and ABC-stacked (Chapter 6) trilayer graphene, and the effect of screening in N-layer graphene (Chapter 7).

Magnetic graphene would be an ideal material for spintronics. Therefore, experimentalists put a lot of effort in achieving such an accomplishment. It is possible to construct high pseudo magnetic fields by applying strain to graphene [71, 72], which can be uniform and (at least theoretically) can induce a quantum Hall effect [73]. In 2003 ferromagnetism was observed at room temperature in highly oriented pyrolytic graphite (HOPG) irradiated with high-energy photons [74]. It was realized that the ferromagnetism is two-dimensional in nature, it can be induced by point defects or by hydrogen chemisorption [75] and therefore it should also manifest itself in graphene. It was shown that point defects induce magnetic moments in graphene, but under the experimental condition used it was not yet possible to achieve any magnetic ordering [76].

Ferromagnetism is caused by a quantum mechanical effect called the *exchange interaction*. Due to the fermionic nature of the electrons, it can be favorable to align their spins and as a consequence, due to the Pauli exclusion principle, distribute them further apart from each other. This reduces electrostatic energy and this ferromagnetic state, where the spins are aligned, could become the ground state of the system. Suppose however that the two electrons had the same momentum before the spin flip. This can no longer be the case in the ferromagnetic configuration, because the Pauli exclusion principle would be violated. Therefore,

the spin-flipped electron has to have a higher momentum and therefore a higher kinetic energy. If this increase in kinetic energy is larger than the gain in electrostatic energy, it is no longer favorable for the system to magnetize. It depends on the energy-momentum relation and the exact form and strength of the interaction (can be modified by screening) whether the paramagnetic or the ferromagnetic state is favorable.

Another possible trigger of magnetic and/or electric phenomena is a situation in which the Fermi surface is nested, i.e. there is a vector in reciprocal space that translates (parts of) the Fermi surface onto itself. This situation arises in graphene that is doped up to the *van Hove singularity*. At these energies there is a saddle point in the band dispersion and the density of states (DOS) diverges. The Fermi-surface nesting together with a diverging DOS can make the susceptibility divergent. This is then an indication of a phase transition into either a charge-density-wave, a spin-density-wave, or a ferromagnetic phase.

Spin-orbit coupling is closely related to magnetism. Angular momentum and spin degrees of freedom are linked through a term proportional to $\mathbf{L} \cdot \mathbf{S}$. The spin-orbit interaction mixes the p_z orbitals with d orbitals. However, it is possible to write an effective Hamiltonian that comprises only the usual p_z orbitals [77]. This effective Hamiltonian features an *intrinsic spin-orbit* (ISO) term, which is a next-nearest-neighbor hopping term. If the $z \to -z$ symmetry of the graphene plane (which lies in the (x, y)-plane) is broken, e.g. by a perpendicular electric field, a *Rashba* term must be considered. This term is a nearest-neighbor spin-flip hopping term [78, 79].

In 2005, Kane and Mele realized that the ISO interaction gives rise to a quantum spin Hall state [78, 79]. This state is then topologically protected, meaning that small perturbations or defects in the system can not destroy this state. It has an insulating bulk, but along the (zig-zag) edges spin-polarized currents do exist. These currents do not backscatter as long as no magnetic impurities are present. Unfortunately, the ISO interaction turns out to be too small in graphene to realize this new state. However, through these two papers, scientists got aware of the importance of topologically protected states and a new booming field of physics opened up. In 2006 the existence of a quantum spin Hall state was predicted to exist in HgTe quantum wells [80]. They were experimentally found a year later [81].

1.7 Outline

The outline of this thesis is the following: Firstly, a more quantitative introduction into the topic of single-layer and multilayer graphene is presented in **Chapter 2**. This chapter is suited for people who are not fully familiar with the tight-binding

description of graphene and the conventions used in the literature.

In **Chapter 3** it is shown that graphene, doped to the saddle point in the dispersion (van Hove singularity), exhibits a phase transition into a spin-density-wave phase. This work is based on Ref. [82]. We have used an approach in which we treat charge and spin degrees of freedom on the same footing, allowing, in principle, for a combination of charge and spin related phenomena. Such a spin-charge-density wave was theoretically predicted to exists in cold atom systems [83]. In graphene, however, spin and charge degrees of freedom decouple and only magnetic instabilities are found.

Next, spin-orbit interactions in a graphene bilayer are studied in **Chapter 4**. Both the intrinsic and Rashba spin-orbit couplings are inserted in the layers of a Bernal stacked graphene bilayer. The ISO interaction causes similar effects as in a monolayer (opening of a topologically nontrivial gap), whereas the Rashba interaction causes a surprising change in the energy dispersion; one of the (spin-degenerate) parabolic energy bands becomes linear. This cone is robust when next-nearest-neighbor hopping parameters are added. However, it is destroyed by a bias voltage between the layers, since this will open a gap. The results of this chapter are published in Ref. [84].

Because the band structure of ABA-stacked trilayers is much richer than the one of monolayers and bilayers, due to the presence of both a linear and a parabolic band, it is worth investigating the appearance of ferromagnetism due to the exchange mechanism. This analysis is performed in **Chapter 5**. As a result of the crossing of two linear and two parabolic bands at $E = 0$, the bands can fill up differently. This different filling of the linear and parabolic bands is dubbed *band-ferromagnetism*. It is found that the system can become ferromagnetic at low doping levels, but that the ferromagnetism comes from the parabolic bands only. The ferromagnetic phase transition, seen in monolayer graphene for large interactions, is absent. This work is published in Ref. [85].

In **Chapter 6**, the same ferromagnetic phase transition is investigated in ABC-stacked trilayer graphene. Parts of these results are presented in the master thesis of R. Olsen, a student whom I co-supervised. It is worth studying this phase transition in rhombohedral stacked trilayer graphene, because, due to the cubic bands, the kinetic energy cost of the magnetic state is much smaller than it is in systems with linear dispersion (monolayer), parabolic dispersion (bilayer), or both (ABA-stacked trilayer). Indeed, the (electron)-doping levels at which the system is ferromagnetic for a realistic interaction strength are around 50 times higher than they are in bilayer graphene. Because the density of states diverges at the Dirac point in ABC-stacked trilayer, screening must be taken into account. Since it is numerically very difficult to do, we use a simplified model for the screening. The results of this chapter are published in Ref. [86].

Although we expect our results with the simplified screening in Chapter 6 to

be accurate within 20 percent, the study of screening is an interesting topic on its own. This fact motivated us to determine the polarization in ABC-stacked multilayer graphene. Exact solutions have been found for both monolayer and bilayer graphene [87], but for systems with a higher number of layers a numeric solution is still lacking. A low-energy model yields a good approximation for the low-momentum behavior of the polarization, but fails in the short-wavelength limit. In **Chapter 7** we provide an analysis which allows one to determine where the approximation breaks down and indicate how one can obtain numeric results for the full momentum behavior of the polarization for an N-layer system. After deriving the small-k and large-k limit for the polarization in ABC-stacked trilayer graphene, we draw a realistic sketch of the polarization and screened potential. The results of this Chapter were recently submitted for publication [88].

Chapter 2

Preliminaries

Abstract

In this Chapter the tight-binding descriptions of monolayer and multilayer graphene are explained in detail for non-specialists in the field. The energy dispersion is derived and an expansion around the Dirac point is made to arrive at a low-energy continuum model.

2.1 Monolayer graphene

Graphene consists of carbon atoms ordered in a honeycomb lattice. The lattice sites are separated by a distance $a = 0.142$ nm. There is one valence electron (p_z orbital) that forms a much weaker pi bond. This electron can carry current by hopping from one carbon atom to the next. This process can be described by a *tight-binding model*. In such a set-up, the electrons are localized at the lattice sites but they can hop to any other lattice position. There is an energy associated with such a hopping, which depends on the overlap of the orbital wave functions. Since the overlap of two orbitals rapidly decreases when the two lattice sites are farther apart, it is often a very good approximation to include only hoppings between sites that are next to each other, i.e. *nearest-neighbor hopping*. The direct hopping of electrons between sites that are connected indirectly by two nearest-neighbor hoppings is called *next-nearest-neighbor hopping*. The unit cell of monolayer graphene contains two inequivalent sites, labeled A and B (see Fig. 2.1a). Therefore, nearest-neighbor hopping is between A and B sites, while next-nearest-neighbor hopping is always within either the A or the B sublattice. Throughout this thesis, direct next-nearest-neighbor hopping in monolayer graphene will be neglected. Therefore, it is not discussed in this Chapter either.

First, let us define the creation and annihilation operators, $a^\dagger(\mathbf{R}_i), b^\dagger(\mathbf{R}_i)$, and $a(\mathbf{R}_i), b(\mathbf{R}_i)$. These operators create or annihilate an electron on sublattice A or B on the lattice position $\mathbf{R}_i$. The Hamiltonian that describes the hopping

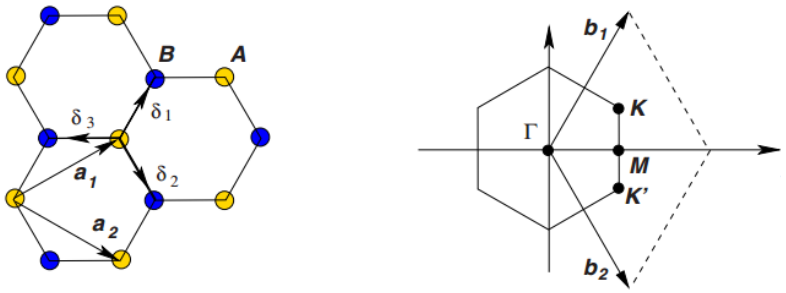

(a) (b)

Figure 2.1: (a) The honeycomb lattice with the different sublattices A and B, the lattice vectors a_1 and a_2 and the nearest-neighbor vectors δ_1, δ_2, and δ_3. (b) Brillouin zone of graphene with the reciprocal lattice vectors, b_1 and b_2, and the high symmetry points K, K', M, and Γ. Figure extracted and edited from Ref. [10].

electrons in a non-interacting system is given by

$$H_0 = -t \sum_{<i,j>} \left[a^\dagger(\mathbf{R}_i) b(\mathbf{R}_j) + H.c. \right], \tag{2.1}$$

where $H.c.$ stands for hermitian conjugate and $t \approx 3$ eV is the hopping energy, i.e. the reduction in kinetic energy due to the overlap of the wave functions between nearest-neighbor sites (delocalization). The sum is over nearest-neighbors only, indicated by the $< ... >$ brackets. To determine the energy-momentum relation, a Fourier transformation has to be performed. Hence, we insert the relation

$$a(\mathbf{R}_i) = \frac{1}{\sqrt{N_c}} \sum_{\mathbf{k}} a(\mathbf{k}) e^{-\mathbf{k}\cdot\mathbf{R}_i}$$

into equation (2.1), where N_c is the number of unit cells and the sum is over all (quasi)-momenta in the Brillouin zone. The Hamiltonian in reciprocal space has the following form,

$$H_0 = -t \sum_{\mathbf{k},i} \left[e^{-i\mathbf{k}\cdot\boldsymbol{\delta}_i} a^\dagger(\mathbf{k}) b(\mathbf{k}) + H.c. \right],$$

where the vectors $\boldsymbol{\delta}_i$ are the three vectors that point from A to B sites. They are shown in Fig. 2.1a. It is common to write down this Hamiltonian in matrix form and to take momentum as a continuous variable, $H_0 = \int d^2\mathbf{k} \psi^\dagger(\mathbf{k}) \mathcal{H}_0(\mathbf{k}) \psi(\mathbf{k})$,

with $\psi^\dagger(\mathbf{k}) = (a^\dagger(\mathbf{k}), b^\dagger(\mathbf{k}))$. The Hamiltonian density is then given by

$$\mathcal{H}_0(\mathbf{k}) = -t \begin{pmatrix} 0 & \gamma_{\mathbf{k}} \\ \gamma_{\mathbf{k}}^* & 0 \end{pmatrix},$$
$$\gamma_{\mathbf{k}} = \sum_{i=1}^{3} e^{-i\mathbf{k}\cdot\boldsymbol{\delta}_i}.$$

The energy-momentum relation of the charge-carriers in graphene is given by the eigenvalues of this Hamiltonian density, hence

$$E(\mathbf{k}) = \pm t|\gamma_{\mathbf{k}}| = \pm t\left[3 + 2\cos(\sqrt{3}ak_y) + 4\cos(\sqrt{3}ak_y/2)\cos(3ak_x/2)\right].$$

The two energy bands are shown in Fig. 2.4. The lower (upper) band is the valence (conduction) band and is completely filled (empty) for the charge-neutral system. The valence and conduction bands touch in the Brillouin zone at the K and K' points, which are called *valleys* (see Fig. 2.1b). These two points are inequivalent because they can not be connected by a reciprocal lattice vector. For many purposes, it is not necessary to use the full-band dispersion. The Hamiltonian can then be expanded around the K and K' point. After a rotation, the expanded Hamiltonian can be brought into the simple form

$$H_0^\xi = \int d^2\mathbf{k}\psi^\dagger(\mathbf{k})\mathcal{H}_0^\xi\psi(\mathbf{k}),$$
$$\mathcal{H}_0^\xi(\mathbf{k}) = v_F \begin{pmatrix} 0 & \xi k_x - ik_y \\ \xi k_x + ik_y & 0 \end{pmatrix},$$

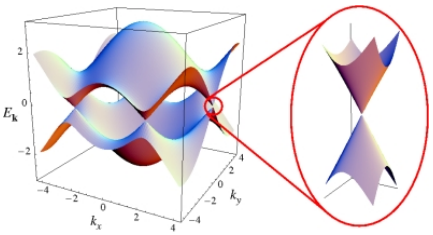

Figure 2.2: The full energy dispersion of monolayer graphene and a zoom-in on the K point for which the dispersion is linear. Figure extracted from Ref. [89].

where $\xi = 1$ ($\xi = -1$) for expansion around the K point (K' point) and $v_F = (3/2)at/\hbar \approx 10^6$ m/s is the Fermi velocity. It is easy to see that the dispersion becomes $E = \pm v_F|\mathbf{k}|$, hence linear. The linear dispersion is characteristic for massless (quasi-)particles. The velocity with which the charge carriers move is 300 times smaller than the velocity of light. Although one has to expand the energy around both the K and the K' point, it is often the case that the two valleys do not couple. In those situations it is sufficient to expand around the K point only, but an extra valley-degeneracy should then be introduced. In this low-energy continuum model the charge carriers are described by the Dirac equation. Therefore graphene has

similarities with quantum electro dynamics (QED) for massless fermions, but due to the lower Fermi velocity, phenomena like the Klein paradox and Zitterbewegung [32] should be easier to detect. It was P.R. Wallace who described the graphene energy dispersion for the first time in 1947 [90].

2.2 Bilayer graphene

The tight-binding description of multilayer graphene is very similar to the one for monolayer graphene. However, there are $2N$ atoms in the unit cell, where N is the number of layers. In addition, it is possible to hop between the layers. The hopping energy between sites that are direct neighbors in two opposite layers equals $t_\perp = 0.3$ eV. In a complete description, it is necessary to add next-nearest-neighbor hopping parameters. The values of the t_3 and t_4 parameters in the Slonczewski-Weiss-McClure (SWMc) model [63, 91] are comparable in magnitude to $t_\perp$. In the SWMc model, t_3 is the amplitude for $A1 - B2$ interlayer hopping, while t_4 describes either $A1 - A2$ or $B1 - B2$ hopping (see Fig. 2.3). The other parameters in the SWMc model are much smaller and we neglect them in this Chapter, but they are explained and included in Chapter 4. In this section we focus on a graphene bilayer. The bilayer Hamiltonian in real space has the form

$$\begin{aligned} H_0 = \sum_i \sum_{j=1}^{3} \Big\{ & -t \left[a_1^\dagger(\mathbf{R}_i - \boldsymbol{\delta}_j) b_1(\mathbf{R}_i) + a_2^\dagger(\mathbf{R}_i) b_2(\mathbf{R}_i + \boldsymbol{\delta}_j) + H.c. \right] \\ & - t_\perp \left[b_1^\dagger(\mathbf{R}_i) a_2(\mathbf{R}_i) + H.c. \right] - t_3 \left[a_1^\dagger(\mathbf{R}_i - \boldsymbol{\delta}_1) b_2(\mathbf{R}_i - \boldsymbol{\delta}_1 - \boldsymbol{\delta}_j) + H.c. \right] \\ & - t_4 \left[a_1^\dagger(\mathbf{R}_i + \boldsymbol{\delta}_j) a_2(\mathbf{R}_i) + b_1^\dagger(\mathbf{R}_i) b_2(\mathbf{R}_i + \boldsymbol{\delta}_j) + H.c. \right] \Big\}. \end{aligned}$$

Note that the t_3 term is such that the sum runs over all a_1 sites and that the electrons hop to the three b_2 sites that are located at $-\boldsymbol{\delta}_j$. Hence the orientation of this hopping is reversed with respect to the usual inplane nearest-neighbor hopping. This will be important in the following. The momentum space representation of this Hamiltonian can be derived after a Fourier transformation, but one can also argue that it must have the following form,

$$\begin{aligned} H_0 &= -t \int d^2\mathbf{k} \psi^\dagger(\mathbf{k}) \begin{pmatrix} 0 & \gamma_{\mathbf{k}} & \gamma_{\mathbf{k}}\gamma_4 & \gamma_{\mathbf{k}}^*\gamma_3 \\ \gamma_{\mathbf{k}}^* & 0 & \gamma_1 & \gamma_{\mathbf{k}}\gamma_4 \\ \gamma_{\mathbf{k}}^*\gamma_4 & \gamma_1 & 0 & \gamma_{\mathbf{k}} \\ \gamma_{\mathbf{k}}\gamma_3 & \gamma_{\mathbf{k}}^*\gamma_4 & \gamma_{\mathbf{k}}^* & 0 \end{pmatrix} \psi(\mathbf{k}), \\ \psi^\dagger(\mathbf{k}) &= \left(a_{1,\mathbf{k}}^\dagger, b_{1,\mathbf{k}}^\dagger, a_{2,\mathbf{k}}^\dagger, b_{2,\mathbf{k}}^\dagger \right) \end{aligned} \tag{2.2}$$

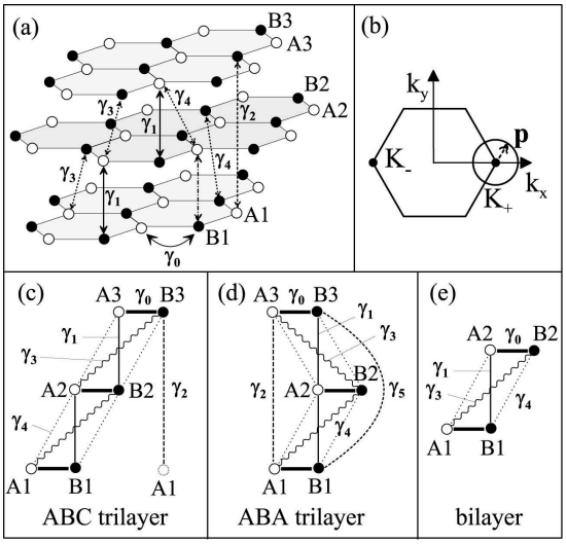

Figure 2.3: Overview of the Slonczewski-Weiss-McClure parameters in different multilayers of graphene. (a) Drawing of ABC-stacked trilayer graphene. (b) Brillouin zone of a graphene system. Schematic of the unit cell of (c) ABC-stacked trilayer, (d) ABA-stacked trilayer, and (e) bilayer graphene. In (c), γ_2 describes a vertical coupling between B_3 and A_1 sites in different unit cells. Figure extracted from Ref. [61].

where $\gamma_n = t_n/t$ and $\gamma_1 = t_\perp/t$. The Hamiltonian must have this form because the element in the matrix connecting two sites, e.g. A_1 and B_2 sites, has a coefficient γ_n, depending on which two sites are connected and a momentum factor $\gamma_{\mathbf{k}}$, $\gamma^*_{\mathbf{k}}$, or 1. Which momentum factor appears depends on the orientation of the projection of the sites in question on the plane. If they are oriented like B_1 sites around an A_1 site it gives a factor $\gamma_{\mathbf{k}}$, when the orientation is such as A_1 sites around a B_1 site, the momentum factor becomes $\gamma^*_{\mathbf{k}}$, and when the two sites are on top of each other there is no momentum transfer (hence a factor 1).

When neglecting the next-nearest-neighbor hopping parameters t_3 and t_4, the energy dispersion differs from monolayer in two ways. Firstly, there are high-energy bands, due to the dimerization of the orbitals on the sites with a direct neighbor in the other layer. Secondly, close around the K point the dispersion is quadratic instead of linear. Note that farther away from the Dirac point the dispersion becomes linear again. For phenomena at very low energies (compared to $t_\perp$) it is possible to derive an effective two-band model. It will have quadratic dispersion for all momenta and therefore the approximation breaks down at some point.

To derive the two-band model it is convenient to define $\psi_l^\dagger(\mathbf{k}) = (a_1^\dagger(\mathbf{k}), b_2^\dagger(\mathbf{k}))$, $\psi_h^\dagger(\mathbf{k}) = (b_1^\dagger(\mathbf{k}), a_2^\dagger(\mathbf{k}))$, and $\tilde{\psi}^\dagger(\mathbf{k}) = \left(\psi_l^\dagger(\mathbf{k}), \psi_h^\dagger(\mathbf{k})\right)$. Moreover, when a low-energy approximation is sufficient, one can expand $\gamma_{\mathbf{k}}$ around the K point, result-

ing in $-t\gamma_{\mathbf{k}} \approx v_F(k_x - ik_y) \equiv v_F\pi$. The Hamiltonian becomes

$$\mathcal{H} = \begin{pmatrix} \mathcal{H}_{11} & \mathcal{H}_{12} \\ \mathcal{H}_{12}^* & \mathcal{H}_{22} \end{pmatrix}, \tag{2.3a}$$

$$\mathcal{H}_{11} = \begin{pmatrix} 0 & 0 \\ 0 & 0 \end{pmatrix}, \tag{2.3b}$$

$$\mathcal{H}_{12} = \begin{pmatrix} \pi & 0 \\ 0 & \pi^\dagger \end{pmatrix}, \tag{2.3c}$$

$$\mathcal{H}_{22} = \begin{pmatrix} 0 & t_\perp \\ t_\perp & 0 \end{pmatrix}, \tag{2.3d}$$

and the Schrödinger equation, $H\tilde{\psi} = E\tilde{\psi}$ splits into two equations,

$$\mathcal{H}_{11}\psi_l + \mathcal{H}_{12}\psi_h = E\psi_l,$$
$$\mathcal{H}_{12}^*\psi_l + \mathcal{H}_{22}\psi_h = E\psi_h.$$

It is possible to eliminate the high-energy components ψ_h and expand up to linear order in E. This results into the equation

$$\left(\mathcal{H}_{11} - \mathcal{H}_{12}\mathcal{H}_{22}^{-1}\mathcal{H}_{12}^*\right)\psi_l = ES\psi_l,$$
$$S = (1 + \mathcal{H}_{12}\mathcal{H}_{22}^{-2}\mathcal{H}_{12}^*).$$

After redefining the fields $\phi = S^{1/2}\psi_l$ such that they are still normalized, one finds an effective Schrödinger equation,

$$S^{-1/2}\left(\mathcal{H}_{11} - \mathcal{H}_{12}\mathcal{H}_{22}^{-1}\mathcal{H}_{12}^*\right)S^{-1/2}\phi = E\phi,$$

which leads to the effective Hamiltonian

$$\mathcal{H}_{\text{eff}} \equiv S^{-1/2}\left(\mathcal{H}_{11} - \mathcal{H}_{12}\mathcal{H}_{22}^{-1}\mathcal{H}_{12}^*\right)S^{-1/2} = -\frac{1}{2m}\begin{pmatrix} 0 & \pi^2 \\ (\pi^\dagger)^2 & 0 \end{pmatrix},$$

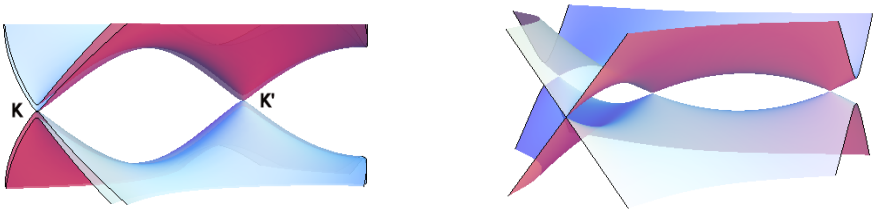

(a) (b)

Figure 2.4: (a) Bilayer dispersion with only nearest-neighbor hopping. The bands are quadratic around the Dirac points. (b) Zoom-in on the K point shows the trigonal warping effect when $\gamma_3 \neq 0$.

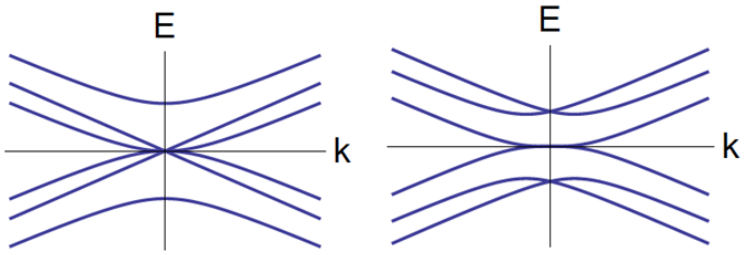

(a) (b)

Figure 2.5: (a) Cross-section of the dispersion around the Dirac point for ABA-stacked trilayer graphene. (b) Cross-section of the dispersion around the Dirac point for ABC-stacked trilayer graphene. All next-nearest-neighbor hopping constants are neglected.

where $m = t_\perp/(2\hbar^2 v_F^2)$ is the effective mass of the quasi-particles. One could include next-nearest-neighbor hopping parameters into the Hamiltonian (2.3) and follow the same procedure to find the corresponding terms in the effective Hamiltonian [92].

For the simplest tight binding model, in which only t and $t_\perp$ are nonzero, the dispersion around the K point is quadratic, as can be seen in Fig. 2.4. As the derivation of the low-energy effective Hamiltonian shows, the electrons are localized on the A_1 and B_2 sites in this limit. The dimerized electrons on the B_1 and A_2 are responsible for the energy bands that have split off from the charge-neutrality point by an energy $t_\perp$. The next-nearest-neighbor hopping parameters modify the low-energy dispersion. The effect of γ_3 is known as *trigonal warping*; the conduction and valence bands do not only touch at the Dirac point, but also at three satellite points (see Fig. 2.4). The effect of γ_4 is to break particle hole symmetry, shifting the satellite points away from $E = 0$.

2.3 Trilayer graphene

An additional layer can be placed on top of a bilayer in two different ways (see the introduction). The discussion in the previous section allows us to construct the Hamiltonian in reciprocal space directly. In Fig. 2.3 the different hopping parameters are shown. Trilayer graphene is the smallest system in which all the parameters of the SWMc model are included. With these parameters given, it is straightforward to write down the Hamiltonian density, although one should be careful to insert the right momentum factors. Since γ_2 and γ_5 connect sites on

next-nearest layers that are exactly on top of each other, they enter the theory without any momentum dependent terms attached to them. Define

$$\psi^\dagger(\mathbf{k}) = \left(a^\dagger_{1,\mathbf{k}}, b^\dagger_{1,\mathbf{k}}, a^\dagger_{2,\mathbf{k}}, b^\dagger_{2,\mathbf{k}}, a^\dagger_{3,\mathbf{k}}, b^\dagger_{3,\mathbf{k}}\right),$$

then the Hamiltonian is given by $H_0 = \int d^2\mathbf{k}\psi^\dagger(\mathbf{k})\mathcal{H}^{\mathrm{ABA/ABC}}\psi(\mathbf{k})$. The Hamiltonian density depends on the stacking order:

$$\mathcal{H}^{\mathrm{ABA}} = \begin{pmatrix} 0 & \gamma_{\mathbf{k}} & \gamma_{\mathbf{k}}\gamma_4 & \gamma^*_{\mathbf{k}}\gamma_3 & \gamma_2 & 0 \\ \gamma^*_{\mathbf{k}} & 0 & \gamma_1 & \gamma_{\mathbf{k}}\gamma_4 & 0 & \gamma_5 \\ \gamma^*_{\mathbf{k}}\gamma_4 & \gamma_1 & 0 & \gamma_{\mathbf{k}} & \gamma^*_{\mathbf{k}}\gamma_4 & \gamma_1 \\ \gamma_{\mathbf{k}}\gamma_3 & \gamma^*_{\mathbf{k}}\gamma_4 & \gamma^*_{\mathbf{k}} & 0 & \gamma_{\mathbf{k}}\gamma_3 & \gamma^*_{\mathbf{k}}\gamma_4 \\ \gamma_2 & 0 & \gamma_{\mathbf{k}}\gamma_4 & \gamma^*_{\mathbf{k}}\gamma_3 & 0 & \gamma_{\mathbf{k}} \\ 0 & \gamma_5 & \gamma_1 & \gamma_{\mathbf{k}}\gamma_4 & \gamma^*_{\mathbf{k}} & 0 \end{pmatrix}$$

$$\mathcal{H}^{\mathrm{ABC}} = \begin{pmatrix} 0 & \gamma_{\mathbf{k}} & \gamma_{\mathbf{k}}\gamma_4 & \gamma^*_{\mathbf{k}}\gamma_3 & 0 & \gamma_2 \\ \gamma^*_{\mathbf{k}} & 0 & \gamma_1 & \gamma_{\mathbf{k}}\gamma_4 & 0 & 0 \\ \gamma^*_{\mathbf{k}}\gamma_4 & \gamma_1 & 0 & \gamma_{\mathbf{k}} & \gamma_{\mathbf{k}}\gamma_4 & \gamma^*_{\mathbf{k}}\gamma_3 \\ \gamma_{\mathbf{k}}\gamma_3 & \gamma^*_{\mathbf{k}}\gamma_4 & \gamma^*_{\mathbf{k}} & 0 & \gamma_1 & \gamma_{\mathbf{k}}\gamma_4 \\ 0 & 0 & \gamma^*_{\mathbf{k}}\gamma_4 & \gamma_1 & 0 & \gamma_{\mathbf{k}} \\ \gamma_2 & 0 & \gamma_{\mathbf{k}}\gamma_3 & \gamma^*_{\mathbf{k}}\gamma_4 & \gamma^*_{\mathbf{k}} & 0 \end{pmatrix}$$

The ABA-Hamiltonian can be brought in a form with two blocks on the diagonal. One of these blocks is then the monolayer Hamiltonian, while the other one is the bilayer Hamiltonian with an interlayer hopping parameter $\tilde{t}_\perp = \sqrt{2}t_\perp$ [66]. The two blocks are coupled by γ_2 and γ_5 only. Hence, when the latter parameters are neglected, the energy dispersion around the Dirac point is a combination of a monolayer and a bilayer dispersion. When all next-nearest-neighbor processes are omitted, the bands are linear and parabolic (Fig. 2.5a). Inclusion of the entire set of SWMc parameters results in a distortion of the dispersion at low energy and low momenta, including trigonal warping (due to γ_3) effects and an overlap between the conduction and the valence bands [66].

Like for the bilayer system, the low-energy physics in the ABC-stacked trilayer takes place on the outer layers, because the electrons in the middle layer dimerize with either the top or the bottom layer. It is possible to construct an effective 2×2 Hamiltonian in the same way that was done for the bilayer. It is valid for small energies $E << t_\perp$ and is given by

$$\mathcal{H}_{\mathrm{eff}} = -\frac{(\hbar v_F)^3}{t_\perp^2}\begin{pmatrix} 0 & \pi^3 \\ (\pi^\dagger)^3 & 0 \end{pmatrix}.$$

From this effective Hamiltonian it is easy to deduce that the dispersion is cubic around the K point (Fig. 2.5b). Next-nearest-neighbor hopping parameters are again responsible for trigonal warping and particle-hole symmetry breaking.

2.4 Slonczewski-Weiss-McClure parameters

The SWMc-model is a very complete tight binding description of multilayer graphene. Nevertheless, there are some controversies about the values of the different parameters. The values of t' (the next-nearest-neighbor hopping parameter in monolayer graphene) given in the literature range from 0.07 to 0.68 eV [93, 94]. Also, it seems that the literature does not agree upon the sign of t'. Most authors take the t' term in the Hamiltonian to be negative, but there are some who let it be positive [95, 96, 97]. Although the term associated with this parameter breaks particle-hole symmetry, at low energies the only effect is to shift the whole dispersion by a constant and is therefore not important in such cases.

The value for γ_3 in graphite is experimentally determined to be $\gamma_3 \approx 0.3$ eV [91], but density functional theory for ABC-stacked trilayer graphene indicates that this parameter, although the absolute value is similar, has an opposite sign [98]. Experiment will tell who is right and trilayer graphene is the smallest system that can be used to determine all the SWMc parameters. Assuming (graphite) values for t, γ_1, and γ_3, experimentalists succeeded in determining the remaining parameters [99].

Chapter 3

SDW instability in highly doped graphene

Abstract

We study the instability of the metallic state towards the formation of a new ground state in graphene doped near the van Hove singularity. The system is described by the Hubbard model and a field theoretical approach is used to calculate the charge and spin susceptibility. We find that for repulsive interactions, within the random phase approximation, there is a competition between ferromagnetism and spin-density wave (SDW). It turns out that a SDW with a triangular geometry is more favorable when the Hubbard parameter is above the critical value $U_c(T)$, which depends on the temperature T, even if there are small variations in the doping. Our results can be verified by angle-resolved photoemission spectroscopy (ARPES) or neutron scattering experiments in highly doped graphene.[1]

3.1 Introduction

Graphene, a newly realized two-dimensional crystal of carbon atoms ordered on a honeycomb lattice [1], is being extensively studied due to its unusual electronic and structural properties. Undoped graphene is a zero-gap semiconductor with a linear low-energy dispersion relation and a vanishing density of states at the Fermi level [10]. Although the Coulomb interaction is unscreened in this regime, the system behaves mostly as a non-interacting electron liquid, where the minor effects of interactions are encoded in a renormalization of the Fermi velocity and the quasiparticle lifetime [100]. The opposite case is that of a divergent density of states, the so called Van Hove (VH) singularity, which is associated to a saddle

[1] This Chapter is based on *Spin-density-wave instability in graphene doped near the van Hove singularity*, D. Makogon, R. van Gelderen, R. Roldán, and C. Morais Smith, Phys. Rev. B **84**, 125404 (2011).

point in the band dispersion [101]. If the Fermi level lies near such a singularity, screening is perfect for wave vectors connecting VH singularities and correlation effects may be enhanced. Recently, several experimental groups have succeeded on making this regime accessible for graphene [56, 102, 103]. The techniques used for this aim are different: in Ref. [56] they have used twisted graphene, obtained from a rotation between stacked graphene layers, which allows one to tune the position of the VH singularity. Other methods involve chemical doping of graphene [102] or intercalation of gold clusters between the graphene layers [103]. This opens up the fascinating possibility to study correlated electronic phases in this material, such as superconductivity, charge-density waves (CDWs) or spin-density waves (SDWs).

The proximity of the Fermi level to a VH singularity in most of the cuprate superconductors has triggered large efforts to understand the role of a peaked density of states (DOS) on the electronic properties of an electron liquid [104]. Superconductivity, itinerant ferromagnetism (FM), CDWs, and SDWs are examples of competing instabilities associated with the VH scenario. In graphene, the existence of some of these instabilities has already been evidenced by recent experiments, such as a CDW [56, 103] or superconducting pairing due to electron-electron interactions [102], following the Kohn-Luttinger mechanism [105]. CDW and SDW phases usually occur in systems with Fermi surface nesting, i.e. when the Fermi surface can be mapped onto itself by a (nonzero) $\mathbf{k}$-vector (nesting vector). At low doping, graphene shows some nesting, since the Fermi surface is composed of two circles around the K and K' points. However, since the DOS is very low, these peaks are small and a very high (Hubbard) interaction is required to enter the DW regime [106]. The situation changes if we strongly dope graphene around the value $\mu \approx |t|$, where μ is the chemical potential and $t \approx 2.8$eV is the hopping parameter. The Fermi surface then acquires a hexagonal shape and nesting occurs in three directions (see Fig. 3.1). Furthermore, the VH singularities lie at the Fermi surface for this doping. At these points, the DOS diverges and we expect some non-trivial peaks in the susceptibility.

In this Chapter, we investigate the Hubbard model in a honeycomb lattice using a field theoretical approach. By performing a Hubbard-Stratonovich transformation, we determine the effective action in terms of an eight-component order parameter, which accounts for charge- and spin-degrees of freedom in the A and B graphene sublattices. We find that the charge susceptibility never diverges for repulsive interactions, thus excluding the possibility of a CDW formation, whereas the spin susceptibility exhibits several peaks. The peaks at the nesting wave vectors $\mathbf{k}$ are stronger than the one at $\mathbf{k} = 0$ (see Fig. 3.2a), thus signaling that SDW is the leading instability, that wins against FM for repulsive interactions.

In the following, we introduce the model and outline the main steps of the calculations in Sec. 3.2 Then, we present the temperature vs interaction vs doping

phase diagram and show that the metallic state becomes unstable towards a SDW phase for realistic values of the interaction parameter U in Sec. 3.3. Finally, we discuss possible experimental techniques which could be used to observe our results and draw our conclusions in Sec. 3.4.

3.2 The model

Due to the strong screening of interactions by the electron gas at the VH filling, we consider only the local Coulomb repulsion (the usual Hubbard U term), which is a good approximation around this doping level [107, 108, 109]. This term leads to a deformation of the band dispersion toward the saddle point [108], an effect that has been observed experimentally by angle-resolved photoemission spectroscopy (ARPES) [102]. Notice that longer-range interaction terms, such as the nearest-neighbor repulsion, would lead to a richer phase diagram, with the possibility of a Pomeranchuk instability [110, 111]. This scenario is in sharp contrast with low-doped graphene, for which the DOS vanishes and the Coulomb interaction will be only slightly screened and therefore will be long ranged. Hence, we use a tight-binding model with a Hubbard interaction U,

$$H = -t \sum_{<i,j>,s} (a^\dagger_{i,s} b_{j,s} + H.c.) + U \sum_{j \in A,B} c^\dagger_{j,\uparrow} c^\dagger_{j,\downarrow} c_{j,\downarrow} c_{j,\uparrow}, \tag{3.1}$$

where the operator c_j can be either a_j or b_j, depending whether j is a label of the A or B sublattice, respectively. Defining $c^\dagger_j = (c^\dagger_{j,\uparrow}, c^\dagger_{j,\downarrow})$, the Hubbard term can be rewritten using the relation

$$c^\dagger_{j,\uparrow} c^\dagger_{j,\downarrow} c_{j,\downarrow} c_{j,\uparrow} = \frac{1}{8} n_j^2 - \frac{1}{2} \mathbf{S}_j \cdot \mathbf{S}_j,$$

where $n_j = c^\dagger_j c_j$ is the on-site number operator and $\mathbf{S}_j = (1/2)\, c^\dagger_j \boldsymbol{\sigma}\, c_j$, describes the spin on the lattice site j. Note that the inner product $\mathbf{S}_j \cdot \mathbf{A}$, where $\mathbf{A}$ is some vectorial field, is defined by $\mathbf{S}_j \cdot \mathbf{A} = (1/2)\, c^\dagger_j\, (\boldsymbol{\sigma} \cdot \mathbf{A})\, c_j$, and that $\boldsymbol{\sigma}$ is the vector of Pauli matrices. The grand canonical partition function describing the system reads

$$Z = \int \mathrm{d}[c^\dagger] \mathrm{d}[c] e^{-S[c^\dagger, c]/\hbar},$$

where the action is given by

$$S = \int_0^{\hbar\beta} \mathrm{d}\tau \left[\sum_j c^\dagger_j \left(\hbar \frac{\partial}{\partial \tau} - \mu \right) c_j + H \right].$$

In this expression, τ is the imaginary time variable, $\beta = 1/k_B T$, and H is defined in Eq. (3.1). We will investigate the possible appearance of CDW and SDW

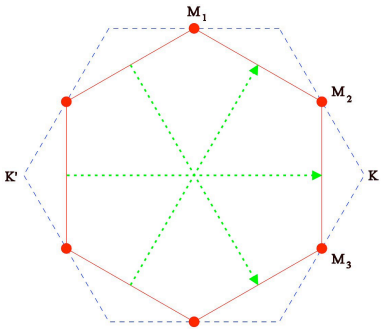

Figure 3.1: Blue dashed line is the Brillouin zone of monolayer graphene. Red line is the Fermi surface for $\mu = t$. Red dots are the van Hove singularities and the green dotted arrows are the nesting vectors.

instabilities by using a path integral formalism recently developed by some of the authors [83]. In the following, we briefly outline the procedure.

We start by performing a Hubbard-Stratonovich transformation that eliminates the quartic term in the action, but introduces eight auxiliary bosonic fields ρ^a, ρ^b, $\mathbf{M}^a$, and $\mathbf{M}^b$ related, respectively, to the electronic and the magnetic degrees of freedom of the fermionic fields of each sublattice. In Fourier space, the action then reads

$$S = -\hbar \sum_{\mathbf{k},n,\mathbf{k}',n'} \left(a^\dagger_{\mathbf{k},n} b^\dagger_{\mathbf{k},n} \right) \cdot \mathbf{G}^{-1}_{\mathbf{k},n;\mathbf{k}',n'} \cdot \begin{pmatrix} a_{\mathbf{k}',n'} \\ b_{\mathbf{k}',n'} \end{pmatrix} + S_2,$$

$$S_2 = \frac{1}{2U} \sum_{\mathbf{k},n,\alpha} \left[\mathbf{M}^\alpha_{\mathbf{k},n} \cdot \mathbf{M}^\alpha_{\mathbf{k},n} - (\rho^\alpha_{\mathbf{k},n})^2 \right],$$

where $\alpha = a, b$. The inverse Green's function is defined by

$$\mathbf{G}^{-1}_{\mathbf{k},n;\mathbf{k}',n'} = \mathbf{G}^{-1}_{0\,\mathbf{k},n;\mathbf{k}',n'} - \mathbf{\Sigma}_{\mathbf{k},n;\mathbf{k}',n'},$$

where the bare Green's function reads

$$-\hbar \mathbf{G}^{-1}_{0\,\mathbf{k},n;\mathbf{k}',n'} = \begin{bmatrix} -(\mu + i\hbar\omega_n)\mathbf{I} & -t\gamma_{\mathbf{k}}\mathbf{I} \\ -t\gamma^*_{\mathbf{k}}\mathbf{I} & -(\mu + i\hbar\omega_n)\mathbf{I} \end{bmatrix} \delta_{\mathbf{k},\mathbf{k}'}\delta_{n,n'},$$

with $\mathbf{I}$ a 2×2 identity matrix, $\omega_n = \pi(2n+1)/\hbar\beta$ the fermionic Matsubara frequency, and $\gamma_{\mathbf{k}} = e^{ia_0 k_y} + e^{-ia_0 k_y/2} \cos(\sqrt{3} a_0 k_x/2)$. In what follows we set the lattice constant $a_0 = 1$. The self-energy is given by

$$\hbar \mathbf{\Sigma}_{\mathbf{k},n;\mathbf{k}',n'} = \frac{-1}{2\sqrt{N\hbar\beta}} \begin{bmatrix} \boldsymbol{\sigma} \cdot \mathbf{M}^a - \rho^a \mathbf{I} & 0 \\ 0 & \boldsymbol{\sigma} \cdot \mathbf{M}^b - \rho^b \mathbf{I} \end{bmatrix},$$

where N is the number of sites of each sublattice and both, $\mathbf{M}^\alpha$ and ρ^α carry a subindex $(\mathbf{k} - \mathbf{k}', n - n')$. By introducing the eight component vector

$$\mathbf{M}_{\mathbf{k},n} = \left(\rho^a_{\mathbf{k},n}, \mathbf{M}^a_{\mathbf{k},n}, \rho^b_{\mathbf{k},n}, \mathbf{M}^b_{\mathbf{k},n} \right)^{\mathrm{T}}$$

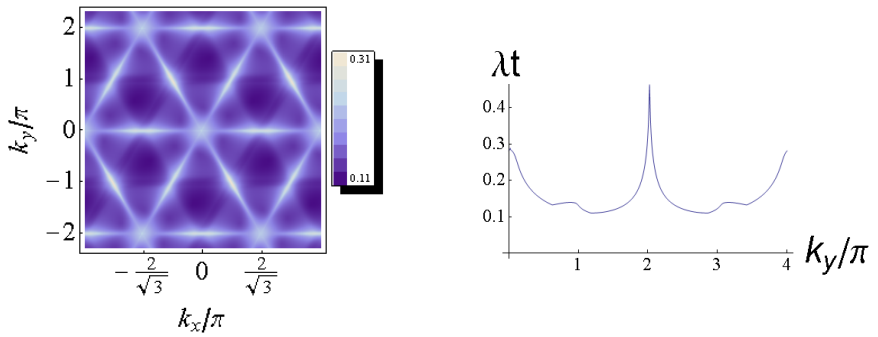

(a) (b)

Figure 3.2: (a) Density plot of the largest eigenvalue of $\boldsymbol{\eta\chi}$ for $T = 0.01t$. Brighter regions correspond to higher peaks in the spin susceptibility. The peaks at the three nesting wave vectors (see Fig. 3.1) are higher than the one at $\mathbf{k} = 0$, indicating that the SDW instability wins over the FM one. (b) Plot of the largest eigenvalue of $\boldsymbol{\eta\chi}$ for $T = 0.0025t$ for $k_x = 0$. Notice that the peak corresponding to SDW at $k_y = 2\pi$ is larger than the FM peaks at $k_y = 0$ and $k_y = 4\pi$.

and integrating out the fermionic fields, we obtain the effective action

$$S_{\text{eff}} = \frac{1}{2U} \sum_{\mathbf{k},n} \mathbf{M}_{\mathbf{k},n} \cdot \boldsymbol{\eta} \cdot \mathbf{M}_{-\mathbf{k},-n} - \hbar \text{Tr}[\ln(-\mathbf{G}^{-1})],$$

where $\boldsymbol{\eta} = \text{diag}(-1, 1, 1, 1, -1, 1, 1, 1)$ and the partition function becomes $Z = \int \text{d}[\mathbf{M}] \exp(-S_{\text{eff}}/\hbar)$. Finding the susceptibility from here is a two steps process. First, we introduce external source fields $\mathbf{J}$ and then we expand the fields in the action around their mean field value $\mathbf{M}_{\mathbf{k},n} = \langle \mathbf{M}_{\mathbf{k},n} \rangle_{\mathbf{J}} + \delta \mathbf{M}_{\mathbf{k},n}$. This results in a self-consistent equation for the mean field values of the fields. Using this equation, we may determine how the bosonic fields react on a distortion of the source fields.

The mean field values are those at which the action has an extremum. Thus, the linear terms in $\delta \mathbf{M}_{\mathbf{k},n}$ are imposed to vanish, yielding the self-consistent equation

$$\begin{aligned} \langle M^r_{\mathbf{k},n} \rangle_{\mathbf{J}} &= \frac{U}{2\sqrt{N\hbar\beta}} \sum_{\mathbf{p},m} \text{Tr}[\mathbf{P}^r \mathbf{G}_{\mathbf{J}\ \mathbf{p},m;\mathbf{p}-\mathbf{k},m-n}], \\ \mathbf{P} &= [\text{diag}(\mathbf{I}, 0), \text{diag}(\sigma^x, 0), \text{diag}(\sigma^y, 0), \text{diag}(\sigma^z, 0), \\ &\qquad \text{diag}(0, \mathbf{I}), \text{diag}(0, \sigma^x), \text{diag}(0, \sigma^y), \text{diag}(0, \sigma^z)]^{\text{T}}. \end{aligned}$$

The trace is taken over the matrices only, because the sum takes care of the trace in $\mathbf{k}$ and frequency space. After differentiating this equation with respect to the

source $\mathbf{J}$, one finds the susceptibility through the relation

$$\mathrm{d}\langle\mathbf{M}\rangle_{\mathbf{J}} = \hbar U \boldsymbol{\chi}_{\mathbf{J}}^{\mathrm{RPA}} \mathrm{d}\mathbf{J}, \tag{3.2}$$

where

$$\boldsymbol{\chi}_{\mathbf{J}}^{\mathrm{RPA}} = \left(\mathbf{I} - U\boldsymbol{\chi}_{\mathbf{J}}\boldsymbol{\eta}\right)^{-1} \boldsymbol{\chi}_{\mathbf{J}}.$$

Moreover, we can also determine the free energy by performing a Legendre transformation $\beta F[\langle\mathbf{M}\rangle_J] = U^{-1}\langle\mathbf{M}\rangle_J^{\dagger} \cdot \mathbf{J} - \ln(Z[\mathbf{J}])$ on the partition function which, up to quadratic order in the deviation $\Delta\langle\mathbf{M}\rangle_J \equiv \langle\mathbf{M}\rangle_J - \langle\mathbf{M}\rangle_0$ and without an additive constant, is

$$\beta F[\langle\mathbf{M}\rangle_J] = \frac{1}{2\hbar U^2} \left(\Delta\langle\mathbf{M}\rangle_J\right)^{\dagger} \cdot \left(\chi_0^{\mathrm{RPA}}\right)^{-1} \cdot \Delta\langle\mathbf{M}\rangle_J. \tag{3.3}$$

The susceptibility χ_0^{RPA} is evaluated in the absence of the source field, $\mathbf{J} = 0$. From here on, we assume that the system is in a homogeneous state, for which the mean field values of the boson fields are given by $\langle M_{\mathbf{k},n}^r\rangle_0 = \langle M_{0,0}^r\rangle\delta_{\mathbf{k},0}\delta_{n,0}$. As a consequence, the self-energy, the Green's function and the susceptibility matrix $\boldsymbol{\chi}_0$ are all diagonal in momentum and frequency space. Due to a nonzero self-energy, the Hamiltonian gets renormalized, such that

$$\hbar\mathbf{G}^{-1} = (\mu + i\hbar\omega_n)\mathbf{I} - H_0 - \boldsymbol{\Sigma} \equiv (\mu + i\hbar\omega_n)\mathbf{I} - H_{\mathrm{ren}},$$

where H_0 is given by the first term in Eq. (1). Assuming a (renormalized) Hamiltonian, which may be diagonalized by using the unitary operators $\mathcal{U}_{\mathbf{k}}$, such that $\mathcal{U}_{\mathbf{k}}^{\dagger} H_{\mathbf{k}} \mathcal{U}_{\mathbf{k}} = \sum_\alpha I^{(\alpha)} \epsilon_{\mathbf{k}}^{(\alpha)}$, where $I^{(\alpha)} = \mathrm{diag}(\delta_{\alpha,1}, \delta_{\alpha,2}, \delta_{\alpha,3}, \delta_{\alpha,4})$ and $\tilde{\epsilon}_{\mathbf{k}}^{(\alpha)} = \epsilon_{\mathbf{k}}^{(\alpha)} - \mu$, the susceptibility can be written as [83]

$$\chi_{\mathbf{k}}^{r,r'}(i\hbar\Omega_n) = \frac{1}{N} \sum_{\mathbf{p},\alpha,\beta} \frac{n_F\left(\tilde{\epsilon}_{\mathbf{p}+\mathbf{k}}^{(\alpha)}\right) - n_F\left(\tilde{\epsilon}_{\mathbf{p}}^{(\beta)}\right)}{\tilde{\epsilon}_{\mathbf{p}+\mathbf{k}}^{(\alpha)} - \tilde{\epsilon}_{\mathbf{p}}^{(\beta)} - i\hbar\Omega_n} T_{\mathbf{p}+\mathbf{k},\mathbf{p}}^{r,r';\alpha,\beta},$$

$$T_{\mathbf{p}+\mathbf{k},\mathbf{p}}^{r,r';\alpha,\beta} = -\frac{1}{4}\mathrm{Tr}[P^r \mathcal{U}_{\mathbf{p}+\mathbf{k}} I^{(\alpha)} \mathcal{U}_{\mathbf{p}+\mathbf{k}}^{\dagger} P^{r'} \mathcal{U}_{\mathbf{p}} I^{(\beta)} \mathcal{U}_{\mathbf{p}}^{\dagger}],$$

where Ω_n are bosonic Matsubara frequencies and $n_F(x) = 1/(e^{\beta x} + 1)$ is the Fermi distribution function. Notice that the overlap between the electron and hole wavefunctions is taken into account through the term $T_{\mathbf{p}+\mathbf{k},\mathbf{p}}^{r,r';\alpha,\beta}$.

3.3 Numerical results

Next, we investigate the possible instabilities by considering the static susceptibility $\boldsymbol{\chi}_{\mathbf{k}}(0)$. To evaluate the latter, one needs to perform a sum over all momenta in the Brillouin zone. We proceed by dividing the Brillouin zone in an $N \times N$ mesh, which implies that the sum in the expression for the susceptibility has N^2 terms.

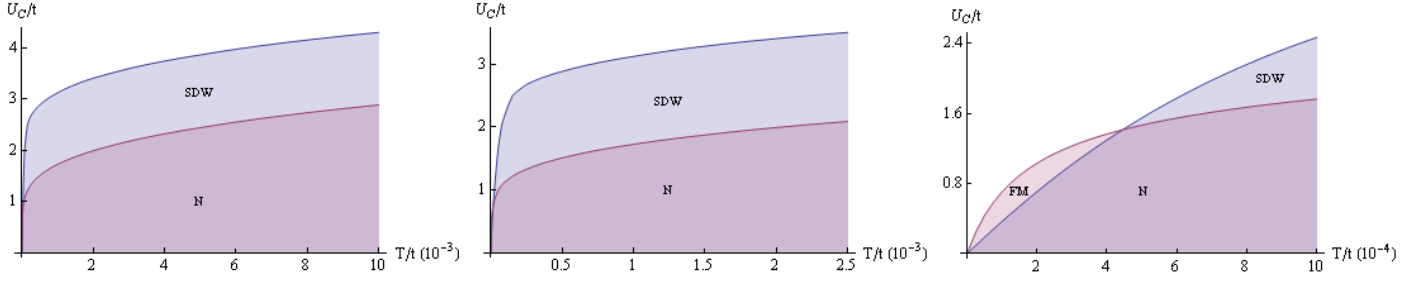

Figure 3.3: (a) The critical coupling required to enter the SDW regime (lower red line) and the FM regime (upper blue line) as a function of temperature, starting from the metallic phase at small U. We observe that the SDW phase wins for all temperatures. (b) Zoom-in of figure (a) for low temperatures. Both figures have been determined using a 10000×10000 mesh, for which convergence was eventually reached for $T > 0.5 \times 10^{-3}$. (c) Same as (a), but calculated in a 700×700 mesh. When not enough points are taken into account, the two lines cross, thus leading to an erroneous conclusion that a FM phase would be more favorable at low temperatures.

The instability condition for repulsive interactions requires the interaction strength U to exceed the critical value U_c defined by $0 = \det(\boldsymbol{\chi}_{J=0}^{-1} - U_c\boldsymbol{\eta}) = \det(\boldsymbol{\eta}\boldsymbol{\chi}_{J=0}^{-1} - U_c)$. This relation links the critical interaction strength to the largest eigenvalue $\lambda_{\mathbf{k}}$ of the matrix $\boldsymbol{\eta}\boldsymbol{\chi}_{\mathbf{k}}(0)$ by

$$U_c^{-1} = \max_{\mathbf{k}} \lambda_{\mathbf{k}} \equiv \lambda_{\mathbf{Q}}.$$

In Fig. 3.2a a density plot of the largest eigenvalue of the matrix $\boldsymbol{\eta}\boldsymbol{\chi}_{\mathbf{k}}(0)$ is shown for a temperature of $T = 0.01t \approx 350$ K. One can distinguish four inequivalent peaks (bright regions in Fig. 3.2a). The one at $\mathbf{k} = 0$ corresponds to a FM instability, while the other three, at nonzero $\mathbf{k}$, correspond to the three independent nesting vectors (see Fig. 3.1) and hence give rise to a SDW. Although not expected, for all temperatures the SDW peaks turn out to be higher than the peak corresponding to the FM phase (see Fig. 3.2b). However, this result depends heavily on the size of the mesh: for low temperatures, the sum converges slowly, and a wrong result can be inferred if N is not large enough. Indeed, by considering a 700×700 mesh, we find that a FM phase would set in at low temperatures [see Fig. 3.3c], whereas the results for a finer mesh (10000×10000) indicate that the true ground state is a SDW [see Fig. 3.3a and Fig. 3.3b].

$T/t(10^{-3})$	T (K)	U_c^{FM}	U_c^{SDW}
0.025	0.87	1.0570	0.8444
0.05	1.74	1.6710	0.9954
0.075	2.6	2.0410	1.0776
0.15	5.2	2.5018	1.2184
0.25	8.7	2.6828	1.3322
0.5	17	2.8896	1.5118
1	35	3.1272	1.7288
2.5	87	3.5082	2.0920
5	175	3.8652	2.4444
10	350	4.3030	2.8878

Table 3.1: Numerical values of the critical coupling U_c (in units of t) for a FM and a SDW phases calculated on a 10000×10000 mesh.

For zero temperature and a doping value exactly at the VH singularity, the critical coupling for both FM and SDW is zero. As explained below, our formalism is not suited to determine which state is more favorable. For finite temperatures, the SDW phase transition has a lower critical U than the FM one. Therefore, between the lower red and upper blue lines in Fig. 3.3 we find a SDW phase. Above the upper blue line, the system allows for a FM phase transition. The starting point of our formalism is a homogeneous ground state, after which we can determine the critical U that is needed to enter a more ordered phase, like the FM, SDW or CDW phase. To reach the regime above the upper blue line in Fig. 3.3, one has to start from a SDW ground state and subsequently determine if a phase transition to the FM phase will occur. Since the SDW ground state is inhomogeneous, our formalism is thus unable to determine the leading instability when U is in this regime.

If the system is tuned away from optimal doping, the VH singularities will no longer lie on the Fermi surface and nesting is reduced in general. This will

result in a lowering of the peaks in the maximal eigenvalue of the susceptibility and hence the critical couplings will increase. This behavior is shown in Fig. 3.4. The SDW peak is always higher than the FM one, but the height decreases quite rapidly as function of doping. The interaction strength in graphene cannot be tuned externally. Although at low doping the on-site Hubbard interaction is estimated to be around $U/t = 3.5$ [10, 112], values of U for highly doped graphene are, to the best of our knowledge, not yet known, but should not be different from the low-doping values. We therefore expect that a SDW phase should be observed experimentally, in the regime of T and U parameters shown in Fig. 3.4 (see also Table 3.1).

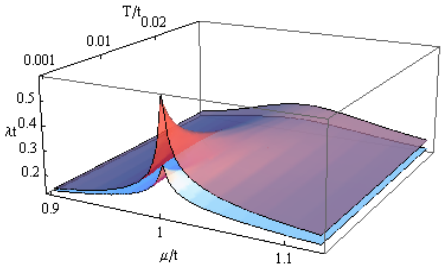

Figure 3.4: Largest eigenvalue vs temperature and vs chemical potential. The critical U scales as $1/\lambda_{\mathbf{Q}}$ and will therefore increase if the doping level is tuned away from $\mu = |t|$.

3.4 Discussion and conclusions

Recently, a CDW has been experimentally observed in twisted graphene bilayers doped at the VH singularity, but it has disappeared when the hopping parameter between the two layers has been put to zero [56]. A CDW phase seems also to be present for graphene grown on top of a superlattice of gold intercalated clusters [103], and a superconducting phase has been conjectured to occur for graphene heavily doped with Ca and K on both sides [102]. However, it is unclear which is the appropriate theoretical model to describe graphene under these circumstances, and for the conventional Hubbard model in a single layer, a CDW can only occur for attractive on-site interactions.

In conclusion, we have evaluated possible SDW and CDW instabilities from a metallic phase for the honeycomb lattice of a single layer of graphene doped at the VH filling. We found that charge and spin degrees of freedom are decoupled, and that CDWs occur for attractive, whereas SDWs occur for repulsive interactions. A peak in the spin susceptibility at zero wave vector has also been found, although precise calculations indicate that it is always subdominant with respect to the ones appearing at the nesting wave vectors, thus determining that the SDW instability must win over FM in the neighborhood of the metallic phase. This finding contradicts a previous result in the literature [106], and could only be

reached after a very careful and time consuming computation in a very large mesh. An interesting point is that the SDW phase is expected to occur at rather high temperatures. This is not very surprising, given that phenomena such as CDW or the integer quantum Hall effect, that usually occur at very low temperatures, have already been detected at high temperatures in graphene ($T = 77$K for the first and room temperature for the latter) [103, 36]. We hope that our results may stimulate further experiments to unveil the existence of a SDW phase in heavily doped graphene.

Acknowledgments

We acknowledge financial support from the Netherlands Organization for Scientific Research (NWO). R. Roldán thanks the EU-India FP-7 collaboration under MONAMI. We are indebted to Belén Valenzuela for a careful reading of this manuscript and for pointing out some ambiguities in the first draft of this Chapter.

Chapter 4

Spin-orbit interactions in bilayer graphene

Abstract

We investigate the effect that the intrinsic spin-orbit and the interlayer and intralayer Rashba interactions have on the energy spectrum of either an unbiased or a biased graphene bilayer. We find that under certain conditions, a Dirac cone is formed out of a parabolic band and that it is possible to create a "Mexican hat"-like energy dispersion in an unbiased bilayer. In addition, in the presence of only an intralayer Rashba interaction, the K (K') point splits into four distinct ones, contrarily to the case in single-layer graphene, where the splitting also takes place, but the low-energy dispersion at these points remains identical.[1]

4.1 Introduction

The influence of spin-orbit (SO) interactions on a single layer of graphene is well known. Kane and Mele [78, 79] were the first who showed that the intrinsic SO (ISO) interaction not only can open a gap, but also gives rise to a quantum spin Hall phase, due to localized edge states. On the other hand, the extrinsic Rashba SO interaction acts in the opposite direction, and tends to close the gap. Later, it was found that the Rashba interaction has interesting effects on its own, leading to a splitting of the Dirac point into four identical points [113]. This splitting is missed in the low-energy calculations used in Refs. [78, 79].

The presence of a gap controlled by the ISO interaction seemed promising, but it turned out to be smaller than originally expected by Kane and Mele [114, 115]. The value of its coupling constant is still controversial, but is expected to be in the range $0.0011 - 0.05$ meV [116, 117], thus very small. The Rashba coupling

[1] This Chapter is based on *Rashba and intrinsic spin-orbit interactions in biased bilayer graphene*, R. van Gelderen and C. Morais Smith, Phys. Rev. B **81**, 125435 (2010).

instead, can be tuned to much higher values. For typical values of an external electric field (50 V/300 nm), the Rashba coupling is less than 1 meV [118, 119]. The effect of impurities can increase this value to 7 meV [120]. However, recent experiments on epitaxial graphene grown on a Ni(111) substrate showed that the Rashba coupling can reach values up to 0.2 eV [121].

Shortly after the discovery of graphene, it was observed that bilayer graphene also exhibits remarkable phenomena. In bilayers, the low-energy excitations are no longer Dirac fermions like in graphene, but massive chiral fermions due to the parabolicity of the energy bands [57]. In addition, bilayer graphene turns out to be a semiconductor, with a gap that can be tuned via a chemical doping [122] or by an external gate voltage [123, 124, 125, 126, 60, 127].

Although there are several studies for the effect of SO interactions in graphene accounting for different boundaries [113, 128] (zigzag and armchair) and electron-electron interactions [115], no investigations of the SO effects have so far been performed in bilayer graphene, to the best of our knowledge. In this Chapter, we incorporate SO interactions in a bilayer graphene system in the presence and absence of a bias voltage. We distinguish between the ISO interaction, which respects the inversion symmetry of the graphene lattice and the extrinsic Rashba interaction, which is only present if this symmetry is broken. This could be done by introducing an electric field. Depending on the orientation of this electric field, there can be both intralayer as well as interlayer Rashba interactions. Furthermore, we consider how the energy spectrum deforms if the layer is biased with an electrical voltage.

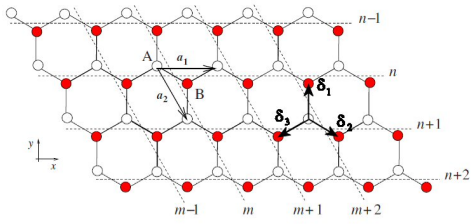

Figure 4.1: Relabeling of the graphene lattice. The length of the lattice vectors shown equals a, while the lattice spacing is $a/\sqrt{3}$. Figure extracted and modified from Ref. [10].

As a main result, we find that the intralayer Rashba coupling in an unbiased bilayer not only splits the K (K') points into four, in a different way than it does for monolayer graphene [113], but also creates a Dirac cone out of a parabolic band. In addition, we show that a fully spin-polarized Mexican-hat band arises in the energy spectrum of an unbiased layer, purely due to SO interactions.

The Mexican-hatlike dispersion appears in a variety of physical systems. This kind of spectrum, with a line of degenerate low-energy points forming a ring, was first discussed by Brazovskii [129], who showed that it leads to a "weak" crystallization transition. In cold atoms physics, a Mexican-hat-like dispersion appears and gives rise to topologically different ground states in SO Bose-Einstein

condensates [130]. The Mexican hat is known in high-energy physics as well, where, for example, the Higgs mechanism is expected to be responsible for the mass of the vector bosons. For bilayer graphene without SO interactions, the energy dispersion has the Mexican-hat shape if the layers are biased. In this case the dispersion was shown to potentialize electron-electron interactions, thus leading to a ferromagnetic instability [131].

The outline of this Chapter is the following: To render the comparison with a monolayer sample easier, we recall some results for monolayer graphene in Sec. 4.2. Next, we set up a model for bilayer graphene in Sec. 4.3, after which we include SO interactions within the layers in Sec. 4.4. In Sec. 4.5, we also include Rashba interactions between the layers, and in Sec. 4.6 we show that the results remain valid even if next-nearest-neighbor (n.n.n.) hopping is included. Finally, we draw our conclusions in Sec. 4.7.

4.2 SO interactions in monolayer graphene

In graphene, the carbon atoms form a honeycomb lattice. Because there are two inequivalent positions for the carbon atoms, this honeycomb lattice can be seen as a triangular lattice with two atoms per unit cell, called A and B, see Fig. 4.1. In the tight-binding approach, one assumes that the electrons are localized around the lattice sites and that they can hop from one lattice site to the next (nearest-

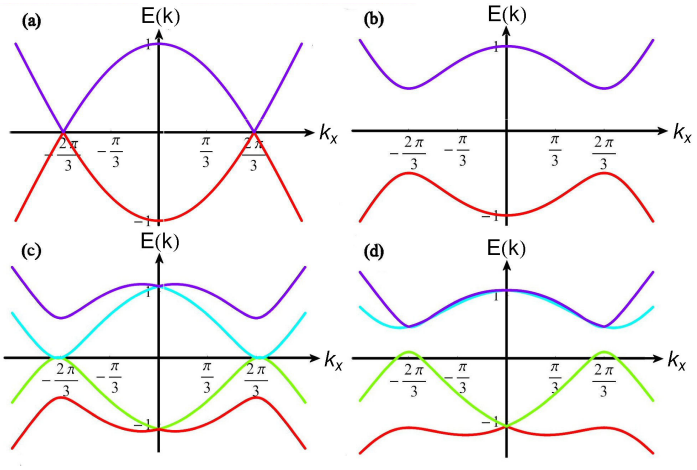

Figure 4.2: Behavior of a graphene sheet for different values of the SO parameters. (a) $\Delta_{SO} = 0$, $t_R = 0$. (b) $\Delta_{SO} = 0.5$, $t_R = 0$. (c) $\Delta_{SO} = 0$, $t_R = 0.2$. (d) $\Delta_{SO} = 0.5$, $t_R = 0.2$. Parameter values are $t = 1$, $a = 1$, $k_y = 2\pi/(\sqrt{3}a)$.

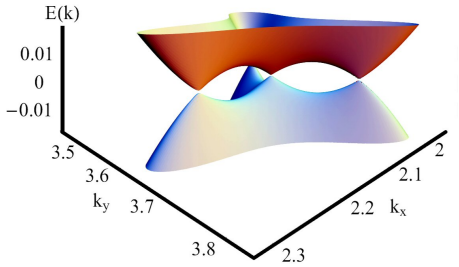

Figure 4.3: Splitting of the Dirac cones due to the Rashba interaction. For $\Delta_{SO} = 0$ no gap opens. In this figure: $t = 1$, $t_\perp = 0.2$, $a = 1$, $\Delta_{SO} = 0$, and $t_R = 0.2$.

neighbor hopping). The noninteracting Hamiltonian is then given by

$$H_0 = t \sum_{\substack{i\in\Lambda_A,\sigma \\ j=1,2,3}} \left[a_\sigma^\dagger(\mathbf{R}_i) b_\sigma(\mathbf{R}_i + \boldsymbol{\delta}_j) + h.c\right], \tag{4.1}$$

where σ is the spin index, i runs over the A-sublattice sites and j over the nearest-neighbor vectors, which, with a lattice orientation as in Fig. 4.1, are defined by

$$\begin{aligned}
\boldsymbol{\delta}_1 &= \frac{a}{\sqrt{3}}(0,1), \\
\boldsymbol{\delta}_2 &= \frac{a}{\sqrt{3}}\left(\frac{\sqrt{3}}{2}, -\frac{1}{2}\right), \\
\boldsymbol{\delta}_3 &= \frac{a}{\sqrt{3}}\left(-\frac{\sqrt{3}}{2}, -\frac{1}{2}\right).
\end{aligned}$$

The constant t is the hopping parameter (≈ 3 eV) and $a/\sqrt{3} \approx 0.142$ nm is the lattice spacing.

After relabeling the lattice as in Fig. 4.1, one can bring the Hamiltonian (4.1) into the form

$$\begin{aligned}
H_0 = t \sum_{n,m,\sigma} \Big[& a_\sigma^\dagger(m,n) b_\sigma(m,n) + a_\sigma^\dagger(m,n) b_\sigma(m-1,n) \\
& + a_\sigma^\dagger(m,n) b_\sigma(m,n-1) + H.c.\Big].
\end{aligned}$$

By performing a Fourier decomposition, the free Hamiltonian reads

$$H_0 = t \int d^2k\, \psi^\dagger(k) M^0_{4\times4} \psi(k), \tag{4.2}$$

where $\psi^\dagger(k) = (a^\dagger(k)_\uparrow, a^\dagger(k)_\downarrow, b^\dagger(k)_\uparrow, b^\dagger(k)_\downarrow)$,

$$M^0_{4\times 4} = \begin{pmatrix} 0 & 0 & \gamma_{\mathbf{k}} & 0 \\ 0 & 0 & 0 & \gamma_{\mathbf{k}} \\ \gamma^*_{\mathbf{k}} & 0 & 0 & 0 \\ 0 & \gamma^*_{\mathbf{k}} & 0 & 0 \end{pmatrix},$$

and $|\gamma_{\mathbf{k}}|^2 = 3 + 2\cos(ak_x) + 4\cos(ak_x/2)\cos(\sqrt{3}/2ak_y)$. The eigenvalues of H_0 are the well known energy bands of graphene [10], $E_\pm = \pm t|\gamma_{\mathbf{k}}|$. Both bands are degenerate with respect to the spin degrees of freedom.

If one wants to include SO interactions into the graphene system, one has to distinguish between the ISO interaction and the extrinsic Rashba term. The ISO interaction does respect all symmetries of the graphene lattice and has the form of a n.n.n. hopping term,

$$H_{SO} = it_{SO} \sum_{<<i,j>>} \nu_{ij} c_i^\dagger s_z c_j.$$

In this expression, t_{SO} is the ISO coupling constant, s_z is the z-component Pauli matrix describing the spin, and c_j is either a_j or b_j, depending wether the index j labels an A or B-sublattice site, respectively. The factor ν_{ij} is $+1$ if the n.n.n. hopping is anti-clockwise and -1 if it is clockwise (with respect to the positive z-axis). Note that this term describes hopping within the same sublattice.

Using the relabeling of the lattice shown in Fig. 4.1 and performing a Fourier decomposition, the ISO Hamiltonian can be rewritten as

$$H_{SO} = \Delta_{SO} \int d^2k\, \psi^\dagger(k) M^{SO}_{4\times 4} \psi(k), \tag{4.3}$$

where

$$M^{SO}_{4\times 4} = \begin{pmatrix} \eta_k & 0 & 0 & 0 \\ 0 & -\eta_k & 0 & 0 \\ 0 & 0 & -\eta_k & 0 \\ 0 & 0 & 0 & \eta_k \end{pmatrix},$$

$\eta_k = [1/(3\sqrt{3})]\left[2\sin(ak_x) - 4\sin(ak_x/2)\cos\left(\sqrt{3}ak_y/2\right)\right]$ and $\Delta_{SO} = 3\sqrt{3}\, t_{SO}$.

The extrinsic SO interaction is the Rashba term, which is only present if the inversion symmetry of the graphene lattice, $z \to -z$, is broken. This can happen if the graphene sheet couples to a substrate or if an electric field is present. For a perpendicular electric field, $\mathbf{E} = E\,\hat{\mathbf{z}}$, the Rashba coupling has the form of a nearest-neighbor hopping term and is given by [113, 132, 79]

$$H_R = it_R \sum_{<i,j>} c_i^\dagger \left(\mathbf{s} \times \hat{\mathbf{d}}_{ij}\right) \cdot \hat{\mathbf{z}}\, c_j + H.c., \tag{4.4}$$

where the Rashba coupling t_R can be tuned by changing the electric field strength, $\mathbf{s}$ is the vector of Pauli matrices and $\hat{\mathbf{d}}_{ij}$ is the unit vector that connects the i and j lattice sites. This term describes nearest-neighbor hopping, but it only couples nearest-neighbors with opposite spin. This is clearly seen if we rewrite this term in the same way that we rewrote the other terms,

$$H_R = t_R \int d^2k\, \psi^\dagger(k) M^R_{4\times4} \psi(k), \tag{4.5}$$

where we have defined

$$\begin{aligned}
M^R_{4\times4} &= \begin{pmatrix} 0 & N_{2\times2} \\ N^\dagger_{2\times2} & 0 \end{pmatrix}, \\
N_{2\times2} &= \begin{pmatrix} 0 & i\left[\xi_1(k) + \xi_2(k)\right] \\ i\left[\xi_1(k) - \xi_2(k)\right] & 0 \end{pmatrix}, \\
\xi_1(k) &= e^{i\frac{1}{2}ak_x}\left[e^{-i\frac{\sqrt{3}}{2}ak_y} - \cos\left(\frac{1}{2}ak_x\right)\right], \\
\xi_2(k) &= \sqrt{3}e^{i\frac{1}{2}ak_x}\sin\left(\frac{1}{2}ak_x\right).
\end{aligned}$$

The total Hamiltonian can be obtained by collecting Eqs. (4.1), (4.3), and (4.5),

$$H = \int d^2k\, \psi^\dagger(k) \left(t\, M^0_{4\times4} + \Delta_{SO}\, M^{SO}_{4\times4} + t_R\, M^R_{4\times4}\right) \psi(k).$$

In Fig. 4.2 we show the behavior of the energy dispersion for a graphene sheet for different values of the SO parameters, Δ_{SO} and t_R, in units of t. Without SO interactions, we find the well-known graphene spectrum with Dirac cones centered at the K and K' points in the reciprocal space [10], see Fig. 4.2a. The ISO interaction opens a gap, but respects the spin degeneracy of the energy bands (Fig. 4.2b). The Rashba term does not open a gap on its own, but it does lift the spin degeneracy, except at the $k_x = 0$ point, as it can be seen in Fig. 4.2c. By zooming in on the region around the K (K') point, we see that the Rashba term splits the Dirac cones into four, as noted in Ref. [113]. This behavior is depicted in Fig. 4.3. Note that this effect is missed in the approximation made by Kane and Mele [79], which is effectively a zeroth order approximation of the Rashba term. If one takes linear terms in k into account, this effect is already present. Here, however, we keep the full expression for the spectrum, without resorting to approximations. The combined effect of the ISO interaction and the Rashba term breaks the particle hole symmetry (Fig. 4.2d). If the Rashba term is small ($t_R < \Delta_{SO}$), the gap is finite [79], otherwise the gap closes (not shown).

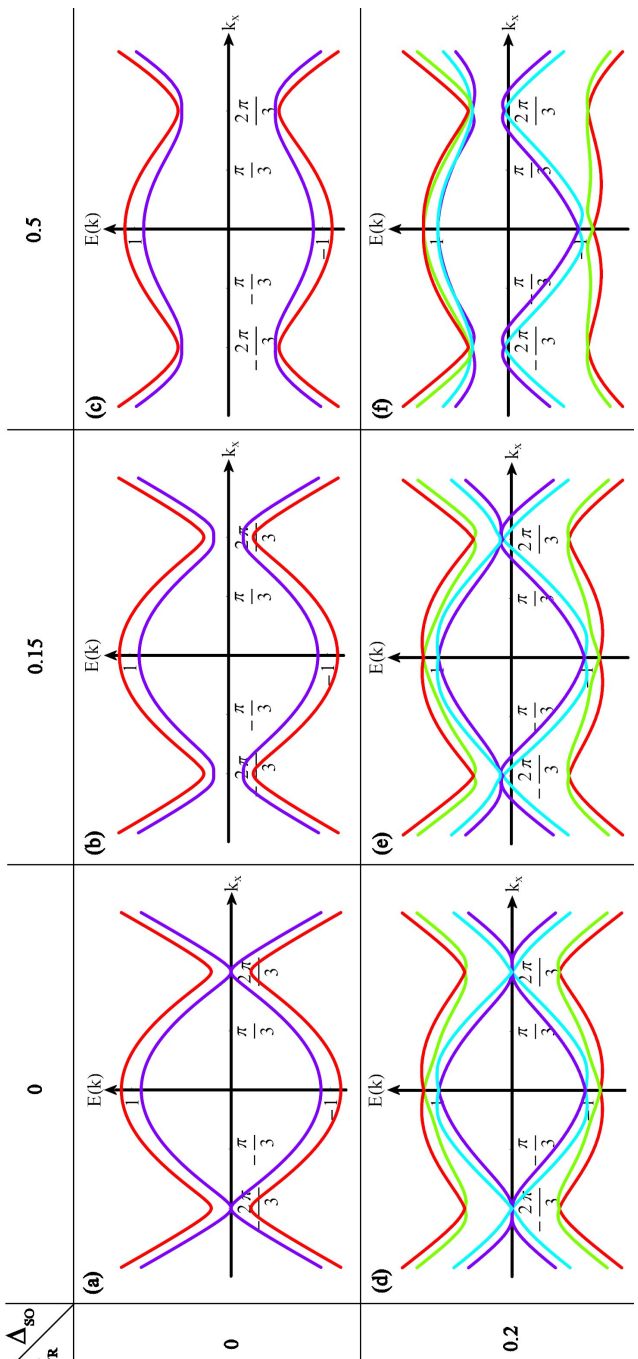

Figure 4.4: Energy spectrum of bilayer graphene for different values of the SO interactions. In this figure the layer is unbiased, hence $V = 0$. Other parameters have the values $t = 1$, $t_\perp = 0.2$, $a = 1$, and $k_y = 2\pi/(\sqrt{3}a)$.

4.3 Bilayer graphene model

Before including the SO interactions into bilayer graphene, let us first consider the noninteracting Hamiltonian. The form of the Hamiltonian of a multilayer graphene system depends on the stacking of the layers [10]. For bilayers, however, there are only two possibilities. The lattice sites can lay exactly on top of each other, or they can be arranged in a Bernal stacking[2], in which the A sites of the upper layer (A_1) lay on top of the B sites of the lower one (B_2), while the other sites (B_1 and A_2) lie opposite to a honeycomb center. We will assume the Bernal stacking here, because it is the most common one.

The consequence of a Bernal stacking is that, in a first approximation, the only interlayer hopping is between A_1 and B_2 sites. It is straightforward to generalize the noninteracting monolayer Hamiltonian to a bilayer one. First, we define

$$\Psi(k)^\dagger = \left(a^\dagger_{\uparrow,1}\,,\, a^\dagger_{\downarrow,1}\,,\, b^\dagger_{\uparrow,1}\,,\, b^\dagger_{\downarrow,1}\,,\, a^\dagger_{\uparrow,2}\,,\, a^\dagger_{\downarrow,2}\,,\, b^\dagger_{\uparrow,2}\,,\, b^\dagger_{\downarrow,2}\right),$$

where the layers 1 and 2 are represented by the corresponding index. We introduce an interlayer hopping parameter, $t_\perp \approx (0.1 - 0.2)\,t$, and bias the bilayer system with a gate voltage V. This gate voltage can be tuned externally and is such that the lower layer has an electric potential $-V$, while the upper layer has V. With this new parameters, the non-interacting Hamiltonian is given by

$$H_0^{bl} = \int d^2k\, \Psi^\dagger(k) M^0_{8\times 8} \Psi(k), \tag{4.6}$$

$$M^0_{8\times 8} = \begin{pmatrix} V\mathbb{1}_{4\times 4} + t\, M^0_{4\times 4} & A \\ A^\dagger & -V\mathbb{1}_{4\times 4} + t\, M^0_{4\times 4} \end{pmatrix},$$

$$A = \begin{pmatrix} 0 & 0 & t_\perp & 0 \\ 0 & 0 & 0 & t_\perp \\ 0 & 0 & 0 & 0 \\ 0 & 0 & 0 & 0 \end{pmatrix}.$$

If we consider $V = 0$ for the moment, we see in Fig. 4.4a that the spectrum is different from the one for monolayer graphene. The dispersion at the K (K') points, where the valence and the conduction bands touch, is no longer linear, but parabolic. This means that in a low-energy approximation the quasi particles become massive ($m \approx 0.054 m_e$) [58]. However, these particles are chiral with respect to sublattice pseudospin and are therefore massive chiral fermions [57], which are a new type of quasi particles, characteristic for bilayer graphene.

If there is a nonzero voltage difference, a gap will open in the energy spectrum. In fact, not only a gap opens, but the parabolic bands are deformed into Mexican

[2]Note that for bilayers there is no difference between Bernal stacking and rhombohedral stacking, since they differ in the orientation of a possible third layer.

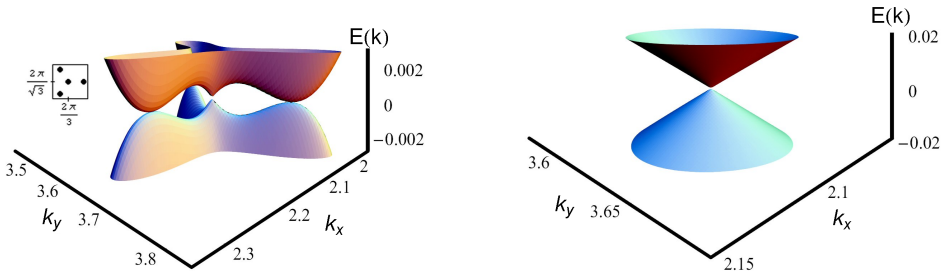

(a) (b)

Figure 4.5: Due to the Rashba coupling, the spin degeneracy of the low lying energy bands is lifted. (a) One band exhibits four touching points between the valence and the conduction bands. Inset: points in k-space where the valence and the conduction bands touch. (b) The other band becomes a Dirac cone. In these figures, the layer is unbiased there is no ISO interaction, and $t_R = 0.2$. Other parameters have the values $t = 1$, $t_\perp = 0.2$, and $a = 1$.

hats in the vicinity of the K (K') points (see Ref. [126] and the discussion in Sec. 4.4.2). However, the energy bands remain spin degenerate, because a nonzero voltage on its own cannot lift the spin degeneracy; as we will discuss in the next section, interactions are required to reach this aim.

4.4 Intralayer SO interactions in bilayer graphene

4.4.1 No bias voltage

Now that we have understood the single-particle spectrum for the bilayer graphene system, let us add SO interactions. We already saw that we have to distinguish between the ISO and the Rashba interactions, but for the bilayer system there is another subdivision, namely into intralayer and interlayer interactions. In this section, we will analyze the effects that the intralayer ISO and Rashba couplings have on the energy spectrum of the bilayer system. The effect of these interactions in the presence of a bias voltage are subsequently discussed. Later we include also interlayer interactions. This is done in Sec. 4.5

The ISO interaction respects the symmetries of a single graphene sheet. Since a graphene bilayer has a smaller symmetry group than a single layer, we expect this interaction to be present in the planes of the bilayer system as well. The ISO

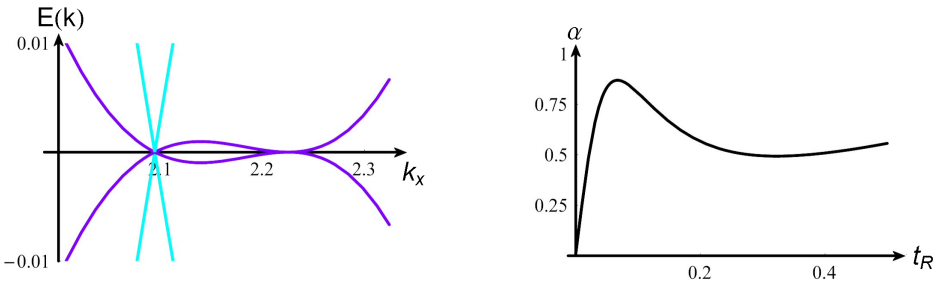

(a) (b)

Figure 4.6: (a) Zoom in on the K point of Fig. 4.4d and an intersection along the line $k_y = 2\pi/(\sqrt{3}a)$ of Fig. 4.5. (b) Slope (α) of the Dirac cone as a function of the Rashba coupling t_R. The scale of the α-axis depends on all parameters of the theory. Here: $t = 1$, $t_\perp = 0.2$, $a = 1$, $V = 0$, $\Delta_{SO} = 0$, and $k_y = 2\pi/(\sqrt{3}a)$.

interaction Hamiltonian is then given by

$$H_{SO} = \Delta_{SO} \int d^2k \, \Psi^\dagger(k) M^{SO}_{8\times 8} \Psi(k), \tag{4.7}$$

$$M^{SO}_{8\times 8} = \begin{pmatrix} M^{SO}_{4\times 4} & 0 \\ 0 & M^{SO}_{4\times 4} \end{pmatrix}. \tag{4.8}$$

Regarding the Rashba term, we expect that a perpendicular electric field gives rise to intralayer interactions in the same way that it did for a single sheet of graphene. Effectively, we have two copies of the monolayer Rashba interaction,

$$H_R = t_R \int d^2k \, \Psi^\dagger(k) M^{R}_{8\times 8} \Psi(k), \tag{4.9}$$

$$M^{R}_{8\times 8} = \begin{pmatrix} M^{R}_{4\times 4} & 0 \\ 0 & M^{R}_{4\times 4} \end{pmatrix}. \tag{4.10}$$

In Fig. 4.4, the energy spectrum of an unbiased bilayer graphene is shown for different values of Δ_{SO} and t_R. For zero SO interactions, we observe the well-known parabolic bands, which are spin degenerate (see Fig. 4.4a). These degeneracies cannot be lifted by the ISO interaction on its own, which simply opens a gap in the spectrum (Fig. 4.4b and Fig. 4.4c). This is the same behavior as for monolayer graphene. Things become interesting when we consider the case of zero ISO coupling and a nonzero Rashba interaction (Fig. 4.4d). The spin degeneracy of the bands is then lifted, but in a very particular way. In Fig. 4.5a, we see that for one of the spin bands (purple lines in Fig. 4.4d) the K point splits into four points again, as for monolayer graphene. One of them remains at the former K point position and the others form a triangle around it, see the inset

in Fig. 4.5a. We will refer to these four points as the split K point. However, here very special features appear: Besides the two energy bands (conduction and valence band) that touch at four points, there are two more bands , associated with the other spin orientation (blue lines in Fig. 4.4d), that touch and form a Dirac cone, as it can be seen in Fig. 4.5b. The center of this Dirac cone is exactly at the point in k space where, without Rashba interaction, the K point was located. This is also the location of the central of the four points that form the split K point. This central point is different from the other three. If we analyze Fig. 4.6a, which shows a zoom-in of Fig. 4.4d and a cross-section cut of Fig. 4.5a and Fig. 4.5b, we see that the central point, located at $k_x = 2\pi/(3a)$, $k_y = 2\pi/(\sqrt{3}a)$ has, in addition to the Dirac cone, a linear crossing at very low energy, whereas the off-center points have only a higher order crossing. A zoom in on the satellites (not shown) seems to indicate that the crossing in the k_y-direction is similar to that in the k_x-direction. This is different from the case of monolayer graphene, where the K point splits into four equivalent points. The most striking feature of the intralayer Rashba coupling is the formation of a Dirac cone out of a parabolic band. If we perform a low-energy approximation and use $\mathbf{k} = \mathbf{K} + \mathbf{q}$, this Dirac cone has the dispersion relation $E(\mathbf{q}) = \alpha|\mathbf{q}|$. The slope α, which corresponds to the velocity of the low-energy excitations, depends on the parameters of the theory and cannot be determined analytically. We have plotted the slope of this cone as a function of t_R for certain parameter values in Fig. 4.6b.

If we set both t_R and Δ_{SO} unequal to zero (Fig. 4.4e and Fig. 4.4f), we see that depending on their relative values, a gap can open. For small ISO interactions, the gap stays closed, but the bands are heavily deformed in an asymmetric manner. Moreover, the particle-hole symmetry is lost. The split K point becomes so deformed that we cannot identify the four points any longer. If Δ_{SO} becomes large enough a gap opens, but the asymmetry remains.

4.4.2 Effect of a bias voltage

If we add a bias voltage to a bilayer graphene system without SO interactions, the system becomes a semiconductor with a tunable gap. We will see in the following that SO interactions can heavily deform the energy dispersion.

As found earlier [60, 10], we observe that for $\Delta_{SO} = t_R = 0$ the effect of the bias is to open a gap and to introduce a Mexican-hatlike shape in the lowest energy band around the K and K' points. The spectrum remains particle-hole symmetric and the bands remain spin degenerate, as is shown in Fig. 4.7a. By keeping $t_R = 0$ and introducing a finite Δ_{SO}, the spin degeneracy is lifted, but only in the region around the K (K') points, as can be seen in Fig. 4.8a. When Δ_{SO} is not too large, the Mexican-hat feature remains, but it disappears as Δ_{SO} is increased further (see Fig. 4.7b and Fig. 4.7c). The gap at the K point (this is not the actual gap if

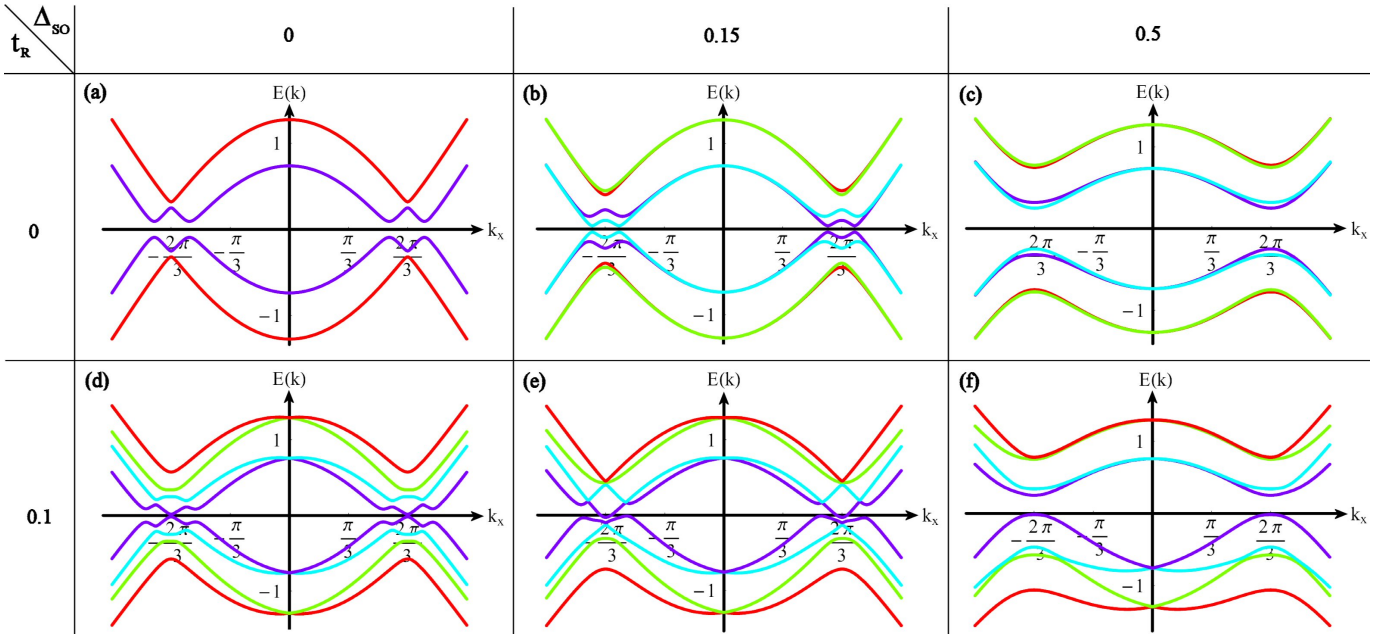

Figure 4.7: Energy spectrum of bilayer graphene for different values of the SO interactions. In this figure, the layer is biased, $V = 0.25$. Other parameters have the values $t = 1$, $t_\perp = 0.2$, $a = 1$, and $k_y = 2\pi/(\sqrt{3}a)$.

$V > \Delta_{SO}$, because of the Mexican-hat structure), equals $2|V - \Delta_{SO}|$; Therefore, during the transition from the Mexican hat to a parabolic band the gap closes at $V = \Delta_{SO}$, after which it opens again. Note that this behavior is similar to that described in Ref. [78], where both the ISO coupling Δ_{SO} and a staggered sublattice potential λ_v can open a gap in monolayer graphene. If Δ_{SO} exceeds λ_v, a transition occurs between a normal insulator phase and a quantum spin Hall phase. Nonetheless, we have to be careful with this comparison, since a staggered sublattice potential in monolayer graphene is fundamentally different from a bias potential in a bilayer. For example, in monolayer graphene we do not observe a Mexican-hat structure and the edge states are responsible for the phase transition. We do not take those into account here. In addition, although the ISO interaction alone cannot lift the spin degeneracy, it does so in the presence of a staggered sublattice potential in monolayer graphene. The lifting occurs for all values of k, except for $k = 0$, contrarily to the biased bilayer, where it is only significant around the K (K') points. Moreover, the effect is stronger in monolayer graphene than it is in bilayer graphene.

As long as the Rashba coupling is zero, an analytical solution for the energy bands can be found. This solution is given by

$$\begin{aligned} E(k)^{\pm,\pm,\pm} = \pm\frac{1}{\sqrt{2}}\Bigg[& t_\perp^2 + 2V^2 + 2t^2|\gamma|^2 + 2\Delta_{SO}^2\eta_k^2 \\ & \pm \Bigg(t_\perp^4 + 4t^2 t_\perp^2|\gamma|^2 + 16t^2V^2|\gamma|^2 \\ & + 16\Delta_{SO}^2V^2\eta_k^2 \pm 8t_\perp^2\Delta_{SO}V\eta_k \Bigg)^{\frac{1}{2}} \Bigg]^{\frac{1}{2}}. \end{aligned} \tag{4.11}$$

In this expression, the three $\pm$ correspond with conduction/valence band, upper/lower layer isospin (symmetric or antisymmetric combination of top and bottom layer states), and spin up/down respectively. It is clear that, if either V, Δ_{SO}, or $t_\perp$ is zero the bands become degenerate, since in this case the last term with the $\pm$ sign vanishes. Another interesting feature that we see only in the particular situation, where $t_\perp, V, \Delta_{SO} \neq 0$ and $t_R = 0$, is a band crossing at $k_x = 0$ (see Fig. 4.7b and Fig. 4.7c and notice the inverted colors at the K and K' points), signalling that the $k_x \to -k_x$ symmetry is lost. This band crossing can be seen analytically from Eq. (4.11). Note that $|\gamma_k|^2$ is symmetric, while η_k is antisymmetric under $k_x \to -k_x$. We conclude that, due to the linear term in η_k, the energy bands satisfies $E(k)^{\pm,\pm,\pm} = E(-k)^{\pm,\pm,\mp}$. Therefore, the individual bands are no longer symmetric under this transformation.

Now, let us investigate the behavior of the system at finite t_R, for $\Delta_{SO} = 0$. First of all, the spin degeneracy is lifted, except at $k_x = 0$. Second, the Mexican-hat feature evolves into something that looks more like an asymmetric farmers hat, see Fig. 4.7d and Fig. 4.8b. Note that if V and/or t_R are increased, the asymmetry

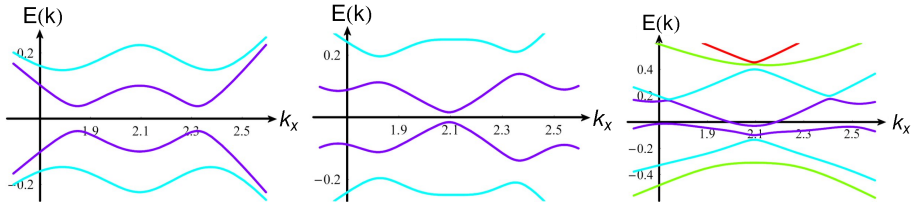

(a) (b) (c)

Figure 4.8: (a) Zoom in on the K point of Fig. 4.7b. (b) Zoom in on the K point of Fig. 4.7d. (c) Zoom in on the K point of Fig. 4.7e. Recall that $V = 0.25$, $t = 1$, $t_\perp = 0.2$, $a = 1$, and $k_y = 2\pi/(\sqrt{3}a)$.

becomes more accentuated and the spectrum does not even look like a farmers hat anymore. We must emphasize that here we do not use any approximation for the energy spectrum, but we keep the full expression. This feature cannot be captured in a zeroth order approximation for the Rashba term, as used by Kane and Mele [78, 79], because at this order of the approximation the spectrum is symmetric around the K (K') point.

If both Δ_{SO} and t_R are finite, the spectrum becomes very complicated (Fig. 4.7e and Fig. 4.7f). As a general trend, Δ_{SO} washes out the Mexican hat feature and at first, increases the difference between spin up and spin down bands around the K (K') points, although the spin degeneracy had been already lifted for all values, except at $k_x = 0$, by the finite Rashba coupling. In addition, particle-hole symmetry is lost. There is no longer a band crossing, but the gap closes and opens again upon increasing Δ_{SO}. Depending on the parameters, a situation can occur where the bands do not touch, but they have common energies, thus there is no gap in the system (see Fig. 4.8c).

4.5 Intra- and inter-layer SO interactions in bilayer graphene

In the previous section we accounted for tunneling between the two layers, but considered only intralayer SO interactions. Now, we investigate the effect of SO interactions between lattice sites in different layers. Since the ISO interaction depends on the symmetry of the graphene plane, it is not obvious if there is any interplane ISO interaction at all. Hence, we focus on the Rashba term. This term only exists in graphene monolayers if the $z \to -z$ mirror symmetry is broken, for example by a perpendicular electric field. Furthermore, the Rashba coefficient can be tuned by varying this electric field. Therefore, we consider here a bilayer system in the presence of a tilted electric field. The inplane component of the electric field

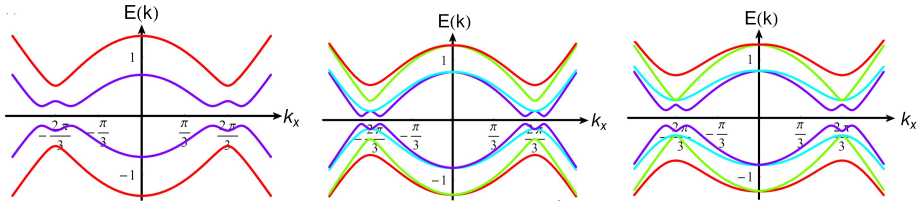

Figure 4.9: (a) Energy spectrum of a biased system, $V = 0.25$, with zero intralayer SO interactions and $t_R^\perp = 0.4$. Compare with Fig. 4.7a. (b) Energy spectrum of an unbiased bilayer system, with zero intralayer Rashba coupling, but with $\Delta_{SO} = 0.15$ and $t_R^\perp = 0.4$. Compare with Fig. 4.4b. (c) Energy spectrum of an unbiased bilayer system, with zero intralayer Rashba coupling, but with $\Delta_{SO} = 0.3$ and $t_R^\perp = 0.4$. Other parameters are $t = 1$, $t_\perp = 0.2$, $a = 1$, and $k_y = 2\pi/(\sqrt{3}a)$.

($\mathbf{E}_\parallel$) gives rise to an interlayer Rashba coupling that is a generalization of Eq. (4.4),

$$H_R^\perp = -it_R^\perp \sum_i a_{i,1}^\dagger \, (\mathbf{s} \times \hat{\mathbf{z}}) \cdot \hat{\mathbf{E}}_\parallel \, b_{i,2} + H.c., \tag{4.12}$$
$$\hat{\mathbf{E}}_\parallel = (\cos\phi, \sin\phi, 0)^T ,$$

where we have chosen to absorb the magnitude of the electric field already in the constant $t_R^\perp$. The orientation of $\mathbf{E}_\parallel$ is determined by ϕ, but the results will be independent of ϕ and therefore we choose $\phi = 0$ arbitrarily. The unit vector connecting the two lattice sites $A_{i,1}$ and $B_{i,2}$ is given by $-\hat{\mathbf{z}}$ and this explains the minus sign in comparison with Eq. 4.4. In k space, Eq. (4.12) becomes

$$H_R^\perp = t_R^\perp \int d^2k \, \Psi^\dagger(k) \, M_{8\times 8}^{R,\perp} \, \Psi(k),$$

where the matrix $M_{8\times 8}^{R,\perp}$ is given by

$$M_{8\times 8}^{R,\perp} = \begin{pmatrix} 0 & C \\ C^\dagger & 0 \end{pmatrix},$$

with

$$C = \begin{pmatrix} 0 & 0 & 0 & -e^{-i\phi} \\ 0 & 0 & e^{i\phi} & 0 \\ 0 & 0 & 0 & 0 \\ 0 & 0 & 0 & 0 \end{pmatrix}.$$

The effect of this interlayer Rashba interaction depends heavily on the other parameters in the theory. Without any intralayer SO interactions, the result of a

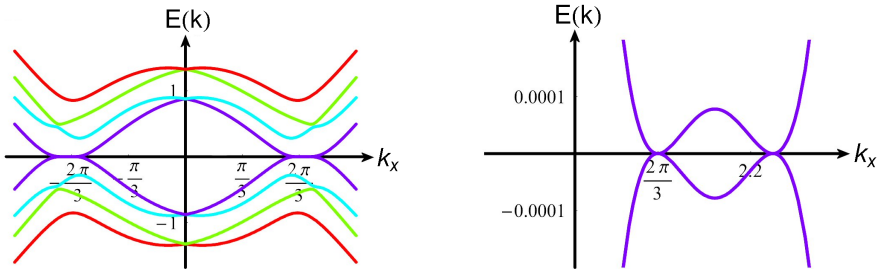

(a) (b)

Figure 4.10: (a) Energy spectrum of an unbiased system with zero intralayer ISO interaction, but $t_R = 0.2$ and $t_R^\perp = 0.4$. Compare with Fig. 4.4d. (b) Zoom in on the K point of (a). Compare with Fig. 4.6a. Other parameters are $t = 1$, $t_\perp = 0.2$, $a = 1$ and $k_y = 2\pi/(\sqrt{3}a)$.

nonzero $t_R^\perp$ is effectively a modification of the interlayer hopping parameter,

$$t_\perp \to t_\perp \sqrt{1 + (t_R^\perp)^2/t_\perp^2}. \tag{4.13}$$

The effect is a slight deformation of the energy bands. Only if $t_R^\perp \gtrsim 0.3$ the shift becomes significant. For a biased system, $t_R^\perp$ will flatten the Mexican hat, as it can be seen in Fig. 4.9a.

The effect of interlayer Rashba coupling is most visible in bilayer systems with zero bias, but with intralayer ISO interactions. Although the energy spectrum can be solved analytically, the equations become too complicated to handle. However, it is clear that the effect is more than a shift of the interlayer hopping parameter. The spin degeneracy of the energy bands is lifted and we see a Mexican hat feature appear in the low lying energy band (see Fig. 4.9b). These low-energy bands are shifted towards the Fermi level and as a consequence the gap between the valence and the conduction bands becomes smaller. If Δ_{SO} is small, the spin degeneracy of the lowest energy band stays intact at the K point, but is lifted around it. However, if Δ_{SO} increases, this degeneracy is lifted and eventually shifted to a degeneracy between the two conduction bands that lay in the middle, as it can be seen in Fig. 4.9c. In comparison with the bilayer without intralayer interactions, the effect of nonzero $t_R^\perp$ manifests itself also for small values of this parameter. In a biased system with intralayer ISO interactions, the effect of the interlayer Rashba coupling is visible, but its influence becomes less important as the bias becomes larger. The effect of a nonzero $t_R^\perp$ in this case is to increase the splitting of the bands around the K (K') points and if $V > \Delta_{SO}$, the Mexican hat is flattened (not shown).

Let us now consider an unbiased system with zero ISO coupling, but with

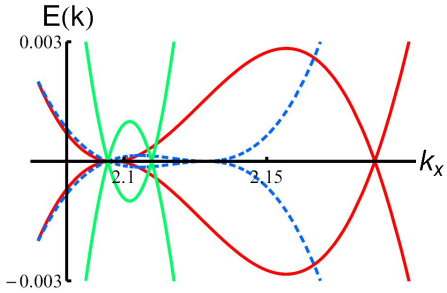

Figure 4.11: Low-energy dispersion for $t_3 = 0.3$ eV, $t_R = 0$ (green/grey line); $t_3 = 0$ eV, $t_R = 0.3$ (blue/dashed line); $t_3 = 0.3$ eV, $t_R = 0.3$ (red/black line). Dirac cones are omitted.

nonzero interlayer and intralayer Rashba coupling. We would have such a system if a tilted electric field is present. The relative strength of both interactions can be tuned independently by changing the parallel and perpendicular components of the electric field. This case is a generalization of the situation that lead to Fig. 4.4d, which was described in more detail in Fig. 4.5 and Fig. 4.6. The most striking effect of a nonzero $t_R^{\perp}$ is the lifting of the spin degeneracies at the K (K') points, with as main consequence the destruction of the Dirac cones (see Fig. 4.10). The way the lowest lying energy band splits is also affected by the interlayer Rashba coupling. Recall that the K (K') point splits into four due to intralayer Rashba coupling and that the central point had a linear crossing at very low-energy scales. This linear crossing is modified to a higher-order crossing by the interlayer Rashba interaction, as it can be seen in Fig. 4.10. Note that the energy scale of the zoom in at the K point in Fig. 4.10 has decreased by a factor fifty with respect to Fig. 4.6. This is also due to the interlayer Rashba coupling.

If all parameters are nonzero the spectrum is very complicated. Interlayer Rashba coupling does deform this spectrum, but we could not detect any special feature that would justify exhibiting them.

4.6 Effect of other hopping parameters

Until now we have completely neglected n.n.n. hopping parameters. However, the values of the t_3 and t_4 parameters in the Slonczewski-Weiss-McClure (SWMc) model [63, 91] are comparable in magnitude with the values that we use for the SO interactions. In the SWMc model, t_3 is the amplitude for $B_1 - A_2$ interlayer hopping, while t_4 describes either $A_1 - A_2$ or $B_1 - B_2$ hopping. There is a disagreement between the theoretical predictions and the experimental verifications of these parameters. Theoretically, t_3 is predicted to have a value of $t_3 = 0.3$ eV $\approx 0.1t$

[91], while from experiments one obtains that this parameter is a factor of three smaller, $t_3 = 0.1$ eV $\approx 0.033t$ [133]. There is more agreement about the value of t_4, namely $t_4 \approx 0.12 - 0.15$ eV $\approx 0.05t$ [91]. In monolayer graphene experiments, the Rashba coupling can be tuned already up to 0.2 eV $\approx 0.068t$ [121] and this is comparable with the magnitude of the parameters we neglected. In this section we consider the SWMc model, which includes the n.n.n. hopping parameters t_3 and t_4, and verify whether the main results of the previous sections remain valid. Notice that in the previous sections we took the hopping parameter $t = 1$ eV, whereas its real value is $t = 3$ eV. Here we will use parameter values as realistic as possible and consider the most general model with higher order hopping terms. Since the effects due to Δ_{SO} would only be visible for values of this parameter much larger than experimentally realizable, and these effects are not altered by the higher order hopping terms, we will not include the intrinsic SO interaction here. In fact, Fig. 4.4,Fig. 4.7,Fig. 4.8, and Fig. 4.9 remain almost unaltered in the framework of the full SWMc model.

The effect of t_3 on an unbiased bilayer without SO interactions is to introduce a splitting of the Dirac cone into four, the so-called trigonal distortion [91]. Indeed this effect, shown as the green line in Fig. 4.12a, is similar to the one produced by the intralayer Rashba interaction (blue dashed line in Fig. 4.12a). However, the splitting due to t_3 is smaller and the satellite points have a linear dispersion instead of the higher order crossing we found in the bilayer with Rashba coupling. Remarkably, the two effects reinforce each other, as it is shown by the red line in the same figure. For certain values of the parameters t_R and t_3, a situation can occur in which we can observe, instead of one satellite point as in the red curve of Fig. 4.12, two satellite points in the $k_y = 2\pi/(\sqrt{3}a)$ direction (not shown). In fact, there are a total of seven touching points between the valence and the conduction bands in this

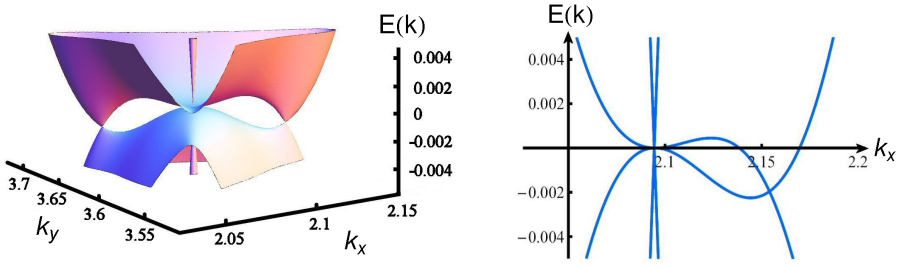

(a) (b)

Figure 4.12: (a) Low-energy dispersion for parameter values $t_3 = 0.3$ eV, $t_4 = 0.1$ eV and $t_R = 0.2$ eV. (b) Cross section cut of (a) along the line $k_y = 2\pi/(\sqrt{3}a)$. Other parameter values are $t = 3$ eV, $t_\perp = 0.4$ eV, and $a = 1$.

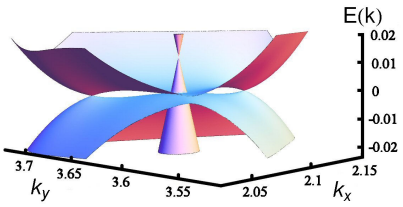

Figure 4.13: Plot for all parameters of the SWMc model nonzero. $t = 3$ eV, $t_\perp = 0.4$ eV, $a = 1$, $t_3 = 0.3$ eV, $t_4 = 0.1$ eV, $\delta = 0.018$ eV, and $t_R = 0.2$ eV.

case, namely two satellite points in three different directions and the central point. The strength of the Rashba coupling that is needed to enter this regime depends heavily on the value of t_3. For the theoretical value $t_3 = 0.3$ eV, the extra satellite points are visible on an energy scale of 0.01 meV, in the regime where $t_R \lesssim 0.4t_3$ or $t_R \gtrsim 3t_3$, while for the experimental value, $t_3 = 0.1$ eV, the extra satellite points can be seen (on the same energy scale), if $t_R \gtrsim 2t_3$. Since in the experimentally accessible cases the associated energies are very small, we do not go into further detail about the extra satellite points here. Another effect of the trigonal distortion is that the crossing of the bands at the satellite points becomes linear instead of higher order. However, the spin polarized Dirac cone remains intact. The formation of this Dirac cone due to an intralayer Rashba coupling is therefore not affected by nonzero values for t_3.

If one also includes $A_1 - A_2$ and $B_1 - B_2$ hopping via the parameter t_4, the particle-hole symmetry is broken. This has consequences for the satellite points. In fact, the band crossing at these points is shifted below the Fermi level. This means that the conduction and the valence bands will overlap as can be seen in Fig. 4.12b and Fig. 4.12c. Although it is possible, for certain parameter values, that the bands do not touch at all outside the K (K') points, they will touch for realistic values of t_3 and t_4, but no longer at the Fermi energy (Fig. 4.12b and Fig. 4.12c). Again, the Dirac cone is still present, and there is no visible difference with the cone in the simplest model (not shown). There are still two different, spin polarized, low-energy excitations, namely massless and massive quasi particles. The difference is that before, the Fermi surface consisted of four points, whereas now it consists of a central point and three satellite pockets. The transport behavior should then change from semiconducting to metallic, when accounting for the t_4 term.

The SWMc model includes also a parameter $\delta \approx 0.018$ eV [91], which is related to the onsite energy difference between stacked and unstacked sites. The sites that lie opposite to each other (A_1 and B_2) have a higher energy than the sites which are placed opposite to a honeycomb center. To incorporate this effect, an extra term is added to the Hamiltonian, $H_\delta = \delta \sum_i \left(a_1^\dagger a_1 + b_2^\dagger b_2 \right)$. This term affects the Dirac cone. However, it does not destroy it, but merely shifts the cone above the Fermi energy, as can be seen in Fig. 4.13. The shape of the cone remains unaltered. In fact, Fig. 4.5b, which shows the slope of the cone, is exactly the same in the full SWMc model as it was in the simplified model we used before (not shown).

A last natural term to include into the model is an intralayer n.n.n. hopping.

This term shifts the position of the K and K' points along the energy axis. By doping the system, it is possible to shift the Fermi energy by the same amount and the final system would be identical to the one considered before. Therefore, this term is usually omitted.

4.7 Conclusions

We studied a graphene bilayer including both, the intrinsic and the Rashba SO interactions and we found that these interactions can modify the energy dispersion in a nontrivial way.

First, we concentrated on the unbiased system and considered only intralayer interactions. We observed that the ISO interaction can open a gap in the system, in the same way as it does for monolayer graphene [79]. On the other hand, if only an intralayer Rashba SO interaction is present, the energy bands are completely different than for monolayer graphene. The K (K') points still split into four, but at very low energies the off center points have now a higher order crossing instead of the linear crossing present in monolayer graphene (Fig. 4.6a). The most striking feature, however, is the formation of a Dirac cone out of an energy band that once was parabolic (Fig. 4.5b). This Dirac cone is located exactly at the former K (K') point. The intralayer Rashba interaction not only lifts the spin degeneracy of the energy bands, but also changes their individual behavior. If both the intralayer ISO and Rashba terms are nonzero, the Dirac cone is destroyed and the particle-hole symmetry is broken.

The presence of a Dirac cone in unbiased bilayer graphene is a very special feature. Together with the split K (K') point, the spectrum that we found will give rise to two different low-energy excitations, one of which is massless. The speed with which this massless excitation travels depends on the Rashba constant (see Fig. 4.6b), which can be tuned by the perpendicular electric field. We expect that the dispersion relation shown in Fig. 4.6a could be observed with angle-resolved photoemission spectroscopy (ARPES) experiments, which have already successfully demonstrated the Dirac dispersion in graphite [134].

In a biased system with nonzero ISO interactions, the spin degeneracy of the energy bands is lifted. The splitting occurs only around the K (K') points. We also observe a band crossing at the $k_x = 0$ point (Fig. 4.7c and Fig. 4.7d). A bias voltage, in combination with the intralayer Rashba coupling, destroys the Dirac cones and the spectrum becomes asymmetric around the K (K') points.

Next, we considered an interlayer Rashba interaction between the planes. This interlayer interaction would in principle be expected to be small compared to the intralayer one because of the larger interlayer atomic separation. However, this effect could still be important if pressure is applied to approach the two layers.

In our model, the interlayer Rashba coupling finds its origin in the presence of a tilted electric field. In a bilayer system with no intralayer SO interactions, this interaction causes effectively a shift of the interlayer hopping parameter. However, in a system where the intralayer SO couplings are nonzero, we see a clear effect in the energy spectrum. In an unbiased system with nonzero Δ_{SO}, the spin degeneracy of the bands is lifted around the K (K') points and a Mexican-hat feature appears. The Mexican-hat feature is known to arise in the bilayer system in the presence of a bias voltage [126]. Here, however, we found that it can also appear without a bias, but solely due to SO interactions. Moreover, the Mexican-hat band in the energy dispersion is fully spin polarized. If the Δ_{SO} parameter becomes large enough, the degeneracy of the two lowest lying conduction bands at the K (K') points is shifted to the two middle bands. The system then becomes isospin degenerate. Indeed, in the presence of tunneling, a bilayer can be described as a two-level system, where the energy bands in each layer have combined into symmetric and antisymmetric energy bands, separated by a gap given by the tunneling energy. If we represent the asymmetric band by an isospin up and the symmetric one by an isospin down, we see that the ISO interaction can lead to an isospin degeneracy at the K and K' points, although the spins remain fully polarized.

If the ISO interaction is absent, but the intralayer Rashba is nonzero, we have seen in Fig. 4.10 that the effect of the interlayer Rashba interaction is to destroy the Dirac cone at the K (K') point and to modify the way the K (K') point splits into four. We can no longer observe a linear crossing for the central point and the energy scales associated with this splitting are substantially smaller.

Finally, we have checked the validity of our results when other parameters of the SWMc model are included. The higher-order hopping terms only affect the low-energy part of the spectrum, hence, only the results for an unbiased bilayer with nonzero intralayer Rashba interactions are visibly altered. The higher order hopping term t_3 induces a trigonal distortion, a behavior which is also produced by the intralayer Rashba interaction. When both terms are present, the effect is amplified and the satellite points will lie further away from the center. On the other hand, the n.n.n. hopping term t_4 breaks the particle-hole symmetry and shifts the touching points of the bands below the Fermi level, see Fig. 4.12b and Fig. 4.12c. In all cases, the spin polarized Dirac cone stays intact. When including the parameter δ of the SWMc model, which accounts for the energy difference between sites that lie opposite to each other and sites that lie opposite to a honeycomb center, we find that the cone is shifted away from the Fermi energy. The energy spectrum including all the parameters of the SWMc model is shown in Fig. 4.13.

Now, we would like to discuss the possibility of observing experimentally the effects that we have described above. In monolayer graphene, the current estimates are that the ISO interaction is very small ($0.0011 - 0.05$ meV) [116]. However,

it is already possible to tune the Rashba coupling in a graphene layer on a Ni substrate up to $t_R \sim 0.2$ eV [121]. Because these values should be representative for bilayer graphene as well, we expect that the results we found involving the Rashba interaction are well within the experimental reach. We believe that it should be possible to detect the Dirac cone that arises from the intralayer Rashba term in an unbiased bilayer. If this Dirac cone can be detected and if it is destroyed by an in-plane electric field, we would have an indication that indeed an interlayer Rashba interaction is present in the system.

The values we used for Δ_{SO} are larger than indicated experimentally. However, we should recall that the same kind of system could be engineered using cold atoms in optical lattices, and in this case there is much less constraint on the parameters of the model. It is already possible to create a two-dimensional honeycomb optical lattice [135] and if a bilayer system could be mimicked, it should be possible to measure the single particle spectrum [136]. In any case, our aim here was mainly to draw a comparison of the different effects of the Rashba and ISO interactions to determine the trend introduced by each one.

A next step would be to include edge states in the model. If we regard the intralayer ISO interaction and the bias voltage in bilayer graphene as being comparable with the ISO interaction and a staggered sublattice potential in monolayer graphene, there is a possibility that the bilayer system would exhibit a phase transition, equivalent to the one described in Ref. [78]. It is already known that there are two types of edge states in bilayer graphene [137], but SO interactions have not yet been taken into account. We hope that our results will motivate further theoretical studies and experiments in the field.

Acknowledgements

We acknowledge financial support from the Netherlands Organization for Scientific Research (NWO). We are grateful to, N. Sandler, W. Beugeling, and A. Lazarides for fruitful discussions. In particular we would like to thank A.H. Castro Neto and M. Goerbig for their comments on the first draft of this Chapter.

Chapter 5

Ferromagnetism in ABA-stacked trilayer graphene

Abstract

We study the ground-state properties of an ABA-stacked trilayer graphene. The low-energy band structure can be described by a combination of both a linear and a quadratic particle-hole symmetric dispersion, reminiscent of monolayer and bilayer graphene, respectively. The multiband structure offers more channels for instability towards ferromagnetism when the Coulomb interaction is taken into account. Indeed, if one associates a subband-index $1/2$ *degree of freedom to the bands (parabolic and linear), it is possible to realize also a band-ferromagnetic state, where there is a shift in the energy bands, since they fill up differently. By using a variational procedure, we compute the exchange energies for all possible variational ground states and identify the parameter space for the occurrence of spin- and band-ferromagnetic instabilities as a function of doping and interaction strength.*[1]

5.1 Introduction

The successful isolation of a one atom thick carbon layer, graphene, has attracted enormous interest in the field of condensed matter [1, 10]. One intriguing aspect of the problem is that, upon coupling a finite number of graphene layers, novel and unexpected properties emerge. Compared to the strong sp^2 bonding between carbon atoms within the graphene sheet, the weak van der Waals force between the layers allows for the formation of different hybridized N-layered configurations. The resulting system is then different from both its 2D (graphene) and its 3D (graphite) counterparts, and depends strongly on the number of layers and on how the stacking is realized. The investigation of multilayer graphene may open

[1] This Chapter is based on *Spin and band ferromagnetism in trilayer graphene*, R. van Gelderen, L.-K. Lim, and C. Morais Smith, Phys. Rev. B **84**, 155446 (2011).

new avenues in the understanding of graphene's electronic properties and in the field of device engineering [138, 139].

Many of the unique electronic properties of monolayer graphene, as opposed to the more conventional GaAs 2D electron gas, originate from the geometry of the honeycomb lattice. These include the peculiar gapless Dirac-cone dispersion [10], the unconventional integer quantum Hall effect [26, 35], and Klein tunneling [33], to name a few. On the other hand, multilayer graphene exhibits different but equally interesting features. While the particle-hole symmetry is generally preserved in the band structure obtained in the most simplified descriptions, the number of conical points and the low-energy dispersion both depend sensitively on the stacking configuration of the N-layered structure and on the model used. For example, in the minimal tight-binding model for the so-called Bernal stacking of a bilayer graphene, the conduction and valence bands touch at the same two points in the Brillouin zone as they do in monolayer graphene, but disperse quadratically instead of linearly. This feature has attracted much interest because it allows for strong electron correlations to take place [140, 141]. On the other hand, a more in depth density functional theory shows that, due to trigonal warping effects, the conduction and valence bands intersect linearly at points which are no longer located at the corners of the Brillouin zone, resulting in a more complex picture [142]. Very recently, broken-symmetry states have been observed due to interaction effects in suspended bilayer graphene [143, 144, 145, 146]. Although a complete characterization of their properties is still lacking, there are some interesting theoretical proposals for the observed states: a nematic state [141] or a quantum anomalous Hall state with spontaneously broken time-reversal symmetry [147, 148]. For another example, the relative twist angle in a bilayer graphene can lead to a highly complex Moiré band structure, which requires a description beyond the standard Bloch's band picture [149]. In fact, at a particular twisting angle, the van Hove singularity of the usual graphene band structure can become observable at a relatively low energy of a few meV [56]. Since high quality samples of N-layered graphene are now becoming accessible experimentally, their anticipated new properties are just about to be unraveled.

In trilayer graphene, the transport properties are also different, depending on the stacking order: at the Dirac point, the ABA-stacked trilayer (Fig. 5.1) is a semimetal, whereas the ABC one is a semiconductor. The electronic band structure in ABC-stacked trilayer graphene was determined using an effective mass approximation [61] and using an *ab-initio* density functional theory [98]. Both methods indicate a semiconductor with zero gap, whereas recent transport measurements suggest a nonzero gap [150]. On the other hand, for ABA-stacked trilayer graphene, the band structure was calculated in the presence of external gates using a self-consistent Hartree approximation [151]. In the absence of a gate, the low-energy spectrum consists of superimposed linear and quadratic bands, which

touch at $\mathbf{k} = 0$. In the presence of a magnetic field, the plateau structure in the Hall conductivity is also determined by the stacking order. Very recently, the integer quantum Hall effect was experimentally observed in an ABC-stacked sample [62, 152]. It was shown that the effect is similar to the one observed in monolayer graphene [26, 35], except for the first plateau at filling factor $\nu = 2$, which was not observed in the trilayer sample. Indeed, this plateau is governed by the chirality of the quasiparticles, which is 1, 2, and 3 for monolayer, bilayer, and trilayer graphene, respectively. The corresponding Berry phases are thus π, 2π, and 3π, respectively. With regard to the ABA stacking, the problem of low mobility has been recently overcome by growing the sample on a high-quality hexagonal boron nitride substrate, which reduces the carrier scattering [99]. The peculiar crossing of the Landau levels due to the massive and massless sub-bands has allowed for a direct determination of the Slonczweski-Weiss-McClure model parameters used to describe the electronic structure of the material [64, 63].

We focus here on the ground-state properties of trilayer graphene in the ABA-stacking configuration in the presence of interactions. The ground state of N-layer undoped graphene is usually assumed to be the state in which the energy bands are filled up to the Dirac point. However, the energy bands are spin degenerate and the formation of pockets of opposite sign in the two spin degenerate bands leads to a gain in exchange energy. This gain in exchange energy is accompanied by a cost in kinetic energy. In monolayer graphene, the cost in kinetic energy is large enough to prevent any ferromagnetic instabilities [153]; only if the interaction would be tuned to unphysical values one would observe the spontaneous generation of spin-up and spin-down pockets. In bilayer graphene the situation is different. The leading-order term in the exchange energy is one order lower in the pocket size than the kinetic energy is. Therefore, the exchange interaction dominates and pockets will form with a size, in k space, of order $Q \approx 0.05 t_\perp$, where $t_\perp$ is the interlayer hopping energy in dimensionless units and Q is measured in units of some cut off [154]. Hence, bilayer graphene has a small ferromagnetic instability. The coexistence of a parabolic and a linear bands in ABA-stacked trilayer graphene opens the way to investigate, next to ordinary ferromagnetic instabilities (Fig. 5.2a), also the 'band ferromagnetism' phenomenon. With band ferromagnetism we mean that the two bands (linear and parabolic) become shifted with respect to each other (the crossing point of the

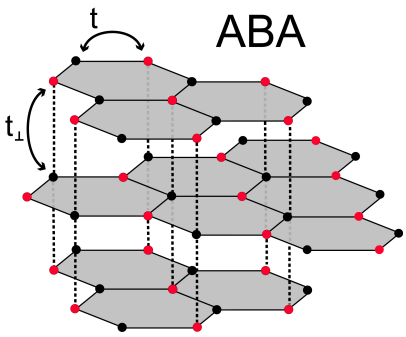

Figure 5.1: ABA-stacked trilayer graphene with the various hopping parameters.

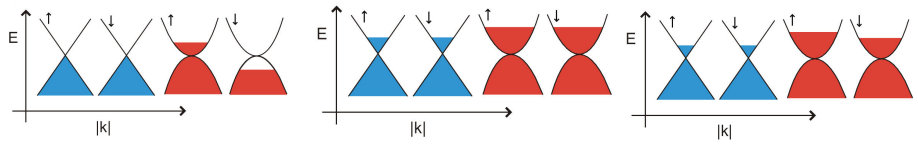

(a) (b) (c)

Figure 5.2: Sketch of (a) the spin-ferromagnetic state in an undoped trilayer, (b) the band-ferromagnetic state in a doped trilayer, and (c) a configuration which is both spin- and band-ferromagnetic in a doped trilayer.

linear and parabolic conduction and valence bands no longer overlap), or alternatively, that the bands fill up to different Fermi energies (see Fig. 5.2b). In the following, we will generalize the approach used in Refs. [153] and [154] to investigate ferromagnetic instabilities in trilayer graphene. We will show that spin- and band-ferromagnetism may occur both separately and simultaneously (Fig. 5.2c). This chapter is organized as follows: In section 5.2 we introduce the model that we use in section 5.3 to compute (band) ferromagnetic instabilities for both undoped and doped trilayer graphene. Our conclusions are presented in section 5.4.

5.2 The Model

In this Chapter, we use a tight-binding approximation to model trilayer graphene and perform an expansion around the K point. The low-energy Hamiltonian around the K point is given by

$$H = \sum \Psi^{\dagger}_{\mathbf{p},\sigma} \mathcal{H}(\mathbf{p}) \Psi_{\mathbf{p},\sigma},$$

where $\Psi^{\dagger}_{\mathbf{p},\sigma} = (a^{\dagger}_{1,\mathbf{p},\sigma}, b^{\dagger}_{1,\mathbf{p},\sigma}, a^{\dagger}_{2,\mathbf{p},\sigma}, b^{\dagger}_{2,\mathbf{p},\sigma}, a^{\dagger}_{3,\mathbf{p},\sigma}, b^{\dagger}_{3,\mathbf{p},\sigma})$,

$$\mathcal{H}(\mathbf{p}) = \begin{pmatrix} 0 & v_F p e^{i\phi(\mathbf{p})} & 0 & -t_\perp & 0 & 0 \\ v_F p e^{-i\phi(\mathbf{p})} & 0 & 0 & 0 & 0 & 0 \\ 0 & 0 & 0 & v_F p e^{i\phi(\mathbf{p})} & 0 & 0 \\ -t_\perp & 0 & v_F p e^{-i\phi(\mathbf{p})} & 0 & -t_\perp & 0 \\ 0 & 0 & 0 & -t_\perp & 0 & v_F p e^{i\phi(\mathbf{p})} \\ 0 & 0 & 0 & 0 & v_F p e^{-i\phi(\mathbf{p})} & 0 \end{pmatrix}, \tag{5.1}$$

and the sum is over all relevant quantum numbers. Here, $a^{\dagger}_{i,\mathbf{p},\sigma}$ ($b^{\dagger}_{i,\mathbf{p},\sigma}$) creates a particle with momentum $\mathbf{p}$ and spin σ at the A (B) sublattice in the i-th layer

($i = 1, 2, 3$), $t_\perp \approx 0.35$ eV is the interlayer hopping energy, $v_F = (3/2)at$ denotes the Fermi velocity, with $a = 0.142$ nm the lattice spacing and $t \approx 3$ eV the nearest-neighbor hopping energy, p is the norm of the momentum vector $\mathbf{p} = (p_x, p_y)$ and $\phi(\mathbf{p}) = \arctan(p_y/p_x)$. Note that if one would have expanded around the K' point, we would have found a Hamiltonian where $\phi(\mathbf{p})$ would be replaced by $\pi - \phi(\mathbf{p})$ in Eq. (5.1). Since we neglect intervalley interactions, we do not need to take this into account and we simply multiply our results by a factor two.

The low-energy approximation that we use here is only valid when the momentum is much smaller than some critical momentum $p \ll k_c$. In Ref. [155] this momentum is approximated to be $k_c a \sim 1/2$ for monolayer and this value is also valid in our case. If one takes the full band dispersion into account, the bands differ from their linear and parabolic shapes. We found that for $pa = 0.1$ the low-energy approximation is accurate within four percent. Since the momenta that occur in this Chapter are well below this value, our low-energy approximation is applicable.

We perform a change of basis, $\Psi \to U\Psi$, with

$$U = \frac{1}{\sqrt{2}} \begin{pmatrix} 1 & 0 & 0 & 0 & -1 & 0 \\ 0 & 1 & 0 & 0 & 0 & -1 \\ 1 & 0 & 0 & 0 & 1 & 0 \\ 0 & 1 & 0 & 0 & 0 & 1 \\ 0 & 0 & 0 & \sqrt{2} & 0 & 0 \\ 0 & 0 & \sqrt{2} & 0 & 0 & 0 \end{pmatrix},$$

to bring the Hamiltonian into the form $\tilde{H} = \sum \tilde{\Psi}^\dagger_{\mathbf{p},\sigma} \tilde{\mathcal{H}}(\mathbf{p}) \tilde{\Psi}_{\mathbf{p},\sigma}$, where

$$\begin{aligned} \tilde{\Psi}^\dagger_{\mathbf{p},\sigma} = \frac{1}{\sqrt{2}}([a^\dagger_{1,\mathbf{p},\sigma} - a^\dagger_{3,\mathbf{p},\sigma}], [b^\dagger_{1,\mathbf{p},\sigma} - b^\dagger_{3,\mathbf{p},\sigma}], \\ [a^\dagger_{1,\mathbf{p},\sigma} + a^\dagger_{3,\mathbf{p},\sigma}], [b^\dagger_{1,\mathbf{p},\sigma} + b^\dagger_{3,\mathbf{p},\sigma}], \\ \sqrt{2} b^\dagger_{2,\mathbf{p},\sigma}, \sqrt{2} a^\dagger_{2,\mathbf{p},\sigma}), \end{aligned}$$

$$\tilde{\mathcal{H}}(\mathbf{p}) = U\mathcal{H}(\mathbf{p})U^{-1} = \begin{pmatrix} \mathcal{H}_{ml}(\mathbf{p}) & 0 \\ 0 & \mathcal{H}_{bl}(\mathbf{p}) \end{pmatrix},$$

$$\mathcal{H}_{ml}(\mathbf{p}) = \begin{pmatrix} 0 & v_F p e^{i\phi(\mathbf{p})} \\ v_F p e^{-i\phi(\mathbf{p})} & 0 \end{pmatrix},$$

$$\mathcal{H}_{bl}(\mathbf{p}) = \begin{pmatrix} 0 & v_F p e^{i\phi(\mathbf{p})} & -\sqrt{2}t_\perp & 0 \\ v_F p e^{-i\phi(\mathbf{p})} & 0 & 0 & 0 \\ -\sqrt{2}t_\perp & 0 & 0 & v_F p e^{i\phi(\mathbf{p})} \\ 0 & 0 & v_F p e^{-i\phi(\mathbf{p})} & 0 \end{pmatrix}.$$

Thus, the trilayer can be described as a combination of a monolayer and a bilayer with a modified interlayer hopping energy. Note that in the new basis, the

basis vectors that are associated with the monolayer part are odd under reflection with respect to the middle plane, while the ones that describe the bilayer are even under this transformation. The hopping parameters γ_2 and γ_5 from the Slonczewski-Weiss-McClure (SWMc) model, or a voltage difference between the top and bottom layer break this reflection symmetry and couple the blocks in the trilayer Hamiltonian [138]. We will neglect those terms here.

Since the Hamiltonian has a block form and we know how to diagonalize the different blocks, it is now a trivial task to bring it into a diagonal form. Using the results from Refs. [153] and [154], we find that $\tilde{\mathcal{H}}(\mathbf{p})$ can be diagonalized as follows:

$$\begin{aligned}\mathcal{D}(\mathbf{p}) &= W^\dagger(\mathbf{p})\tilde{\mathcal{H}}(\mathbf{p})W(\mathbf{p}) = W^\dagger(\mathbf{p})U\mathcal{H}(\mathbf{p})U^{-1}W(\mathbf{p}) \\ &\equiv Z^\dagger(\mathbf{p})\mathcal{H}(\mathbf{p})Z(\mathbf{p}), \\ W(\mathbf{p}) &= \begin{pmatrix} V(\mathbf{p}) & 0 \\ 0 & M(\mathbf{p}) \end{pmatrix},\end{aligned}$$

where $V(\mathbf{p})$ and $M(\mathbf{p})$ are the matrices that diagonalize the monolayer and bilayer Hamiltonian respectively,

$$\begin{aligned}V(\mathbf{p}) &= \frac{1}{\sqrt{2}}\begin{pmatrix} -e^{i\phi(\mathbf{p})} & 1 \\ 1 & e^{-i\phi(\mathbf{p})} \end{pmatrix}, \\ M(\mathbf{p}) &= M_1(\mathbf{p})M_2M_3(\mathbf{p}), \\ M_1(\mathbf{p}) &= \begin{pmatrix} 1 & 0 & 0 & 0 \\ 0 & e^{-i\phi(\mathbf{p})} & 0 & 0 \\ 0 & 0 & 1 & 0 \\ 0 & 0 & 0 & e^{i\phi(\mathbf{p})} \end{pmatrix}, \\ M_2 &= \frac{1}{\sqrt{2}}\begin{pmatrix} 1 & 0 & 1 & 0 \\ 0 & 1 & 0 & 1 \\ 1 & 0 & -1 & 0 \\ 0 & 1 & 0 & -1 \end{pmatrix}, \\ M_3(\mathbf{p}) &= \begin{pmatrix} \cos\varphi(\mathbf{p}) & \sin\varphi(\mathbf{p}) & 0 & 0 \\ -\sin\varphi(\mathbf{p}) & \cos\varphi(\mathbf{p}) & 0 & 0 \\ 0 & 0 & \cos\varphi(\mathbf{p}) & -\sin\varphi(\mathbf{p}) \\ 0 & 0 & \sin\varphi(\mathbf{p}) & \cos\varphi(\mathbf{p}) \end{pmatrix}.\end{aligned}$$

In the last matrix, $\varphi(\mathbf{p})$ is defined by the relation $\tan[2\varphi(\mathbf{p})] = v_F\sqrt{2}p/t_\perp$. This result differs by a factor $\sqrt{2}$ from Ref. [154] because of the modified interlayer hopping parameter in $\mathcal{H}_{bl}$. The energy bands are given by the nonzero entries of the matrix $\mathcal{D}(\mathbf{p})$,

$$\begin{aligned}\mathcal{D}(\mathbf{p}) = \mathrm{diag}\big\{ &-v_Fp,\ v_Fp,\ [-t_\perp - \xi(p)]/\sqrt{2}, \\ &[-t_\perp + \xi(p)]/\sqrt{2},\ [t_\perp + \xi(p)]/\sqrt{2},\ [t_\perp - \xi(p)]/\sqrt{2}\big\},\end{aligned}$$

where $\xi(p) = \sqrt{t_\perp^2 + 2v_F^2 p^2}$.

The next step is to implement the Coulomb interaction in the model. Since we consider only weakly doped trilayers in this Chapter, the Coulomb interaction is only slightly screened and therefore long ranged,

$$\begin{aligned} H_I = \frac{1}{2}\int d^2\mathbf{x}\, d^2\mathbf{y}\big\{ & V^{\mathrm{D}}(\mathbf{x}-\mathbf{y})[\rho_1(\mathbf{x})\rho_1(\mathbf{y}) + \rho_2(\mathbf{x})\rho_2(\mathbf{y}) \\ & + \rho_3(\mathbf{x})\rho_3(\mathbf{y})] + V^{\mathrm{ND}}(\mathbf{x}-\mathbf{y})[\rho_1(\mathbf{x})\rho_2(\mathbf{y}) \\ & + \rho_2(\mathbf{x})\rho_1(\mathbf{y}) + \rho_2(\mathbf{x})\rho_3(\mathbf{y}) + \rho_3(\mathbf{x})\rho_2(\mathbf{y})] \\ & + V^{\mathrm{2ND}}(\mathbf{x}-\mathbf{y})[\rho_1(\mathbf{x})\rho_3(\mathbf{y}) + \rho_3(\mathbf{x})\rho_1(\mathbf{y})]\big\}, \end{aligned} \tag{5.2}$$

where $\rho_i(\mathbf{x}) = \sum_\sigma \left(a_{i,\sigma}^\dagger(\mathbf{x}) a_{i,\sigma}(\mathbf{x}) + b_{i,\sigma}^\dagger(\mathbf{x}) b_{i,\sigma}(\mathbf{x}) \right)$ is the density of electrons in the ith layer and the interaction potentials for the in-plane (D), the nearest-neighbor planes (ND) and the next-nearest-neighbor planes (2ND) are given by

$$\begin{aligned} V^{\mathrm{D}}(\mathbf{x}-\mathbf{y}) &= \frac{e^2}{\epsilon|\mathbf{x}-\mathbf{y}|}, \\ V^{\mathrm{ND}}(\mathbf{x}-\mathbf{y}) &= \frac{e^2}{\epsilon\sqrt{d^2+|\mathbf{x}-\mathbf{y}|^2}}, \\ V^{\mathrm{2ND}}(\mathbf{x}-\mathbf{y}) &= \frac{e^2}{\epsilon\sqrt{4d^2+|\mathbf{x}-\mathbf{y}|^2}}. \end{aligned}$$

Here, e is the electron charge, ϵ the dielectric constant of the substrate (of air in the case of suspended graphene), and d the interlayer distance ($d \approx .32$ nm). The form of $V^{\mathrm{ND}}(\mathbf{x}-\mathbf{y})$ can be understood by recalling that $\mathbf{x}$ is a two-dimensional vector. We Fourier transform Eq. (6.3) and express it in terms of symmetric and anti-symmetric combinations of layer densities,

$$\begin{aligned} H_I = \frac{1}{2A}{\sum_{\mathbf{q}}}' \sum_{\alpha=\pm} \big[& \rho_\alpha(\mathbf{q}) V_\alpha(\mathbf{q}) \rho_\alpha(-\mathbf{q}) \\ & + \tilde{\rho}_\alpha(\mathbf{q}) V_\alpha(\mathbf{q}) \tilde{\rho}_\alpha(-\mathbf{q}) + \check{\rho}_\alpha(\mathbf{q}) \check{V}_\alpha(\mathbf{q}) \check{\rho}_\alpha(-\mathbf{q})\big], \end{aligned} \tag{5.3}$$

where the prime on the sum indicates that we omit the $\mathbf{q} = 0$ term, since it is canceled by the neutralizing background (Jellium model), A is the area of the unit

cell, and the different quantities are defined by

$$\rho_{\pm}(\mathbf{q}) = \frac{1}{\sqrt{2}}\left[\rho_1(\mathbf{q}) \pm \rho_2(\mathbf{q})\right], \tag{5.4}$$

$$\tilde{\rho}_{\pm}(\mathbf{q}) = \frac{1}{\sqrt{2}}\left[\rho_3(\mathbf{q}) \pm \rho_2(\mathbf{q})\right], \tag{5.5}$$

$$\check{\rho}_{\pm}(\mathbf{q}) = \frac{1}{\sqrt{2}}\left[\rho_1(\mathbf{q}) \pm \rho_3(\mathbf{q})\right], \tag{5.6}$$

$$V_{\pm}(\mathbf{q}) = \frac{2\pi e^2}{\epsilon q}\left(\frac{1}{2} \pm e^{-qd}\right), \tag{5.7}$$

$$\check{V}_{\pm}(\mathbf{q}) = \frac{2\pi e^2}{\epsilon q}\left(\frac{1}{2} \pm e^{-2qd}\right). \tag{5.8}$$

We want to write this interaction term in the number operators of the energy bands instead of the number operators of the layers. We know how to diagonalize the kinetic term and therefore $\Phi_{\mathbf{p},\sigma} \equiv Z(\mathbf{p})^{\dagger}\Psi_{\mathbf{p},\sigma}$ are the operators that annihilate particles in the different energy bands. As a result, we obtain, $\left(\Phi^{\dagger}_{\mathbf{p},\sigma}\Phi_{\mathbf{p},\sigma}\right)_j = n_{j,\sigma}(\mathbf{p})$, the number operator of the jth energy band, where we have to number the bands as in Fig. 5.3. It is convenient to rewrite the density operators in the diagonal basis,

$$\rho_{\pm}(\mathbf{q}) = \sum_{\mathbf{p}} \Phi^{\dagger}_{\mathbf{p}+\mathbf{q}}\chi^{\pm}(\mathbf{p}+\mathbf{q},\mathbf{p})\Phi_{\mathbf{p}}, \tag{5.9}$$

$$\tilde{\rho}_{\pm}(\mathbf{q}) = \sum_{\mathbf{p}} \Phi^{\dagger}_{\mathbf{p}+\mathbf{q}}\tilde{\chi}^{\pm}(\mathbf{p}+\mathbf{q},\mathbf{p})\Phi_{\mathbf{p}}, \tag{5.10}$$

$$\check{\rho}_{\pm}(\mathbf{q}) = \sum_{\mathbf{p}} \Phi^{\dagger}_{\mathbf{p}+\mathbf{q}}\check{\chi}^{\pm}(\mathbf{p}+\mathbf{q},\mathbf{p})\Phi_{\mathbf{p}}, \tag{5.11}$$

where

$$\chi^{\pm}(\mathbf{p}+\mathbf{q},\mathbf{p}) \equiv \frac{1}{\sqrt{2}} Z^{\dagger}_{\mathbf{p}+\mathbf{q}}\mathrm{diag}(1,1,\pm 1,\pm 1,0,0)Z_{\mathbf{p}}, \tag{5.12}$$

$$\tilde{\chi}^{\pm}(\mathbf{p}+\mathbf{q},\mathbf{p}) \equiv \frac{1}{\sqrt{2}} Z^{\dagger}_{\mathbf{p}+\mathbf{q}}\mathrm{diag}(0,0,\pm 1,\pm 1,1,1)Z_{\mathbf{p}}, \tag{5.13}$$

$$\check{\chi}^{\pm}(\mathbf{p}+\mathbf{q},\mathbf{p}) \equiv \frac{1}{\sqrt{2}} Z^{\dagger}_{\mathbf{p}+\mathbf{q}}\mathrm{diag}(1,1,0,0,\pm 1,\pm 1)Z_{\mathbf{p}}. \tag{5.14}$$

Inserting equations (5.4)-(5.14) into the interaction Hamiltonian (5.3) yields the interaction term that we use for our calculations. We are only interested in the

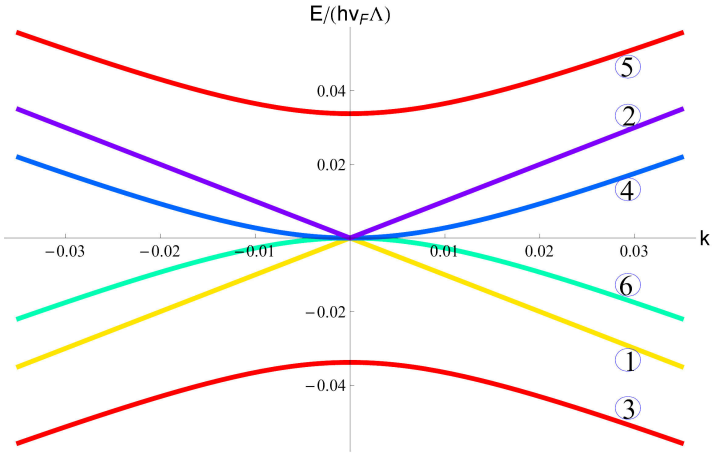

Figure 5.3: The energy spectrum of trilayer graphene. The numbering of the bands is such that $\Phi^\dagger_{\mathbf{p},j}\Phi_{\mathbf{p},j} = n_j$.

exchange energy, which is given by

$$\begin{aligned}\frac{E_{\text{ex}}}{A} = -\frac{1}{2}\int \frac{d^2\,\mathbf{p}}{(2\pi)^2}\frac{d^2\,\mathbf{p}'}{(2\pi)^2}\sum_{\alpha,i,j,\sigma,a} \\ \left[\chi^\alpha_{ij}(\mathbf{p}',\mathbf{p})\chi^\alpha_{ji}(\mathbf{p},\mathbf{p}')V_\alpha(\mathbf{p}'-\mathbf{p})n_{i,\sigma,a}(\mathbf{p}')n_{j,\sigma,a}(\mathbf{p})\right] \\ +\left[\tilde{\chi}^\alpha_{ij}(\mathbf{p}',\mathbf{p})\tilde{\chi}^\alpha_{ji}(\mathbf{p},\mathbf{p}')V_\alpha(\mathbf{p}'-\mathbf{p})n_{i,\sigma,a}(\mathbf{p}')n_{j,\sigma,a}(\mathbf{p})\right] \\ +\left[\check{\chi}^\alpha_{ij}(\mathbf{p}',\mathbf{p})\check{\chi}^\alpha_{ji}(\mathbf{p},\mathbf{p}')\check{V}_\alpha(\mathbf{p}'-\mathbf{p})n_{i,\sigma,a}(\mathbf{p}')n_{j,\sigma,a}(\mathbf{p})\right].\end{aligned} \tag{5.15}$$

In the sum α takes the values $\pm$; i and j label components, hence run from 1 to 6; σ sums over spin, and a over the valley index. We neglected the valley index so far since in our case it only gives rise to an extra factor two, as we choose the same pocket structure for both valleys in our studies.

5.3 Ferromagnetic instabilities

Undoped case

For undoped trilayer graphene, the noninteracting ground state is the configuration in which the three valence bands are completely filled and the conduction bands are completely empty. If an electron or hole pocket forms in one of the bands, this costs kinetic energy. This cost is given by the absolute value of the integral

$\int_0^{E(Q)} dE\, \rho(E)E$, where Q is the pocket size and $\rho(E)$ the density of states. Since for the linear band, $\rho(E) \sim E$ and $E(Q) \sim Q$, one finds that $\Delta E_{\mathrm{kin},l} \sim Q^3$, while for the parabolic band, $\rho(E) \sim E^0$, but $E(Q) \sim Q^2$, hence $\Delta E_{\mathrm{kin},p} \sim Q^4$. In fact, the changes in kinetic energy for a linear band with pockets of size Q_l and a parabolic band with pockets of size Q_p are

$$\Delta E_{\mathrm{kin},l}(Q_l) = \frac{A}{6\pi}\hbar v_F |Q_l|^3,$$
$$\Delta E_{\mathrm{kin},p}(Q_p) = \frac{A}{8\pi}\frac{(\hbar v_F)^2}{\sqrt{2}t_\perp}|Q_p|^4.$$

Since $Q_i < 1$, for $i = l/p$, the creation of linear pockets costs more kinetic energy than the creation of parabolic ones. Trilayer graphene has four energy bands close to the K point, hence there are four different pocket parameters: Q_{lu}, Q_{ld}, Q_{pu}, and Q_{pd}, where l/p stands for linear and parabolic bands and u/d for up and down spins. We are assuming long range interactions and are neglecting the short range part, hence there is no intervalley scattering. We also assume particle number conservation, thus Q_{pd} is not independent from the other variational parameters. For zero doping one has the constraint:

$$s_{lu}\frac{Q_{lu}^2}{4\pi} + s_{ld}\frac{Q_{ld}^2}{4\pi} + s_{pu}\frac{Q_{pu}^2}{4\pi} + s_{pd}\frac{Q_{pd}^2}{4\pi} = 0, \tag{5.16}$$

where $s_{i\sigma} = +1$ for electronlike pockets and $s_{i\sigma} = -1$ for holelike pockets.

One can now vary the pocket parameters and calculate whether the energy is minimized for nonzero pocket sizes (at zero temperature). Our formalism is build

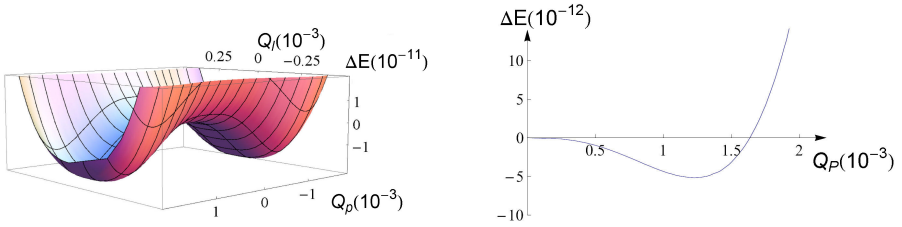

(a) (b)

Figure 5.4: (a) The energy difference $\Delta E(Q_{lu}, Q_{ld}, Q_{pu}, Q_{pd})$ per unit cell (Eq. 5.18) for the undoped trilayer, where we have chosen $Q_{lu} = -Q_{ld} \equiv Q_l$. Because of particle number conservation $Q_{pu} = -Q_{pd} \equiv Q_p$. ΔE is measured in units of $hv_F\Lambda$, Q_l and Q_p are both measured in units of Λ. (b) The energy difference per unit cell $\Delta E(Q_{lu} = 0, Q_{ld} = 0, Q_{pu} = Q_p, Q_{pd} = -Q_p)$. This is a cross section along the $Q_l = 0$ axis of Fig. 5.4a. ΔE is measured in units of $hv_F\Lambda$ and Q_p is measured in units of Λ.

up in such a way that the pocket parameters can take both positive and negative values. A positive Q corresponds to an electron pocket. Hence, the corresponding conduction band (linear/parabolic, up/down) is filled up to momentum Q. A negative Q corresponds to hole pockets, i.e. the corresponding valence bands are depleted up to momentum $|Q|$. This method allows us to obtain the exchange integrals for all possible pocket configurations at once. Using this formalism, we find that the bands fill up according to (see Fig. 5.3 for the numbering of the bands) ,

$$n_u(p) = \begin{pmatrix} 1-\Theta(-Q_{lu}-p) \\ \Theta(Q_{lu}-p) \\ 1 \\ \Theta(Q_{pu}-p) \\ 0 \\ 1-\Theta(-Q_{pu}-p)) \end{pmatrix},$$

$$n_d(p) = \begin{pmatrix} 1-\Theta(-Q_{ld}-p) \\ \Theta(Q_{ld}-p) \\ 1 \\ \Theta(Q_{pd}-p) \\ 0 \\ 1-\Theta(-Q_{pd}-p)) \end{pmatrix},$$

where Θ is the Heaviside step function. Note that one cannot have both electron and hole pockets in the same band at the same time, because if, for example, $Q_{lu} > 0$, then $\Theta(-Q_{lu} - p) = 0$. Hence, in this case, the linear spin-up valence band is completely filled (band 1 in Fig. 5.3), while the linear spin-up conduction band (band 2 in Fig. 5.3) is filled up to momentum $|Q_{lu}|$, corresponding to an electron pocket of size $|Q_{lu}|$.

The integrals that we have to compute have the same structure as the ones in Ref. [154]. The expansion in the pocket parameters is highly nontrivial and very lengthy. Since there are three variational parameters, we have performed the integrals numerically. The expression for the integrals (Eq. 5.15) has many terms and it is not enlightening to write all of them out.

From this point on, we work in dimensionless units by measuring momenta in units of a cutoff Λ, which is estimated using a Debye approximation, in which the number of states is conserved in the Brillouin zone: $\Lambda^2 = 2\pi/A$. We measure energies in units of $\hbar v_F \Lambda(A\Lambda^2) = h v_F \Lambda$. This dimensionless energy corresponds with the energy per unit cell in units of $\hbar v_F \Lambda$. Let us also introduce a dimensionless interaction strength $g = e^2/(\epsilon \hbar v_F)$. Furthermore, we set Λ, $\hbar$ and t equal to unity.

Note that the spin-up and spin-down terms decouple. This allows us to calculate

$$\begin{aligned}\Delta E(Q_l, Q_p) &= \Delta E_{\mathrm{kin}}(Q_l, Q_p) + \Delta E_{\mathrm{ex}}(Q_l, Q_p) \\ &\equiv \Delta E_{\mathrm{kin},l}(Q_l) + \Delta E_{\mathrm{kin},p}(Q_p) + \Delta E_{\mathrm{ex},l}(Q_l) + \Delta E_{\mathrm{ex},p}(Q_p) \\ &\quad + \Delta E_{\mathrm{ex,mixed}}(Q_l, Q_p) \end{aligned} \tag{5.17}$$

on a discrete $N_l \times N_p$ lattice, where we have chosen the values of the pocket parameters such that their squares lie on an equally spaced grid for reasons which will become clear later. After calculating these data points, one can compute

$$\Delta E_{\mathrm{tot}}(Q_{lu}, Q_{ld}, Q_{pu}, Q_{pd}) = \Delta E(Q_{lu}, Q_{pu}) + \Delta E(Q_{ld}, Q_{pd}) \tag{5.18}$$

The next step is to select out the points that satisfy the constraint (5.16) and find the values of the pocket sizes for which the energy is minimized.

For the undoped case, it turns out that the energy is minimized when the pockets in the linear band are zero, while the pockets in the parabolic band have a nonzero value. This is the result that one obtains if a monolayer and a bilayer are superimposed on each other. There is *a priori* no reason for this to be the case because in the exchange integrals there appear terms that are mixed in linear and parabolic pocket parameters. However, their contribution is too small to shift the equilibrium value of the pockets in the linear bands away from zero. In Fig. 5.4a, we have plotted ΔE as function of Q_l and Q_p, where $Q_{pu} = -Q_{pd} \equiv Q_p$ due to particle number conservation and we have chosen $Q_{lu} = -Q_{ld} \equiv Q_l$. Since the spin of the electrons has no preferred direction, one sees two minima in Fig. 5.4a for $Q_l = 0$ and some fixed value of $Q_p = \pm Q_{\mathrm{min}}$. The energy increases if the linear pocket is chosen to be different from zero, while tuning the parabolic pocket away from zero lowers the energy. Although ΔE is small (order of 1 meV per square micrometer), the equilibrium sizes of the pockets are significant (see Fig. 5.4b). The effect is comparable in magnitude with the graphene bilayer. In Fig. 5.5a we display the equilibrium value for Q_p as a function of the interaction strength g (for suspended graphene, g is estimated to be $g \approx 2.3$). The equilibrium value for the linear pocket sizes is zero for this range of the interaction strength.

Since we neglect intervalley scattering, the situation in which both valleys have the same pocket configuration and the system is ferromagnetic is degenerate with the situation in which one valley has a pocket configuration in which the spins are flipped with respect to the other valley and, hence, there is no net magnetization. It is necessary to take intervalley scattering into account to determine which configuration is more favorable. We have numerically determined and compared the exchange energy for both cases and we find that the ferromagnetic state is indeed favorable. Note that this configuration spontaneously breaks time-reversal symmetry, a feature that was also observed in the graphene bilayer [154]. The ground state is twofold degenerate and the two minima are related by time-reversal symmetry.

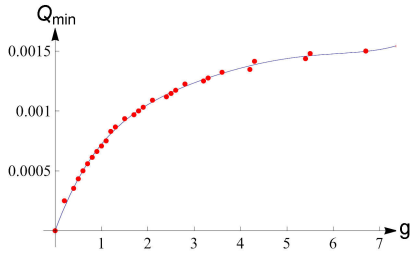

(a)

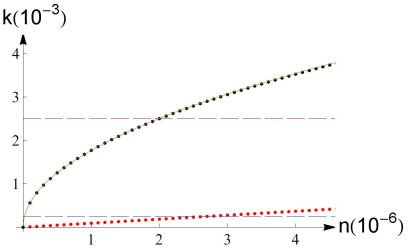

(b)

Figure 5.5: (a) $Q_{\min}$, which is the equilibrium value of Q_p as a function of the dimensionless interaction strength g. $Q_{\min}$ is measured in units of Λ. The line is a polynomial fit to eighth order in g. (b) Plot of Q_l^0 (blue/black dots) and Q_p^0 (grey/grey dots) in units of Λ as a function of doping in units of Λ^{-2}. The red and blue lines mark the interval in which we have chosen our datapoints. The yellow line is a plot of Q_p^0 assuming that $Q_l^0 = 0$.

Doped case

The doped case in trilayer graphene is more subtle than in either a monolayer or a bilayer. For a monolayer and bilayer one can dope the system (with electrons or holes) and the bands (spin up and spin down) will fill up to some Fermi energy, corresponding with this particular doping level. This will be the noninteracting ground state for the doped system. In trilayer graphene this is not the case. If one dopes a graphene trilayer such that both the linear and the parabolic band are filled up to some Fermi energy E_F, it turns out that due to kinetic energy considerations, this is not a stable state. The kinetic energy is minimized when the parabolic band is filled up differently than the linear band. Alternatively, since for a physical system the Fermi energy has a well defined value, one can interpret this result as a shift of the linear and parabolic energy bands with respect to each other. For our discussion, it is more natural to keep the intersection points of the bands in place and, as a consequence, use different Fermi energies for the parabolic and linear bands. By choosing this interpretation, we allow ourselves to use the formalism developed in the previous section.

Since the kinetic energy cost of filling up the linear band goes as $\approx k^3$, this costs more energy than filling up the parabolic band, for which the energy cost goes as $\approx k^4$ (recall that we work in dimensionless units, such that $k < 1$). Let us define $k_F^{l/p,u/d}$ as the momentum to which the linear (parabolic) spin up (down) band fills up when the kinetic energy is minimized. When there is no interaction present the bands will be spin degenerate. Furthermore, we can use the same formalism as for the undoped case. The difference is that, for $g = 0$, the pocketsizes of the

bands are equal to $Q^0_{l/p} = k_F^{l/p,u/d}$. Hence, the constraint (5.16) now reads,

$$\begin{aligned} &s_{lu}\frac{Q^2_{lu}}{4\pi} + s_{ld}\frac{Q^2_{ld}}{4\pi} + s_{pu}\frac{Q^2_{pu}}{4\pi} + s_{pd}\frac{Q^2_{pd}}{4\pi} \\ &= s^0_l\frac{(Q^0_l)^2}{2\pi} + s^0_p\frac{(Q^0_p)^2}{2\pi} \equiv n, \end{aligned} \tag{5.19}$$

where n is the doping level and $s^0_{l/p}$ is the sign of $Q^0_{l/p}$. To determine the values of $Q^0_{l/p}$, one can vary the filling of the bands respecting the constraint and determine for which configuration the kinetic energy is minimized. One can show that $Q^0_l << Q^0_p$ (see Fig. 5.5b). In fact, the resolution we use for calculating the integrals is such that $Q^0_l = 0$. Note that, although $Q^0_l << Q^0_p$, the single-particle energies associated with these momenta are of the same order of magnitude. The linear band is filled to higher energies than the parabolic one, since the latter is very flat. However, in our discussion this is not relevant because the energies we calculate depend only on momenta and the fact that $Q^0_l = 0$ in our formalism barely changes the results. Furthermore, if the effect of interactions on the linear pockets would be such that it would make them larger than the threshold value in Fig. 5.5b, we would be able to detect it. In the language we proposed in the introduction, this would be a band-ferromagnetic state as the bands filled up to different energies, but have no net magnetization.

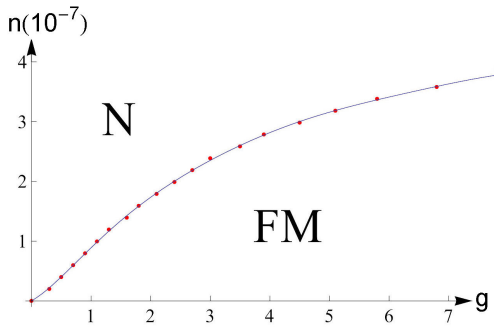

Figure 5.6: Phase diagram, doping (n) versus interaction strength (g). The doping is dimensionless but can be converted to experimental units (cm^{-2}) through multiplication with Λ^2. There is a first-order phase transition from the ferromagnetic state (FM) to the normal state (N) as doping is increased.

In the doped case, the reference state with respect to which we compute energy differences has nonzero kinetic and exchange energies, $E^0_{\mathrm{kin}} = E_{\mathrm{kin}}(Q^0_l, Q^0_p)$ and $E^0_{\mathrm{ex}} = 2E_{\mathrm{ex}}(Q^0_l, Q^0_p)$. One is now ready to vary the pocket parameters, compute the energies, apply the constraint (5.19), and find the configuration that minimizes the energy

$$\begin{aligned} \Delta E = {} & E_{\mathrm{kin}}(Q_{lu}, Q_{pu}) + E_{\mathrm{kin}}(Q_{ld}, Q_{pd}) - E^0_{\mathrm{kin}} \\ & + E_{\mathrm{ex}}(Q_{lu}, Q_{pu}) + E_{\mathrm{ex}}(Q_{ld}, Q_{pd}) - E^0_{\mathrm{ex}}. \end{aligned}$$

The result will depend on the value of the interaction parameter g. If the graphene trilayer is doped, the system can still relax into a ferromagnetic state, but a critical

interaction strength is needed. This critical value of the interaction increases with doping, as it can be seen in Fig. 5.6. The linear bands stay empty (up to our resolution) and the parabolic pockets exhibit a discontinuous jump, indicating a first-order phase transition. This state is both band ferromagnetic, as well as spin ferromagnetic. Note that the jump is such that in one of the parabolic bands hole pockets will occur.

So far we have looked only at configurations in which the pocket sizes are small. Although for the doped case the phase transition is first order, the pocket sizes are small and it is known that in monolayer graphene another first order transition occurs as the interaction strength exceeds some critical value ($g_c \approx 5.3$ for undoped monolayer graphene) [153]. This transition is to a phase in which the monolayer has maximal magnetization. Since, for some purposes, one can regard a trilayer as a combination of monolayer and bilayer graphene, it is natural to look for this transition in a graphene trilayer. Although this transition is theoretically present, we conclude that it can not been seen in any realistic experiment, because the critical coupling is out of any experimental range ($g_c > 200$).

5.4 Conclusions

In this Chapter, we have determined the ground state of trilayer graphene accounting for the long range Coulomb interaction. We used a formalism in which we could treat electronlike and holelike pockets on the same footing. This allowed us to vary the four pocket parameters (linear or parabolic and spin up or down) to obtain a large dataset. We have chosen the discrete points to lie on a square-root profile, so that we had many points that satisfied the constraint (5.16) for the undoped system or (5.19) for the doped one.

For the undoped trilayer, we found that the energy is minimized for a configuration in which the linear bands are empty and an electron and a hole pocket occur in the spin-up and spin-down parabolic bands, which is a spin-ferromagnetic state (Fig. 5.2a). Since there is no preferred direction for the spin, this state is doubly degenerate (Fig. 5.4a). The pockets increase in size when the interaction is tuned to higher values. They are only zero when the interaction vanishes, see Fig. 5.5a.

The doped trilayer is more subtle, since the noninteracting case is already a band-ferromagnetic state in which the bands (linear and parabolic) fill up differently (Fig. 5.2b). We named it a "band-ferromagnetic" state due to the finite polarization in the subband-index degree of freedom associated with parabolic and linear bands. Although in physical systems the bands will shift with respect to each other, resulting in a well-defined Fermi energy, we chose to keep the bands fixed and let the bands fill up differently. This gave us two Fermi momenta ($k_F^{l/p}$)

and Fermi energies ($E_F^{l/p}$). Although $E_F^p < E_F^l$, the parabolic band is much flatter than the linear one and therefore $k_F^p >> k_F^l$. Our resolution was such that $k_F^l = 0$, but this simplification will not affect the results. If the linear pockets exceed the threshold value given by the blue line in Fig. 5.5b for some value of the interaction strength we would have detected this. It turned out, however, that the linear bands stay empty for all doping levels that we considered. Furthermore, we saw a transition to a spin-ferromagnetic state. In contrast with the undoped case, this state is the ground state only if the coupling exceeds some critical value, which on its turn increases with doping. The doping versus interaction strength phase diagram is shown in Fig. 5.6. The phase transition from the normal state (N) to a magnetic state (FM) is first order, i.e. the pocket size jumps discontinuously and the magnetization also exhibits a jump to some nonzero value. Note that this magnetic state is both spin-ferromagnetic and band-ferromagnetic, since the bands fill up to different energies (Fig. 5.2c).

We have also looked for a phase transition to a maximally magnetized state, as observed in monolayer graphene. We do not find such a transition for any interaction strength that would be experimentally achievable.

Although the graphene trilayer exhibits some features of both monolayer and bilayer graphene, it is an interesting system on itself and more complex than either of the two. The interplay between the filling of the linear and parabolic bands gives rise to many more possible configurations of the pocket parameters. For example, already in the noninteracting groundstate of the doped trilayer the bands are shifted with respect to each other.

It would be interesting to measure this spectrum in experiments using, for example, angle resolved photo-emission spectroscopy (ARPES). Long-range Coulomb interactions can give rise to a ferromagnetic groundstate as it does in bilayer graphene, but will not affect the linear bands. The first-order transition as seen in monolayer graphene is not present as a result of interactions between the different bands.

We are aware that next-nearest-neighbor hopping parameters have effects on the energy spectrum that are of comparable magnitude as the effect we describe here [66]. However, if the system is sufficiently doped this will not alter our results. For the undoped case the results may be slightly altered, but our results could definitely be used as a starting point to investigate the full parameter model in more detail.

Acknowledgements

The authors acknowledge financial support from the Netherlands Organization for Scientific Research (NWO).

Chapter 6

Ferromagnetism in ABC-stacked trilayer graphene

Abstract

In this Chapter we study the ferromagnetic behavior of ABC-stacked trilayer graphene. This is done using a nearest-neighbor tight-binding model, in the presence of long-range Coulomb interactions. For a given electron-electron interaction g and doping level n, we determine whether the total energy is minimized for a paramagnetic or ferromagnetic configuration of our variational parameters. The g versus n phase diagram is first calculated for the unscreened case. We then include the effects of screening using a simplified expression for the fermion bubble diagram. We show that ferromagnetism in ABC-stacked trilayer graphene is more robust than in monolayer, in bilayer, and in ABA-stacked trilayer graphene. Although the screening reduces the ferromagnetic regime in ABC-stacked trilayer graphene, the critical doping level remains one order of magnitude larger than in unscreened bilayer graphene.[1]

6.1 Introduction

Within a decade after the discovery of graphene flakes by mechanical exfoliation [1], numerous methods have been developed to create larger and cleaner samples, realized both as single layers and as stacked layers of graphene [43, 156, 31, 157, 158, 44].

Early on, it was realized that stacked graphene layers behave differently than both a single layer and 3D graphite. For example, in bilayer graphene the dispersion is quadratic instead of linear and the electrons behave as massive chiral particles, which is a completely new type of particle. Few-layer graphene is still

[1]This Chapter is based on *Ferromagnetism in ABC-stacked trilayer graphene*, R. Olsen, R. van Gelderen, and C. Morais Smith, Phys. Rev. B, **87**, 115414 (2013).

a 2D system, hence the quantum Hall effect can be observed. For monolayer graphene, the plateaus in the Hall conductivity are located at half integer multiples of $4e^2/h$ [26], originating from a Landau level at zero energy which is half filled by electrons and half filled by holes. In bilayer graphene, this particular Landau level has an extra degeneracy resulting in Hall plateaus at integer values of $4e^2/h$ and a quantum Hall effect that is different from the one in a monolayer as well as from the quantum Hall effect found in usual two-dimensional electron gases [57]. In addition to the number of layers, the order of the stacking also influences the physical properties significantly.

In multilayer graphene, the different layers can have three distinct orientations with respect to the bottom one. Bernal stacking (or AB stacking) is the configuration in which the $\mathcal{B}$ sublattice of the odd layers are opposite to the $\mathcal{A}$ sublattice of the even layers. The Hamiltonian of a system with an even number $2N$ of layers can be rewritten in a block diagonal form, where the N different blocks are bilayerlike Hamiltonians. The blocks can be linked by hopping parameters that couple lattice sites on next-nearest planes. For an odd number $(2N+1)$ of layers, one of the blocks is the monolayer Hamiltonian. Therefore, these systems have a linear band in addition to the N parabolic ones [138].

In ABC-stacked multilayer graphene, the $\mathcal{B}$ sublattice of each layer lies opposite to the $\mathcal{A}$ sublattice of the layer above it, but opposite to the honeycomb centers in the layer beneath it (see Fig. 6.1). Since electrons that are placed oppositely in two bordering planes dimerize, resulting in an energy shift away from zero, these multilayers can, for low energies, be described by a 2×2 effective matrix Hamiltonian, which is governed by the indirect (effective) hopping between the two atoms in the outer planes that have no neighbor in the adjacent layer. This effective hopping is a process consisting of $N-1$ interplane nearest-neighbor hoppings, combined with N in-plane nearest-neighbor hoppings, resulting in an energy dispersion around the K points, $E_N \sim v_F^N k^N / t_\perp^{(N-1)}$ [139].

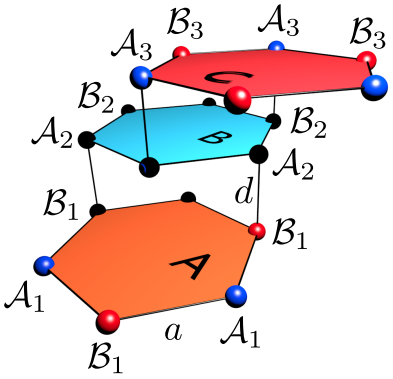

Figure 6.1: Atomic structure of ABC-stacked trilayer graphene.

A tight-binding approach for an increasing number of layers should in principle include hopping between more distant carbon atoms. The long known Slonczewski-Weiss-McClure (SWMc) model [64, 63] accounts for next-nearest-neighbor hopping, as well as hopping between next-nearest planes. In fact, trilayer graphene can be used to obtain the values of the different hopping parameters by fitting

experimental data to the SWMc model [99]. However, often it is sufficient to take into account only the intra- and interplane nearest-neighbor hopping parameters.

Recent experimental and theoretical studies of trilayer graphene have shown that magnetotransport and electronic transport properties [159], thermoelectric transport properties [160], and chiral tunneling [161] indeed depend on the stacking order. Furthermore, one can open a sizeable band gap in ABC-stacked trilayers (120 meV) by applying an external electric field, while for an ABA-stacked trilayer no gap is observed under the same conditions [67]. Possible gapped many-body states have also been investigated [162].

Extensive research into the band structure of ABC-stacked multilayer graphene has been done recently using an effective mass approximation [61]. It was found that the electron and hole bands touching at zero energy support chiral quasiparticles characterized by a Berry phase of $N\pi$ for N layers. The phonon spectrum of ABC-stacked graphene has been investigated theoretically using density functional theory [163] and experimentally by using infrared absorption spectroscopy, where the intensities have been found to be much stronger than that of bilayer graphene [164]. Using magnetic fields up to 60T, there has been evidence of the integer quantum Hall effect in trilayer graphene [152]. The Hall resistivity plateaus have been reproduced by using a self-consistent Hartree calculation on ABC-stacked graphene [152]. It has been suggested that the differences in the quantum Hall effect between ABC and ABA-stacking might be used to identify the stacking order of high-quality trilayer samples [165]. By using infrared absorption spectroscopy, it has been shown that the optical conductivity spectra for ABC and ABA-stacked graphene differs considerably [166]. These optical properties have been calculated and reproduced in the framework of a tight-binding model [167]. Finally, it can be mentioned that high-resolution transmission microscopy of ABC-stacked trilayer

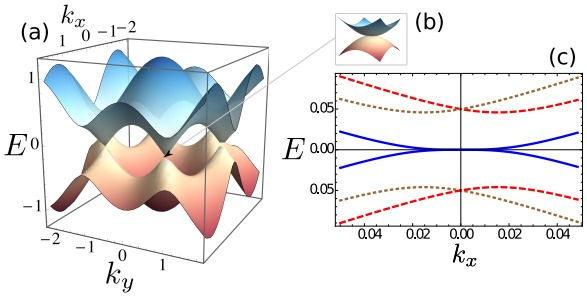

Figure 6.2: (a) Numerically calculated, full dispersion of ABC-stacked trilayer graphene (two lowest bands). (b) Zoom-in on one of the K points. (c) Numerically calculated low-energy approximation of ABC-stacked trilayer graphene dispersion (expansion around the K point).

graphene on a SiC surface has successfully provided information on the interlayer distances of ABC-stacked trilayer graphene [168].

In this Chapter we investigate the magnetic properties of ABC-stacked trilayer graphene by using a nearest-neighbor tight-binding model, in the presence of long-range Coulomb interactions. For interacting electrons, the system can gain energy by aligning the spins of the electrons. This *exchange mechanism* is accompanied by a cost in kinetic energy due to the Pauli principle. After fixing the doping level and interaction strength, one can use a variational approach to determine whether the system spontaneously magnetizes or remains paramagnetic. For monolayer graphene, the system only magnetizes if the interaction strength is tuned to unphysically high values. Depending on the doping level n, this phase transition can be first or second order [153]. For bilayer graphene the system can be ferromagnetic for the estimated value of the Coulomb interaction ($g = 2.1$), but the electron density has to be as low as $n \sim 10^9$ cm^{-2} for the material to become magnetic [154]. This is on the brink of what is experimentally achievable, since it is not possible to create perfectly undoped graphene in experiment, due to the formation of electron hole puddles [27] and impurities trapped in the substrate. In ABA-stacked trilayer, the interplay between the linear and the parabolic bands opens up possibilities for both spin- and band-ferromagnetism, but only at low electron doping [85].

Although in a low-energy approximation ABC-stacked trilayer graphene seems to be, in a way, the three layer generalization of the Bernal stacked bilayer [139], it is worth a further investigation because its cubic energy dispersion is expected to enhance significantly the phase space where the ferromagnetic regime occurs. In addition, screening should play an important role, due to the diverging density of states. Here we show that this is indeed the case: although the screening reduces the regime of parameters for the occurrence of ferromagnetism, the latter remains at least one order of magnitude more robust than in unscreened bilayer graphene. The outline of this Chapter is the following: we set up the model in Sec. 6.2, present our results of the unscreened case in Sec. 6.3, and look at the effects of screening in Sec. 6.4. Our conclusions are drawn in Sec. 6.5.

6.2 The model

We use a tight-binding model which takes into account the hopping of electrons to nearest-neighbor in-plane and interplane sites. In real space, the Hamiltonian is given by

$$H = H_0 + H_I, \tag{6.1}$$

with the non-interacting part being

$$
\begin{aligned}
H_0 = &-t \sum_{\langle i,j\rangle,\sigma} \sum_{n=1}^{3} \left[a^{\dagger}_{i,\sigma,n} b_{j,\sigma,n} + \text{H.c.} \right] \\
&- t_{\perp} \sum_{i,\sigma} \left[b^{\dagger}_{i,\sigma,1} a_{i,\sigma,2} + \text{H.c.} \right] \\
&- t_{\perp} \sum_{i,\sigma} \left[b^{\dagger}_{i,\sigma,2} a_{i,\sigma,3} + \text{H.c.} \right],
\end{aligned}
\tag{6.2}
$$

where i and j label the lattice sites, $\sigma \in \{\uparrow, \downarrow\}$ labels spin, $n \in \{1, 2, 3\}$ labels the layer, $t \approx 3$ eV denotes the intralayer nearest-neighbor hopping parameter, $t_{\perp} \approx 0.35$ eV denotes the interlayer nearest-neighbor hopping, and the operator $c^{\dagger}$ (c) creates (annihilates) an electron on sublattice $\mathcal{C} \in \{\mathcal{A}, \mathcal{B}\}$. H_I is the interaction Hamiltonian. Since the stacking considered is ABC, the $\mathcal{A}$ sublattice in the bottom layer (layer 1) and the $\mathcal{B}$ sublattice in the top layer (layer 3) do not have direct neighbors in an adjacent layer. The electrons interact via a Coulomb interaction, which can be included in our model by the term

$$
\begin{aligned}
H_I = \frac{1}{2} \int d^2\mathbf{x}\, d^2\mathbf{y} \big\{ & V^{\mathrm{D}}(\mathbf{x}-\mathbf{y}) [\rho_1(\mathbf{x})\rho_1(\mathbf{y}) + \rho_2(\mathbf{x})\rho_2(\mathbf{y}) \\
&+ \rho_3(\mathbf{x})\rho_3(\mathbf{y})] + V^{\mathrm{ND}}(\mathbf{x}-\mathbf{y}) [\rho_1(\mathbf{x})\rho_2(\mathbf{y}) \\
&+ \rho_2(\mathbf{x})\rho_1(\mathbf{y}) + \rho_2(\mathbf{x})\rho_3(\mathbf{y}) + \rho_3(\mathbf{x})\rho_2(\mathbf{y})] \\
&+ V^{\mathrm{2ND}}(\mathbf{x}-\mathbf{y}) [\rho_1(\mathbf{x})\rho_3(\mathbf{y}) + \rho_3(\mathbf{x})\rho_1(\mathbf{y})] \big\},
\end{aligned}
\tag{6.3}
$$

where the density of electrons in the nth layer is given by $\rho_n(\mathbf{x}) = \sum_{\sigma} \Psi^{\dagger}_{\sigma,n}(\mathbf{x}) \Psi_{\sigma,n}(\mathbf{x})$, with $\Psi_{\sigma,n}(\mathbf{x}) \equiv (a_{\sigma,n}(\mathbf{x}), b_{\sigma,n}(\mathbf{x}))$, where $a_{\sigma,n}(\mathbf{x})$ and $b_{\sigma,n}(\mathbf{x})$ are the field operators corresponding to $a_{i,\sigma,n}$ and $b_{i,\sigma,n}$, respectively. The interaction potentials for the in-plane (D), the nearest-neighbor planes (ND) and

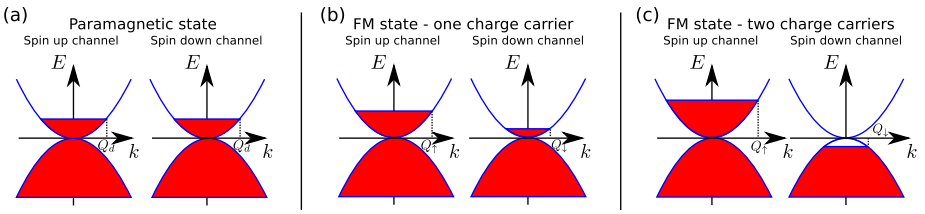

Figure 6.3: Sketch of the electron (hole) pockets for three configurations of the system: (a) paramagnetic, (b) ferromagnetic with one type of charge carrier, and (c) ferromagnetic with two types of carriers.

the next-nearest-neighbor planes (2ND) are given by

$$V^{\mathrm{D}}(\mathbf{x}-\mathbf{y}) = \frac{2\pi e^2}{\epsilon|\mathbf{x}-\mathbf{y}|},$$
$$V^{\mathrm{ND}}(\mathbf{x}-\mathbf{y}) = \frac{2\pi e^2}{\epsilon\sqrt{d^2+|\mathbf{x}-\mathbf{y}|^2}},$$
$$V^{\mathrm{2ND}}(\mathbf{x}-\mathbf{y}) = \frac{2\pi e^2}{\epsilon\sqrt{4d^2+|\mathbf{x}-\mathbf{y}|^2}}.$$

In these interaction potentials, $d \approx 3.2$ Å is the interlayer distance, e the electron charge, and ϵ the average dielectric constant of the substrate and the material above graphene ($\epsilon = 1$ for suspended graphene in vacuum).

6.2.1 Kinetic energy

After Fourier transforming and expanding the momenta around the K point, the noninteracting Hamiltonian acquires the form

$$H_0 = \sum_\sigma \int d\mathbf{k}\Psi^\dagger_\sigma(\mathbf{k})\mathcal{H}(\mathbf{k})\Psi_\sigma(\mathbf{k}), \tag{6.4}$$
$$\Psi^\dagger_\sigma(\mathbf{k}) = (a^\dagger_{\mathbf{k},\sigma,1}, b^\dagger_{\mathbf{k},\sigma,1}, a^\dagger_{\mathbf{k},\sigma,2}, b^\dagger_{\mathbf{k},\sigma,2}, a^\dagger_{\mathbf{k},\sigma,3}, b^\dagger_{\mathbf{k},\sigma,3}),$$

where $c^\dagger_{\mathbf{k},\sigma,n}$ creates a particle with momentum $\mathbf{k}$ on sublattice $c \in \{a, b\}$ in layer n with spin σ, and $\mathcal{H}$ is a 6×6 matrix given by

$$\mathcal{H} = \hbar v_F \begin{pmatrix} 0 & u & 0 & 0 & 0 & 0 \\ u^* & 0 & -\gamma_1 & 0 & 0 & 0 \\ 0 & -\gamma_1 & 0 & u & 0 & 0 \\ 0 & 0 & u^* & 0 & -\gamma_1 & 0 \\ 0 & 0 & 0 & -\gamma_1 & 0 & u \\ 0 & 0 & 0 & 0 & u^* & 0 \end{pmatrix}, \tag{6.5}$$

where $u \equiv ke^{i\phi(\mathbf{k})}$. In the above expression, $k = |\mathbf{k}|$ is the norm of the two-dimensional momentum vector, $\phi(\mathbf{k}) = \arctan(k_y/k_x)$ is the angle of the momentum vector, $\hbar v_F = (3/2)at$ is the Fermi velocity in terms of the lattice constant $a = 1.42$ Å and intralayer hopping parameter t, and $\gamma_1 \equiv t_\perp/(\hbar v_F)$.

Although it is possible to write an analytic expression for the low-energy approximation of the single-particle dispersion for ABC-stacked trilayer graphene [169], this is not the case for the required diagonalization matrix for $\mathcal{H}$. For this reason, we calculate both numerically. The full dispersion is shown in Fig. 6.2(a) and (b), together with an expansion of the energy bands around the K point (i.e. eigenvalues of Eq. (6.5)), which are indeed cubic for small momenta (at small momenta $E(k) \approx \pm(v_F^3/t_\perp^2)k^3$ for the two lowest bands), see Fig. 6.2(c).

When the system undergoes a phase transition into a ferromagnetic state, pockets of one spin configuration – let us say up – will be larger than the pocket of spin-down electrons [see Fig. 6.3(a)-(b)] Moreover, it is also possible to have two types of charge carriers in the system, i.e. the formation of spin-up electron-pockets and spin-down hole pockets [see Fig. 6.3(c)].

To compute the energy of an electron or hole pocket of size Q_σ (see Fig. 6.3), we have to compute the integral

$$\Delta K = \int_0^{E(Q_\sigma)} E\mathcal{D}(E)dE,$$

where $\mathcal{D}(E)$ is the density of states

$$\mathcal{D}(E) = \frac{\partial N}{\partial E} = \frac{A}{4\pi}\frac{\partial}{\partial E}\left[k(E)^2\right],$$

with A denoting the area of the unit cell and N is the number of states below E. We compute the inverse of the dispersion relation $E(k)$ numerically. Note that for small pocket sizes, $\Delta K \sim Q_\sigma^5$. When compared with monolayer graphene ($\Delta K^{m.l.} \sim Q_\sigma^3$) [153] and bilayer graphene ($\Delta K^{b.l.} \sim Q_\sigma^4$) [154] it is evident that the kinetic energy cost of an electron (hole) pocket is smaller in ABC-stacked trilayer graphene than in the fewer-layered carbon structures.

6.2.2 Exchange energy

When calculating the energy contribution coming from H_I, the direct contribution (i.e. the Hartree term) cancels due to the positive Jellium background. The only term left is the exchange contribution (i.e., the Fock term), which favors spin alignment. However, spin alignment will result in a cost in kinetic energy due to the Pauli exclusion principle. Thus, ferromagnetism will occur or not, depending on the competition between the kinetic energy and the exchange energy.

In the appendix of this Chapter (section 6.A), it is shown that the exchange energy of a configuration as in Fig. 6.3, where the spin-up and the spin-down bands fill up differently, can be written in a way similar to the one in bilayer graphene [154],

$$\frac{E_{\text{ex}}}{A} = -\frac{1}{2}\int \frac{d\,\mathbf{k}}{(2\pi)^2}\frac{d\,\mathbf{k}'}{(2\pi)^2}\sum_{\sigma,a}\sum_{s=1}^{6}\sum_{\alpha,\beta=1}^{6} \left[\chi^s_{\alpha\beta}(\mathbf{k}',\mathbf{k})\chi^s_{\beta\alpha}(\mathbf{k},\mathbf{k}')V_s(\mathbf{k}'-\mathbf{k})n_{\sigma,\alpha,a}(\mathbf{k}')n_{\sigma,\beta,a}(\mathbf{k})\right]. \tag{6.6}$$

Here, α and β label the band index and a labels the valley, but we will neglect intervalley scattering and only focus on the K point. $n_{\sigma,\alpha,a}(\mathbf{k})$ are the Fermi

functions and the expressions for $V_s(\mathbf{k}' - \mathbf{k})$ are given in the appendix (section 6.A). In comparison with the bilayer, there are six χ matrices instead of two and they are no longer 4×4, but 6×6. Moreover, they can only be computed numerically (see the appendix of this Chapter for more details).

Since we have expanded around the K point, we introduce a cutoff $\Lambda = \sqrt{2\pi/A}$ in such a way that the number of states in the Brillouin zone is conserved. Using the cutoff, we can measure momenta (and hence pocket sizes) in units of Λ and energies in units of $\hbar v_F \Lambda (\approx 7.2$ eV). This makes all our variables and parameters dimensionless and after setting $\hbar = 1$, $v_F = 1$, and $\Lambda = 1$ they have the following values: $t = 0.42$, $t_\perp = 0.05$, $a = 1.56$, and $d = 3.7$ [170].

6.3 Unscreened case

6.3.1 Numerical solution

The exchange energy E_{ex}/A given by Eq. (6.6) is solved numerically using the double exponential (DE) algorithm [171] (the DE algorithm is originally intended for 1D integrals, but is extended to 3D to perform the exchange integrals). Due to the singular behavior of the Coulomb potentials, the integral must undergo a series of transformations. Firstly, the integral is transformed to polar coordinates, where we introduce a cutoff Λ for integrals over the norm of the the momentum. A change of variables is then applied, such that these integrations range from zero to one. This permits the singular behavior along $\mathbf{k} = \mathbf{k}'$ to be rotated by a Duffy coordinate transformation [172]

$$\begin{aligned}\int_0^{2\pi} d\theta \int_0^1 dk \int_0^1 dk' \frac{F(k,k',\theta)}{\sqrt{(k'^2 - 2kk'Q\cos\theta + Q^2k^2}} \\ = \int_0^{2\pi} d\theta \int_0^1 dk \int_0^1 dk'' \Bigg[\frac{F(k,kk'',\theta)}{\sqrt{k''^2 - 2k''Q\cos\theta + Q^2}} \\ + \frac{F(kk'',k,\theta)}{\sqrt{1 - 2k''Q\cos\theta + Q^2k''^2}} \Bigg]. \end{aligned} \tag{6.7}$$

This formula is derived by splitting the k' integration into two separate integrations from 0 to k and from k to 1. Making the change of variables $k' = kk''$ on the first integral leads to the first term on the right hand side of Eq. (6.7). In the second integral, with integration boundaries k and 1, the identity $\int_0^1 dk \int_k^1 dk' f(k,k') = \int_0^1 dk \int_0^k dk' f(k',k)$ is applied. Thus, a change of variables $k' = kk''$ leads to the second term on the right hand side of Eq. (6.7).

The singularities are now confined to lines parallel to the k-axis. However, there are now two such lines of singularities in the integrand, located at $k'' = h_1 \neq 1$ and $k'' = h_2 \neq 1$. The lines of singularities located at h_1 and h_2 must be moved

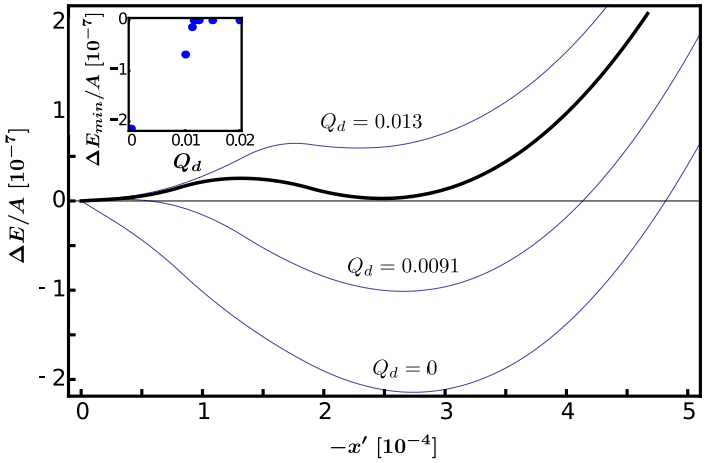

Figure 6.4: ΔE versus $-x'$ at electron-electron coupling $g = 6$. The phase transition occurs at the doping $Q_d \approx 0.0116$ that produces the thick black curve. Inset: Minimum energy versus doping Q_d. The phase transition is identified by the value of Q_d where ΔE_{min} first becomes nonzero.

to $k'' = 1$ by a change of variables. After the change of variables, the integration boundaries are no longer confined to zero and one. Since the DE algorithm is only capable of handling singularities at the integration boundaries, all integrals are split at $k'' = 1$ (where the singularities are now located), before being performed.

The Hamiltonian matrix $\mathcal{H}$ of Eq. (6.5) is diagonalized numerically using the Jacobi diagonalization algorithm, which is extended to handle a Hermitian 6×6 matrix by solving the corresponding 12×12 real symmetric matrix [173]. The resulting diagonalization matrix $\mathcal{M}(\mathbf{k})$ is used inside the χ matrices of Eq. (6.6) to calculate the exchange energy, while the resulting dispersion $E(k)$ is used to calculate the kinetic energy (see Appendix for details).

The numerical diagonalization process does not provide $E^{-1}(k)$, which is needed to calculate the kinetic energy. Thus, the inverse is approximated by linear interpolation of the dispersion. Integration by parts yields

$$\Delta K = E(Q)N(E(Q)) - \int_0^{E(Q)} N(E)dE,$$

which is used in order to avoid explicit numerical evaluation of $\partial N/\partial E$.

Consider a paramagnetic state with doping Q_d and a ferromagnetic state with electron (or hole) pockets $Q_\uparrow$ and $Q_\downarrow$. Then, the kinetic energy difference is calculated by

$$\frac{\Delta E_{kin}}{A} = \frac{1}{A}\left[\Delta K(Q_\uparrow) + \Delta K(Q_\downarrow) - 2\Delta K(Q_d)\right].$$

The difference in exchange energy $\Delta E_{ex}/A$ is calculated by subtracting E_{ex}/A of the paramagnetic state from the corresponding energy of the ferromagnetic state. For an unperturbed system, both spin channels are filled up to the Fermi-momentum Q_d [see Fig. 6.3(a)]. Due to the exchange mechanism, the system can prefer a ferromagnetic state with either one type of carrier or two types of carriers [see Fig. 6.3(b)-(c)]. These perturbations are parameterized by the variable x, which is positive for one type of carrier and given by

$$Q_\uparrow^2 = 2Q_d^2 - x, \qquad Q_\downarrow^2 = x.$$

For two types of carriers, x is defined to be negative and parameterizes the electron and hole pocket as

$$Q_\uparrow^2 = 2Q_d^2 + |x|, \qquad Q_\downarrow^2 = |x|,$$

where we assume the electron pocket in the spin-up channel. Using this parametrization, particle conservation is satisfied. It is convenient to introduce $x' \equiv x - Q_d^2$, such that $x' = 0$ represents the unperturbed state (i.e. $Q_\uparrow = Q_\downarrow = Q_d$). Then, $\Delta E/A = \Delta E_{kin}/A + \Delta E_{ex}/A$ can be plotted as a function of x' for given electron-electron coupling g and doping Q_d (see Fig. 6.4).
The minimum of $\Delta E(x)/A$ is estimated numerically by interpolation of points close to the minimum. The critical doping, where the minimum $\Delta E_{min}/A$ of $\Delta E(x)/A$ is zero, is found numerically by solving $\Delta E_{min}(Q_d)/A = 0$. Since each minimum is a time consuming calculation, a simple binary search pattern is used (see inset of Fig. 6.4).

6.3.2 Phase diagram

For a fixed value of $g = 6$, we see in Fig. 6.4 the behavior of ΔE as a function of pocket sizes, upon varying the doping Q_d. For some doping values, ΔE is positive definite (paramagnetic phase), while for others ΔE attains a negative minimum (ferromagnetic phase). Inspection of the critical curve (thick line) shows that there is a first order phase transition between the paramagnetic and ferromagnetic

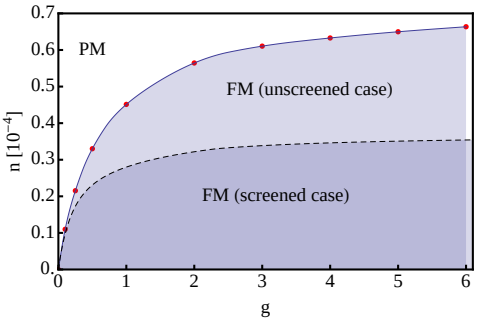

Figure 6.5: Phase diagram for ABC-stacked trilayer graphene, in the case of an unscreened potential (solid blue line) and a screened potential (dashed black line). The red dots are the calculated values, while the solid line is an interpolation function based on the calculated points.

phases. Repeating the entire procedure for different values of g leads to the g versus n phase diagram depicted in Fig. 6.5, where $n = Q_d^2/2$. The continuous solid line is an interpolation function of the calculated points.

These results were obtained by neglecting higher order corrections that lead to screening of the Coulomb potential. These effects will be considered in the next section.

6.4 Effects of screening

6.4.1 Screened potential

Fourier transforming the real-space potentials V^D, V^{ND} and V^{2ND} and going to dimensionless variables yields

$$V^D = \frac{2\pi g}{k}, \quad V^{ND} = \frac{2\pi g e^{-kd}}{k}, \quad V^{2ND} = \frac{2\pi g e^{-2kd}}{k},$$

where $g = e^2/\epsilon\hbar v_F$. As can be seen from Eq. (6.11) in the Appendix, the bare interaction line of ABC-stacked trilayer graphene becomes a matrix V_{mn}, where m and n are layer indices. Therefore, the RPA renormalization of the potential [174] can be described by the Dyson-like equation

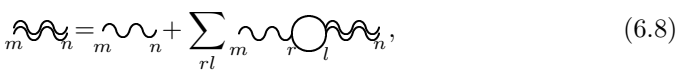

(6.8)

where r and l are layer indices. Let $\mathcal{V}_{mn}$ be the renormalized potential. Then,

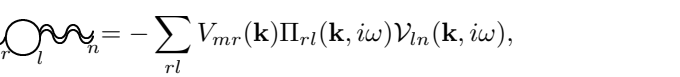

where

$$\Pi_{rl}(\mathbf{k}, i\omega) := \sum_{\sigma} \int \frac{d\mathbf{k}'}{(2\pi)^2} \int \frac{d\omega'}{\beta} G_0^{\sigma,rl}(\mathbf{k}', i\omega') \times G_0^{\sigma,lr}(\mathbf{k}' - \mathbf{k}, i\omega' - i\omega)$$

and $G_0^{\sigma,lr}$ is the noninteracting Green's function of the system. Eq. (6.8) is difficult to solve due to the layer dependence. However, for sufficiently low momenta $e^{-kd} \sim 1$ and $e^{-2kd} \sim 1$, which means that $V_{ij} \sim V \equiv 2\pi g/k$. Thus, the layer dependence is removed, and Eq. (6.8) can be solved with respect to $\mathcal{V}_{ij} \equiv \mathcal{V}$:

$$\mathcal{V}(\mathbf{k}) = \frac{V(k)}{1 - V(k) \sum_{rl} \Pi_{rl}(\mathbf{k}, i\omega)}. \tag{6.9}$$

This equation holds for suspended trilayer graphene in vacuum. If the trilayer is deposited on a substrate, the results remain valid as long as the substrate is

insulating. Indeed, the only effect of the insulating substrate on the potential is an increase of the dielectric constant compared to the suspended sample, hence a lowering of the interaction parameter g [155]. On the other hand, when the trilayer is placed on a metallic substrate, the electrons of the substrate also contribute to the screening of the Coulomb potential in the graphene system. This effect could be incorporated into the theory by extending the summation in Eq. (6.8) to include also these electrons. However, in order to calculate the polarization in this case, one would need to include their energy dispersion and the end result would heavily depend on the substrate used. Since this behavior is not universal, such a study is beyond the scope of this thesis.

6.4.2 Phase diagram

It is interesting to observe that Eq. (6.9) does not converge to the true unscreened potential V_{mn} as $\Pi_{rl} \to 0$. In order to achieve such a convergence, Eq. (6.9) must be changed to

$$\mathcal{V}_{mn}(\mathbf{k}, i\omega) = \frac{V_{mn}(k)}{1 - V(k)\Pi^{tot}(\mathbf{k}, i\omega)},$$

where

$$\begin{aligned}\Pi^{tot}(\mathbf{k}, i\omega) &\equiv \sum_{\sigma} \Pi(Q_\sigma, \mathbf{k}, i\omega) \\ &\equiv \sum_{rl,\sigma} \Pi_{rl}(Q_\sigma, \mathbf{k}, i\omega).\end{aligned}$$

Since the polarization depends on ω, the renormalized potential $\mathcal{V}$ also does. This frequency dependence of the potential becomes important when plasmon excitations are present. Here we study the zero-temperature limit, hence plasmons cannot be thermally excited. Since no external fields are considered either, we can take the $\omega \to 0$ limit (i.e the static limit). For both, monolayer and bilayer graphene, the polarization $\Pi(Q_\sigma, \mathbf{k}, 0)$ behaves linearly in k for large k, independent of Fermi momentum Q_σ, and exhibits an identical slope [87]. This occurs because the dispersions are linear in the large-k limit for both systems, and the Green's functions depend on the dispersion. Since the dispersion of ABC-stacked trilayer graphene is also linear in the large-k limit with the same slope as of the single- and bilayer dispersions, it is reasonable to assume that the linear behavior of $\Pi(Q_\sigma, \mathbf{k}, 0)$ is also present for ABC-stacked trilayer graphene. In the exchange energy integrations, there are terms that are integrated from zero to the edge of the Brillouin zone (i.e. the cutoff $\Lambda = 1$). Therefore, we will first focus on the screening effects coming from the linear behavior of $\Pi(Q_\sigma, \mathbf{k}, 0)$ and approximate it by $\Pi(Q_\sigma, \mathbf{k}, 0) = \kappa k$. An analytical expression of $\Pi(Q_\sigma, \mathbf{k}, 0)$ was calculated by Gamayun [87] for bilayer graphene and is plotted in Fig. 6.6 for two values

of the Fermi momentum (dashed and dotted lines) and compared with the linear estimate, where $\kappa \approx -0.12495$ (solid line) [175]. Notice that the high-k approximation that we use here is better than the one obtained using a two-band low-k approximation. Indeed, for bilayer graphene where both the two-band and the full-band polarizations were calculated, we see that the low-k approximation of the two-band model misses the correct high-k linear asymptotics and introduces a large error in the integrals which are performed up to the cutoff Λ.

Let us now use the linear expression for Π and define $V \equiv g\tilde{V}$. Then, since $\Pi^{tot}V = 2\Pi V$ is constant in k, the renormalized potential can be written as $\mathcal{V}_{ij} = \tilde{g}\tilde{V}_{ij}$, where

$$\tilde{g} \equiv \frac{g}{1 - 4\pi g\kappa}.$$

Thus, the large momentum behavior of the renormalized potential effectively renormalizes the electron-electron coupling g. Let $n(g)$ be an interpolation function representing the phase boundary in the case of no screening (the solid line in Fig. 6.5). Then,

$$n'(g) = n(\tilde{g}) = n\left(\frac{g}{1 - 4\pi g\kappa}\right),$$

is the phase boundary in the screened case. This boundary is shown by a dashed line in Fig. 6.5.

The low-k regime of the polarization $\Pi(Q_\sigma, \mathbf{k}, 0)$ for ABC-stacked trilayer graphene can be approximated by a constant $w = -1/[6\pi k_F \beta]$, where $\beta = 400$

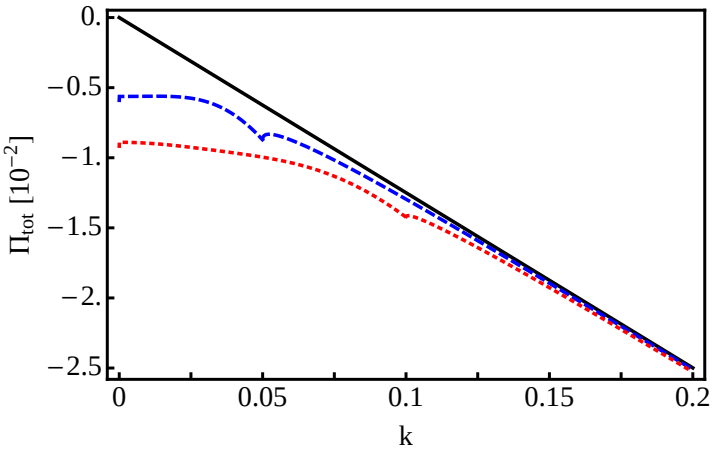

Figure 6.6: Plot of the bilayer graphene polarization $\Pi(k_F, \mathbf{k}, 0)$. The analytical expression derived in Ref. [87] is shown as a blue dashed line for $k_F = 0.025$ and as a red dotted line for $k_F = 0.05$. The black solid line is the linear asymptote κk valid at large k, which we here extrapolate to small k.

[86]. We will consider the case where $g = 6$ and use the critical doping $k_F \approx 0.0116$ (see Fig. 6.4), which leads to $w \approx -0.0114$. It is natural to let the transition into the linear regime of Π occur at the point where $\kappa k_0 = w$, i.e. at $k_0 = 0.1$ for $g = 6$. The renormalized potential for $k < k_0$ now becomes

$$\mathcal{V}_{nm}(k) = \tilde{V}_{nm}(k)\frac{g}{1 - 4\pi g w/k} \equiv \tilde{V}_{nm}(k)\tilde{\tilde{g}}(k).$$

As a crude approximation, we can let

$$\begin{aligned}\mathcal{V}_{nm} &\approx \tilde{V}_{nm}\ \mathrm{avg}_{k\in\Omega}\left[\tilde{\tilde{g}}(k)\right] \\ &= \frac{\tilde{V}_{nm}}{\mathrm{vol}\ \Omega}\int_0^{k_0} dp \int_0^{k_0} dp' \int_0^{2\pi} d\theta \frac{g}{1 - 4\pi g w/k(p, p', \theta)},\end{aligned}$$

where $\Omega = [0, k_0]^2 \times [0, 2\pi]$ is the domain where the constant regime of the polarization holds and $k \equiv \sqrt{p^2 + p'^2 - 2pp'\cos\theta}$. Thus, the renormalized g for $g = 6$ at the critical k_F becomes

$$\tilde{\tilde{g}} = \ \mathrm{avg}_{k\in\Omega}\left[\tilde{\tilde{g}}(k)\right] \approx 0.46,$$

where the integration was calculated numerically. At the same values of g and k_F, the polarization in the linear regime yields $\tilde{g} \approx 0.58$. Thus, $\tilde{\tilde{g}} \sim \tilde{g}$, which implies that, as a first approximation, we may consider the linear approximation of the polarization for all momenta, which leads to the phase boundary represented by the black dashed line of Fig. 6.5.

6.5 Conclusions

In this Chapter we study the magnetic properties of ABC-stacked trilayer graphene using a tight-binding approach, where only the nearest-neighbor hopping parameters are taken into account. We include the Coulomb interaction and evaluate the exchange energy (Fock term) allowing for an unequal filling of the spin-up and spin-down bands. Then we calculate numerically the difference in energy between paramagnetic and ferromagnetic configurations of the system and identify the points of phase transitions for fixed values of the interaction parameter g. By repeating the calculations for several values of g, we obtain the phase diagram in the electron-electron coupling vs doping plane. As a first step, we did not take into account the effects of Coulomb screening. The results are shown as the solid line in Fig. 6.5.

Although the phase diagram for monolayer [153], bilayer [154], and ABA-stacked trilayer [85] graphene have been previously derived, effects of screening have been neglected until now. Our work represents the first step to incorporate these important effects.

For the unscreened case, at $g \approx 2.1$, a comparison with unscreened bilayer graphene [154] shows that ABC-stacked trilayer graphene has a ferromagnetic behavior which is approximately 50 times stronger. Furthermore, a similar comparison with ABA-stacked trilayer graphene [85] shows that ABC-stacked trilayer has a ferromagnetic behavior that is approximately 300 times stronger. At $g \approx 2.1$, monolayer graphene shows a paramagnetic behavior at all doping levels. In order for phase transitions to be present in monolayer graphene, the electron-electron coupling needs to exceed $g \approx 5$ [153]. Fig. 6.4 shows that at $g = 6$, the phase transition in ABC-stacked trilayer graphene is of first order. This behavior persists for all couplings $g < 6$. ABA-stacked trilayer [85] and bilayer graphene [154] also exhibits first order phase transitions for couplings $g < 6$. This is in contrast to monolayer graphene, where both first order and second order phase transitions take place at given couplings g [153]. Thus, ABC-stacked trilayer graphene behaves in a similar manner to bilayer and ABA-stacked trilayer graphene, but exhibits a much stronger ferromagnetic behavior, making it easier to experimentally detect ferromagnetism. At $g = 2.1$, the phase transition to ferromagnetism occurs at $n \approx 5.5 \cdot 10^{-5}$. In SI-units the doping level becomes $\tilde{n} = g_s g_v \Lambda^2 Q_d^2/[4\pi] = g_s g_v Q_d^2/[2A] = n g_s g_v/A$, where $g_s = 2$ and $g_v = 2$ are the spin and valley degeneracies, respectively, and $A \approx 5.2 \cdot 10^{-16}$ cm^2 is the area of the Brillouin zone. Thus, neglecting valley degeneracy, $\tilde{n} \approx 2 \cdot 10^{11}$ cm^{-2}. Note that, by mapping the parameter x' of Fig. 6.4 to x, we see that the critical curve attains a minimum at $x < 0$. Thus, in the ferromagnetic regime at $g = 6$, the energy is always minimized for a configuration with two types of charge carriers. This behavior persists for all $g < 6$.

These conclusions were reached by neglecting Coulomb screening. However, due to the diverging density of states in ABC-stacked trilayer graphene, screening plays a very important role and must be taken into account. A thorough calculation of the polarization bubble in the full-band model is beyond the scope of this Chapter. Nevertheless, we have included screening effects within a simplified model. In the case of monolayer and bilayer graphene, the large-k behavior of the bubble diagrams are linear in k, with the same slope κ. Arguing that this linear behavior also applies to ABC-stacked trilayer graphene, and approximating the low-k behavior of the polarization by a constant, we found that screening effects can be incorporated via a simple renormalization of the electron-electron coupling g. Fig. 6.5 shows that the large momentum behavior of the screening leads to a reduced ferromagnetic region in the ABC-stacked trilayer graphene phase diagram. However, ferromagnetism is still approximately 25 times stronger than in unscreened bilayer graphene, which means that ABC-stacked trilayer remains the material with the strongest ferromagnetic behavior.

We are aware that next-nearest-neighbor hopping parameters, like γ_3 of the SWMc model can be of the same order as γ_1 [98], and that this can have an in-

fluence on the low-momentum behavior of the model. This parameter has been systematically neglected in studies of ferromagnetism in multilayer graphene (see Ref. [154] for bilayer and Ref. [85] for ABA-stacked trilayer). The reason is that, for studying the effects of other hopping parameters, one needs to redefine what is meant by a particle and a hole pocket due to the broken rotational symmetry of the dispersion around the K point of the Brillouin zone, resulting from the SWMc model [98, 84]. Furthermore, this broken symmetry leads to more complex integration boundaries, which makes the resulting numerical integrations intractable.

Recently, an intrinsic bandgap of 6 meV was experimentally observed in suspended ABC-stacked trilayer graphene, and it was argued that it should be driven by interactions [150]. However, this gap did not appear in most of the samples placed on a substrate, which were investigated during the same study. Since suspended samples are more susceptible to ripples and deformations, it can well be that the spatial inversion symmetry was broken by strain, resulting in the intrinsic bandgap. Our studies should then apply for ABC-stacked trilayer graphene on a substrate, without deformations. Because the dielectric constant is larger for samples on a substrate than for suspended samples (in vacuum), the coupling constant g will be renormalized by a factor $\epsilon \sim 2.5$ for graphene on a SiO_2 wafer. Otherwise, the paramagnetic-ferromagnetic phase transition remains unaltered.

A simplified theoretical model which includes only on-site interactions suggests that the difference in bandstructure between ABA- and ABC-stacked trilayers should be enough to explain the presence of a gap due to antiferromagnetism in ABC-stacked samples, while ABA-stacked trilayers remain ungapped [177]. These studies, however, cannot explain why the gap arises only in suspended samples.

Here we include long-range Coulomb interactions and investigate also the effect of screening. It is usually argued (without further ado) that screening is more important in ABC-stacked trilayer than in the other related compunds. Our studies reveal that this is not always true, since the polarization is linearly increasing in a considerable region, over which one must integrate to obtain the exchange energy. This feature is similar in monolayer, bilayer, and ABC-stacked trilayer graphene, and it is simply a consequence of the linear dispersion at intermediate values of k, which occurs in all the cases. Our studies reveal that the low-energy approximation for the polarization is not always enough to ground fast conclusions. Although the final understanding about ABC-stacked trilayer graphene has not yet been reached, we hope that our work will pave the way to possible extensions of the existing models for the investigation of ferromagnetism in multi-layer graphene using numerical methods.

Acknowledgments

The authors acknowledge financial support from the Netherlands Organization for Scientific Research (NWO), as well as useful discussions with D. S. L. Abergel, D. Campbell, A. H. Castro Neto, and G. Japaridze.

6.A Exchange energy

The interaction Hamiltonian for ABC-stacked trilayer graphene is shown in Eq. (6.3). Fourier transforming ρ_n and $\Psi_{\sigma,n}$ leads to

$$\begin{aligned}\rho_n(\mathbf{q}) &= \int d\mathbf{r}\rho_n(\mathbf{r})e^{-i\mathbf{q}\cdot\mathbf{r}} = \sum_\sigma \int d\mathbf{r}\Psi^\dagger_{\sigma,n}(\mathbf{r})\Psi_{\sigma,n}(\mathbf{r})e^{-i\mathbf{q}\cdot\mathbf{r}} \\ &= \frac{1}{A}\sum_{\mathbf{k},\sigma}\Psi^\dagger_{\sigma,n}(\mathbf{k}+\mathbf{q})\Psi_{\sigma,n}(\mathbf{k}),\end{aligned} \tag{6.10}$$

in the discrete limit. Using Eq. (6.10) and Fourier transforming V^D, V^{ND} and V^{2ND} in Eq. (6.3), going to the discrete limit, and subsequently rewriting the resulting expression into a matrix form yields

$$H_I = \frac{1}{2A}\sum_{\mathbf{q}\neq 0}\begin{pmatrix}\rho_1(-\mathbf{q}) & \rho_2(-\mathbf{q}) & \rho_3(-\mathbf{q})\end{pmatrix} M \begin{pmatrix}\rho_1(\mathbf{q})\\ \rho_2(\mathbf{q})\\ \rho_3(\mathbf{q})\end{pmatrix},$$

where (by omitting the $\mathbf{q}$ dependence for brevity)

$$\begin{aligned}M &= M_t + M_r \\ &= \begin{pmatrix}V^D & V^{ND} & 0\\ V^{ND} & V^D & V^{ND}\\ 0 & V^{ND} & V^D\end{pmatrix} + \begin{pmatrix}0 & 0 & V^{2ND}\\ 0 & 0 & 0\\ V^{2ND} & 0 & 0\end{pmatrix}.\end{aligned} \tag{6.11}$$

The matrix M_t is diagonalized by U_t such that $U_t^T D_t U_t = M_t$ where

$$U_t = \frac{1}{2}\begin{pmatrix}-\sqrt{2} & 0 & \sqrt{2}\\ 1 & -\sqrt{2} & 1\\ 1 & \sqrt{2} & 1\end{pmatrix}, \quad D_t = \begin{pmatrix}v_1 & 0 & 0\\ 0 & v_2 & 0\\ 0 & 0 & v_3\end{pmatrix},$$

with $v_1 \equiv V^D$, $v_2 \equiv V^D - \sqrt{2}V^{ND}$ and $v_3 \equiv V^D + \sqrt{2}V^{ND}$. Similarly, M_r is diagonalized by U_r such that $U_r^T D_r U_r = M_r$ where

$$U_r = \begin{pmatrix}0 & 1 & 0\\ -1/\sqrt{2} & 0 & 1/\sqrt{2}\\ 1/\sqrt{2} & 0 & 1/\sqrt{2}\end{pmatrix}, \; D_r = \begin{pmatrix}0 & 0 & 0\\ 0 & -V^{2ND} & 0\\ 0 & 0 & V^{2ND}\end{pmatrix}.$$

Let us define

$$\frac{1}{\sqrt{2}}\begin{pmatrix}\tilde{\rho}_1\\ \tilde{\rho}_2\\ \tilde{\rho}_3\end{pmatrix} \equiv U_t \begin{pmatrix}\rho_1\\ \rho_2\\ \rho_3\end{pmatrix} = \frac{1}{\sqrt{2}}\begin{pmatrix}-\rho_1+\rho_3\\ \rho_1/\sqrt{2}-\rho_2+\rho_3/\sqrt{2}\\ \rho_1/\sqrt{2}+\rho_2+\rho_3/\sqrt{2}\end{pmatrix},$$
$$\frac{1}{\sqrt{2}}\begin{pmatrix}\tilde{\rho}_4\\ \tilde{\rho}_5\\ \tilde{\rho}_6\end{pmatrix} \equiv U_r \begin{pmatrix}\rho_1\\ \rho_2\\ \rho_3\end{pmatrix} = \frac{1}{\sqrt{2}}\begin{pmatrix}\sqrt{2}\rho_2\\ -\rho_1+\rho_3\\ \rho_1+\rho_3\end{pmatrix}.$$

Defining $\tilde{\varrho}_I(\mathbf{q}) = (\tilde{\rho}_1(-\mathbf{q}), \tilde{\rho}_2(-\mathbf{q}), \tilde{\rho}_3(-\mathbf{q}))^t$, $\tilde{\varrho}_{II}(\mathbf{q}) = (\tilde{\rho}_4(-\mathbf{q}), \tilde{\rho}_5(-\mathbf{q}), \tilde{\rho}_6(-\mathbf{q}))^t$, and using the above diagonalization yields

$$H_I = \frac{1}{2A}\sum_{\mathbf{q}\neq 0}\frac{\pi e^2}{\epsilon q}\tilde{\varrho}_I^t \begin{pmatrix}1 & 0 & 0\\ 0 & 1-\sqrt{2}e^{-qd} & 0\\ 0 & 0 & 1+\sqrt{2}e^{-qd}\end{pmatrix}\tilde{\varrho}_I$$
$$+\frac{1}{2A}\sum_{\mathbf{q}\neq 0}\frac{\pi e^2}{\epsilon q}\tilde{\varrho}_{II}^t \begin{pmatrix}0 & 0 & 0\\ 0 & -e^{-2qd} & 0\\ 0 & 0 & e^{-2qd}\end{pmatrix}\tilde{\varrho}_{II}.$$

By defining

$$V_1(q) \equiv \frac{\pi e^2}{\epsilon q}, \quad V_{2/3}(q) \equiv \frac{\pi e^2}{\epsilon q}(1 \mp \sqrt{2}e^{-qd}),$$

$$V_4(q) \equiv 0, \quad V_{5/6}(q) \equiv \frac{\pi e^2}{\epsilon q}(\mp e^{-2qd}),$$

the Hamiltonian reduces to the compact form

$$H_I = \frac{1}{2A}\sum_{\mathbf{q}\neq 0}\sum_{s=1}^{6}\tilde{\rho}_s(-\mathbf{q})V_s(\mathbf{q})\tilde{\rho}_s(\mathbf{q}).$$

Inspection of the operators $\tilde{\rho}_s$ for $s = 1, 2, \ldots, 6$, indicates that they are all linear combinations of $\rho_n(\mathbf{q})$ for $n = 1, 2, 3$. Thus, using Eq. (6.10) one obtains

$$\tilde{\rho}_s(\mathbf{q}) = \sum_{\mathbf{k}}\tilde{\Psi}^\dagger(\mathbf{k}+\mathbf{q})\tilde{\chi}_s\tilde{\Psi}(\mathbf{k})$$
$$= \sum_{\mathbf{k}}\Phi^\dagger(\mathbf{k}+\mathbf{q})\mathcal{M}^\dagger(\mathbf{k}+\mathbf{q})\tilde{\chi}_s\mathcal{M}(\mathbf{k})\Phi(\mathbf{k}),$$

where $\mathcal{M}(\mathbf{q})$ is the diagonalizing matrix of the ABC-stacked trilayer Hamiltonian, $\tilde{\Psi} \equiv (\tilde{\Psi}_1, \tilde{\Psi}_2, \tilde{\Psi}_3)$, with $\tilde{\Psi}_n(\mathbf{q}) \equiv \Psi_n(\mathbf{q})/\sqrt{A}$ being a two component dimensionless

annihilation operator working on layer n. The operator $\Phi^\dagger$ contains the band creation operators of the six bands. Thus, the six matrices $\tilde{\chi}^\alpha$ are defined as

$$\tilde{\chi}_{1/6} \equiv \begin{pmatrix} \mp\mathbf{1}_2 & 0 & 0 \\ 0 & 0 & 0 \\ 0 & 0 & \mathbf{1}_2 \end{pmatrix}, \quad \tilde{\chi}_4 \equiv \begin{pmatrix} 0 & 0 & 0 \\ 0 & \sqrt{2}\mathbf{1}_2 & 0 \\ 0 & 0 & 0 \end{pmatrix},$$
$$\tilde{\chi}_{2/3} \equiv \begin{pmatrix} \mathbf{1}_2/\sqrt{2} & 0 & 0 \\ 0 & \mp\mathbf{1}_2 & 0 \\ 0 & 0 & \mathbf{1}_2/\sqrt{2} \end{pmatrix},$$

where $\tilde{\chi}_5 \equiv \tilde{\chi}_1$. By defining $\chi^s \equiv \mathcal{M}^\dagger(\mathbf{k}+\mathbf{q})\tilde{\chi}_s\mathcal{M}(\mathbf{k})$ the ABC-stacked trilayer interaction Hamiltonian can be written as

$$H_I = \frac{1}{2A}\sum_{\mathbf{q}\neq 0}\sum_{\mathbf{p},\mathbf{p}'}\sum_{s=1}^{6}\sum_{\alpha,\beta,\mu,\nu=1}^{6}\Phi^\dagger_\alpha(\mathbf{p}-\mathbf{q})\chi^s_{\alpha\beta}(\mathbf{p}-\mathbf{q},\mathbf{p})$$
$$\times\,\Phi_\beta(\mathbf{p})V_s(\mathbf{q})\Phi^\dagger_\mu(\mathbf{p}'+\mathbf{q})\chi^s_{\mu\nu}(\mathbf{p}'+\mathbf{q},\mathbf{p}')\Phi_\nu(\mathbf{p}').$$

Let

$$|\mathbf{N}\rangle = \prod_{\mathbf{k},\nu,\sigma}\left[\Phi^\dagger_{\sigma,\nu}(\mathbf{k})\right]^{N_{\mathbf{k},\sigma,\nu}}|0\rangle$$

denote a Fock state of the system, where $N_{\mathbf{k},\sigma,\nu} \in \{0,1\}$ is the occupancy of electrons in the momentum state $\mathbf{k}$ of energy band ν with spin σ. Then, to first order, the energy of the system is described by

$$E_I = \langle\mathbf{N}| : H_I : |\mathbf{N}\rangle,$$

where : : denotes normal ordering. Working out the expectation value of H_I results in two distinct contributions. These are the Hartree (direct) and the Fock (exchange) contributions. Because of the Jellium background the Hartree contribution vanishes and only the Fock contribution remains. Thus,

$$E_{ex} = \frac{1}{2A}\sum_{\mathbf{p},\mathbf{p}'}\sum_{s=1}^{6}\sum_{\alpha,\beta=1}^{6}\sum_{\sigma,a}\mathcal{A}_{\sigma,\alpha,\beta,a}(\mathbf{p},\mathbf{p}')$$
$$\times\,\chi^s_{\alpha\beta}(\mathbf{p},\mathbf{p}')V_s(\mathbf{p}'-\mathbf{p})\chi^s_{\beta\alpha}(\mathbf{p}',\mathbf{p}),$$

where

$$\mathcal{A}_{\sigma,\alpha,\beta,a} = -\langle\mathbf{N}|\Phi^\dagger_{\sigma,\beta}(\mathbf{p})\Phi_{\sigma,\beta}(\mathbf{p})\Phi^\dagger_{\sigma,\alpha}(\mathbf{p}')\Phi_{\sigma,\alpha}(\mathbf{p}')|\mathbf{N}\rangle$$
$$= -n_{\sigma,\beta,a}(\mathbf{p}')n_{\sigma,\alpha,a}(\mathbf{p}),$$

and $n_{\sigma,\alpha,a}(\mathbf{p}')$ are Fermi occupation functions, which in the $T \to 0$ limit become Heaviside step functions representing the pocket configurations shown in Fig. 6.3.

Going to the continuum limit reproduces the result shown in Eq. (6.6). For further information on the numerical methods used to solve the exchange integral, see Ref. [176].

Chapter 7

Screening in ABC-stacked multilayer graphene

Abstract

In this Chapter we study the static polarization in ABC-stacked multilayer graphene. Since the density of states diverges for these systems if the number of layers exceeds three, screening effects are expected to be important. In the random phase approximation, screening can be included through the polarization. We derive an analytical integral expression for the polarization in both the full-band model and an effective two-band model. Numerical evaluation of these integrals are very time consuming in the full-band model. Hence, for ABC-stacked trilayer graphene, we use the two-band model to calculate the low momentum part of the polarization. The results for the two-band model are universal, i.e. indpendent of doping. The high momentum part is linear and is determined by calculating two points, such that we can determine the slope. For ABC stacked trilayer graphene, the slope is given by three times the monolayer value. The numerical results for the polarization of trilayer graphene are used to sketch the screened potential.[1] *After completion of this work we became aware of Ref. [178]. The results in this Chapter are obtained independently.*

7.1 Introduction

Stacking several layers of graphene on top of each other does not immediately lead to graphite. As long as the number of layers is small enough, the two-dimensional nature of the system is preserved, i.e. the (quasi) momentum of the particles is oriented within the plane. The properties of these systems depend heavily on the way the layers are stacked and typically differ considerably from both monolayer graphene and graphite.

[1] This Chapter is based on *Screening in multilayer graphene* , R. van Gelderen, R. Olsen, and C. Morais Smith, Arxiv:1304.5501 (2013).

There are two natural ways to stack graphene layers, namely AB or Bernal stacking and ABC (rhombohedral) stacking. In Bernal stacked multilayer graphene, the odd layers all have the same orientation, and so do the even layers. The orientation of the even layers is such that the $\mathcal{B}$ sublattice sites are opposite to the $\mathcal{A}$ sublattice sites of the layers directly beneath and above it. The $\mathcal{A}$ sublattice sites are located opposite to honeycomb centers. In rhombohedral stacked graphene, every layer is oriented such that the $\mathcal{B}$ sublattice is on top of the honeycomb centers of the layer beneath it and the $\mathcal{A}$ sublattice is on top of the $\mathcal{B}$ sublattice of the layer beneath it. This results in a cyclic structure through different orientations. Hence, the layers i and $i+3$ are exactly on top of each other. This lattice structure is shown in Fig. 7.1.

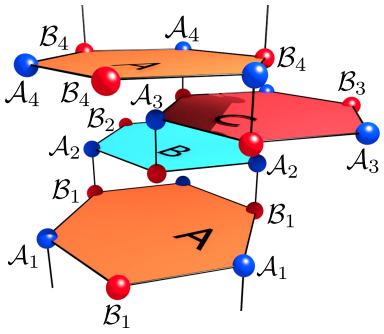

Figure 7.1: Atomic structure of ABC-stacked multilayer graphene.

Although a recent theoretical work investigates systems in which the stacking of the layers is partly Bernal and partly rhombohedral [55], so far most of the effort has been put into understanding either completely Bernal or completely rhombohedral stacked multilayer samples. These two systems behave very differently. In Bernal stacked multilayers, there are multiple low-energy bands, i.e. quasi particles with different dispersions. When the number of layers is even ($N = 2n$), the n low-energy conduction bands are all parabolic (bilayer-like), but with different effective masses, while for an odd number of layers ($N = 2n + 1$) a linear band with the same slope as the energy band in monolayer graphene exists next to the n parabolic ones [138]. The valence bands are related to the conduction bands by particle hole symmetry. On the other hand, for ABC-stacked multilayers, the low-energy physics takes place on the sublattice sites on the outer layers that do not have a direct neighbor in the next layer. As a result, it is possible to construct an effective 2×2 Hamiltonian that is valid for energies $E << t_\perp \approx 0.3$ eV [139]. From this effective model, it is easy to derive that the energy bands at small momenta and low energies disperse as $E \sim k^N$, i.e. the bands become very flat when N increases. At the K point, where the conduction and valence bands touch, the dispersion of the bands makes that the density of states diverges when $N \geq 3$. This is in sharp contrast to Bernal stacked graphene, where the density of states never diverges at the Dirac point.

The integer quantum Hall effect could be a way to identify the different stacking orders. This is because the Landau level spectrum is very different in the two

systems [181]. For example, in the trilayer case the Landau levels disperse with the magnetic field B as $E \sim B^{3/2}$ for rhombohedral stacking, while the linear and parabolic bands in Bernal stacked trilayers give rise to two sets of Landau levels. One set disperses as a graphene monolayer, $E_{\mathrm{ml}} \sim \sqrt{B}$, while the other behaves as $E_{\mathrm{bl}} \sim B$, just as a graphene bilayer does. Hence, the Landau levels cross as a function of the magnetic field [66]. This fundamental difference is true for any $N \geq 3$ multilayer system: When the stacking is Bernal the Landau levels cross, while for ABC-stacked systems they do not (as long as the high-energy bands are neglected). Due to the low mobility of most multilayer graphene samples, much higher magnetic fields are required to observe the quantization of the Hall conductance. Nevertheless, for both Bernal and rhombohedral stacked trilayer graphene the integer quantum Hall effect is observed in experiment [99, 152, 62]. In the Bernal stacked case, hexagonal boron nitride was used as a substrate, increasing the mobility by a factor of 100 [99]. This technique may be used in the future to observe the quantum Hall effect in graphene multilayers with an even higher number of layers.

Although the integer quantum Hall effect was observed promptly, it took much longer to confirm that the fractional quantum Hall effect exists in graphene. As a result, the importance of the Coulomb interaction in graphene has long been debated. Theoretical predictions of interaction effects had been made, such as a ferromagnetic phase transition in monolayer, bilayer, and later also in trilayer graphene [153, 154, 85, 86]. The observation of the fractional quantum Hall effect in 2009 confirmed that interactions do play a role in graphene physics. The groups of Eva Andrei and Philip Kim reported the quantum Hall plateau in suspended graphene with high mobility at filling factor $\nu = 1/3$, using a two-terminal device [37, 38]. However, a two-terminal setup cannot provide an unambiguous proof of the existence of the phenomenon. The issue has only been definitively settled after a four-terminal device was used to observe the $\nu = 1/3$ plateau in suspended graphene [179] and several other plateaus at fractional filling factors in graphene on hexagonal boron nitride [180]. The importance of interactions in graphene was later reiterated by other experiments, for example the renormalization of the Fermi velocity due to the Coulomb interaction in monolayers [182]. In addition, there is evidence that the fractional quantum Hall effect also occurs in suspended bilayer and trilayer samples [183].

The Coulomb interaction is always present in systems that consist of many charged particles, like electrons. The importance of electromagnetic interactions depends on the properties of the system. The ratio of the Coulomb to kinetic energy r_s is a measure of the influence that the Coulomb interaction has on the system. When the kinetic energy dominates and r_s is small, the system can be described as a Fermi liquid. When r_s is large new phases can occur. For a two-dimensional electron gas (2DEG), $r_s = m^* e^2/(\epsilon \hbar^2 \sqrt{\pi n_{\mathrm{el}}})$, where m^* is the effective

mass of the electrons, e the electron charge, ϵ the dielectric constant, and $n_{\rm el}$ the density of electrons. Hence, for low electron densities the Coulomb interaction dominates and other phases, for example a Wigner crystal, can form. The $n_{\rm el}^{-1/2}$ dependence is the result of the Coulomb interaction $\langle V\rangle \sim 1/\langle r\rangle \sim \sqrt{n_{\rm el}}$ and a quadratic kinetic energy $\langle K\rangle \sim k_F^2 \sim n_{\rm el}$. When the dispersion is not quadratic, r_s will become a different function of the electron density.

In monolayer graphene, the charge carriers behave as massless relativistic particles. Therefore, the kinetic energy scales with momentum or $\sqrt{n_{\rm el}}$, instead of momentum squared or $n_{\rm el}$ as it was the case in the 2DEG. Hence, the parameter r_s depends only on material parameters and is independent of electron doping $r_s = e^2/(\epsilon\hbar v_F)$ [155]. For graphene, ϵ is the average dielectric constant of the material below and above the graphene layer, i.e. $\epsilon = 1$ for suspended graphene in vacuum and $\epsilon = 2.5$ for graphene on a SiO_2 substrate. Thus, $r_s = 2.2$ and $r_s = 0.8$ for these two cases, respectively. Compared to a typical 2DEG, graphene is weakly interacting. However, close to the charge neutrality point the density of states vanishes. As a consequence, there are not many electrons available for screening and the Coulomb interaction is almost unscreened, thus remaining long ranged. Indeed, the Thomas-Fermi screening vector, which is the $k \to 0$ limit of the polarization, scales with the Fermi energy and therefore vanishes if the system is close to half filling [155]. In the short-wavelength limit, where k is large, the polarization is linear and, in this regime, the effect of screening is a renormalization of the interaction strength.

For bilayer graphene, the parameter r_s scales as $r_s \sim 1/\sqrt{n_{\rm el}}$ [155]. Hence, close to half filling, where $n_{\rm el} = 0$, the interaction term should dominate the kinetic term. However, not only is it very difficult to produce a charge neutral system, due to the formation of electron hole puddles [27], it is also no longer true that the Thomas-Fermi vector vanishes for $n_{\rm el} = 0$. The Thomas-Fermi vector is independent of the density of electrons in bilayer graphene. Therefore, screening is more profound in bilayers than in monolayers of graphene. The polarization can be calculated analytically and from the polarization it is possible to construct the screened potential [87]. Due to the two-dimensional nature of the system, the potential is not exponentially screened, but remains polynomial.

For ABC-stacked multilayers with three or more layers, the density of states diverges at the charge neutrality point. Since the Thomas-Fermi vector scales with the density of states, it is expected that screening is important for such systems. Nevertheless, not much is known about Coulomb interations in multilayer graphene systems.

The aim of this Chapter is to determine the polarization and the screened potential in rhombohedral stacked multilayers. Firstly, two models are introduced in section 7.2. In the full-band model the full $2N \times 2N$ Hamiltonian is used, while in the two-band model an effective 2×2 matrix is introduced. In section

7.3, the polarization is calculated in the two-band model and it is shown that this approximation breaks down for large momenta. Although we analytically derive the formal integrals which have to be solved to calculate the polarization in N layers of graphene, we solve the problem numerically only for ABC-stacked trilayer graphene, as an example. We also show results for the full-band model. The screened Coulomb potentials are derived for the two-band model in section 7.4 and a realistic sketch of the screened potential is drawn in the full-band model. We discuss our results in section 7.5.

7.2 The Model

7.2.1 Full-band Hamiltonian

To describe an ABC-stacked multilayer of graphene with N layers, we use a nearest-neighbor tight-binding model. Hence, the electrons can tunnel to adjacent lattice sites within the same layer (with energy $t = 3$ eV) or to direct neighbors at a distance $d = 3.4$ Å in other layers (with energy $t_\perp = 0.35$ eV). The noninteracting tight-binding Hamiltonian in real space is given by

$$H_0 = -\sum_{<l_i,l_j>,\sigma} \left(t a^\dagger_{l_i,\sigma} b_{l_j,\sigma} + t_\perp a^\dagger_{(l+1)_i,\sigma} b_{l_i,\sigma} + H.c. \right).$$

If $c \in \{a, b\}$, then $c^\dagger_{l_i,\sigma}$ ($c_{l_i,\sigma}$) creates (annihilates) an electron on lattice site i in layer $l \in \{1, 2, ..., N\}$ with spin $\sigma \in \{\uparrow, \downarrow\}$. Since the unit cell of this system contains $2N$ lattice sites, the reciprocal space representation of this Hamiltonian is a $2N \times 2N$ matrix. After expanding around the K point, the low-energy Hamiltonian is cast into the form,

$$\begin{aligned}
H_0 &= \int d^2\mathbf{k} \psi^\dagger(\mathbf{k}) \mathcal{H}_0 \psi(\mathbf{k}), \\
\mathcal{H}_0 &= \begin{pmatrix} H_{\mathrm{ml}} & B & 0 & 0 & \dots \\ B^T & H_{\mathrm{ml}} & B & 0 & \dots \\ 0 & \ddots & \ddots & \ddots & \end{pmatrix}, \\
H_{\mathrm{ml}} &= \hbar v_F \begin{pmatrix} 0 & k e^{i\phi(\mathbf{k})} \\ k e^{-i\phi(\mathbf{k})} & 0 \end{pmatrix}, \\
B &= \begin{pmatrix} 0 & 0 \\ t_\perp & 0 \end{pmatrix}, \\
\psi^\dagger(\mathbf{k}) &= \left(a^\dagger_1(\mathbf{k}), b^\dagger_1(\mathbf{k}), a^\dagger_2(\mathbf{k}), \dots, b^\dagger_N(\mathbf{k}) \right),
\end{aligned} \tag{7.1}$$

where $\hbar v_F = (3/2)at$ defines the Fermi velocity in monolayer graphene. Furthermore, k is the norm of the two-dimensional momentum vector, $k = |\mathbf{k}|$, and

$\phi(\mathbf{k}) = \arctan(k_y/k_x)$ is the angle of the momentum vector. In the following, we refer to Eq. 7.1 as the *Noninteracting full-band Hamiltonian.*

7.2.2 Two-band Hamiltonian

In an ABC-stacked multilayer, only the $\mathcal{A}$ sublattice in the bottom layer (layer 1) and the $\mathcal{B}$ sublattice in the top layer (layer N) do not have direct neighbors in an adjacent layer. The electrons on sites with a neighbor in an opposite layer will dimerise and the energy bands associated with these electrons will move away from the charge neutrality point. This results in two energy bands close to the charge neutrality point, while the other energy bands split away from zero by an energy $\sim t_\perp$. Hence, for an ABC-stacked multilayer of graphene, the low-energy physics takes place on the $\mathcal{A}_1$ and the $\mathcal{B}_N$ sites. Therefore, it is possible to construct an effective low-energy model that takes only the two energy bands into account that are closest to the Dirac point [98]. This low-energy Hamiltonian is a 2×2 matrix and since it takes N intra-plane and $N-1$ inter-plane hoppings to go from the $\mathcal{A}_1$ to the $\mathcal{B}_N$ site, it has the form,

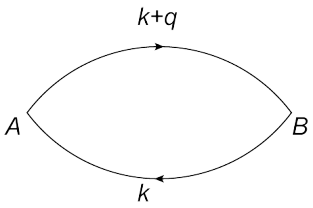

Figure 7.2: The bubble diagram Π_{AB}.

$$
\begin{aligned}
H_0^{2\mathrm{B}} &= t_\perp \left(\frac{\hbar v_F}{t_\perp}\right)^N \int d^2\mathbf{k} \psi_{2B}^\dagger(\mathbf{k}) \mathcal{H}_0^{2\mathrm{B}} \psi_{2B}(\mathbf{k}), \\
\mathcal{H}_0^{2\mathrm{B}} &= \begin{pmatrix} 0 & k^N e^{-iN\phi(\mathbf{k})} \\ k^N e^{iN\phi(\mathbf{k})} & 0 \end{pmatrix}, \\
\psi_{2B}^\dagger(\mathbf{k}) &= (a_1^\dagger(\mathbf{k}), b_N^\dagger(\mathbf{k})).
\end{aligned}
\tag{7.2}
$$

We will refer to the Hamiltonian in Eq. 7.2 as the *Noninteracting two-band Hamiltonian.* This Hamiltonian is valid for small momenta at which the energies are much smaller than $t_\perp$.

7.3 The Polarization Bubble

The Feynman diagram of the polarization is shown in Fig. 7.2. In the random phase approximation, this bubble diagram can be used to compute the screened potential or the free energy in an infinite order expansion. The screened part of the potential can also be absorbed into the dielectric constant. By doing so, one can relate the polarization to the electromagnetic susceptibility $\chi(\omega, \mathbf{k})$, which is defined by $\epsilon(\omega, \mathbf{k}) = 1 + 4\pi\chi(\omega, \mathbf{k})$, and measures the tendency of the medium to adjust to an external electromagnetic perturbation. Furthermore, the $k \to 0$ limit

of the polarization gives the Thomas-Fermi screening vector. The dynamical part of the polarization is needed to describe plasmons, but those will not be treated in this Chapter. Here, we focus on the static polarization, for which $\omega = 0$.

7.3.1 Two-band model

In this section, we will calculate the polarization and subsequently the screened Coulomb interactions in the two-band model. We can neglect spin in this problem. The Hamiltonian is a matrix and hence, the bubble diagram will have indices labeling lattice site. For convenience, we indicate the $\mathcal{A}_1$ sites by A and the $\mathcal{B}_N$ sites by B. The polarization is given by

$$\Pi = \begin{pmatrix} \Pi_{AA} & \Pi_{AB} \\ \Pi_{BA} & \Pi_{BB} \end{pmatrix},$$

$$\Pi_{ij}(i\omega_m, \mathbf{k}) = T\sum_n \int \frac{d^2q}{(2\pi)^2} G_{ij}(i\Omega_n + i\omega_m, \mathbf{q}+\mathbf{k}) G_{ji}(i\Omega_n, \mathbf{q}), \tag{7.3}$$

where $G_{ij}(i\omega, \mathbf{k})$ is the electron propagator between the lattice sites i and j, ω_m and Ω_n are Matsubara frequencies, and T is temperature. In Fig. 7.2 the Feynman diagram of the Π_{AB} bubble is shown.

The propagator, which is a 2×2 matrix in the two-band model, is given by $G(i\omega, \mathbf{k}) = (i\omega \mathbb{1} - \mathcal{H}_0^{2\mathrm{B}})^{-1}$, where $\mathbb{1}$ is the identity matrix. A derivation of the propagator in the full-band model is given in the appendix of this Chapter (section 7.A), but can be applied in the two-band model as well. The diagonalization matrices of $\mathcal{H}_0^{2\mathrm{B}}$ are defined as

$$U_{\mathbf{k}} = \frac{1}{\sqrt{2}} \begin{pmatrix} 1 & e^{-Ni\phi(\mathbf{k})} \\ e^{Ni\phi(\mathbf{k})} & -1 \end{pmatrix},$$

$$U_{\mathbf{k}}^\dagger \mathcal{H}_0^{2\mathrm{B}} U_{\mathbf{k}} = D_k = \mathrm{diag}(\alpha k^N, -\alpha k^N),$$

where we have defined $\alpha \equiv t_\perp (\hbar v_F / t_\perp)^N$. Let us denote $\xi_k^s = s\alpha k^N$, where $s = \pm$. Then,

$$\begin{aligned} G(i\omega, \mathbf{k}) &= U_{\mathbf{k}}^\dagger (i\omega_m - D_k)^{-1} U_{\mathbf{k}}, \\ &= \sum_s \frac{1}{i\omega_m - \xi_k^s} U_{\mathbf{k}}^\dagger \Delta^s U_{\mathbf{k}}, \\ \Delta^+ &= \mathrm{diag}(1, 0), \\ \Delta^- &= \mathrm{diag}(0, 1). \end{aligned}$$

Writing $G(i\omega_m, \mathbf{k})$ in this form allows us to perform the Matsubara sum in expression (7.3) for the polarization:

$$
\begin{aligned}
\Pi_{ij}(i\omega_m,\mathbf{k}) &= T\sum_n \int \frac{d^2q}{(2\pi)^2} G_{ij}(i\Omega_n + i\omega_m, \mathbf{q}+\mathbf{k}) G_{ji}(i\Omega_n,\mathbf{q}),\\
&= T\sum_n \int \frac{d^2q}{(2\pi)^2} \sum_{s,s'} \frac{1}{i\Omega_n + i\omega_m - \xi^s_{|\mathbf{k}+\mathbf{q}|}} \frac{1}{i\Omega_n - \xi^{s'}_q} F^{ss'}_{ij}(k,q,\theta),\\
&= \int \frac{d^2q}{(2\pi)^2} \sum_{s,s'} \frac{n(\xi^s_{|\mathbf{k}+\mathbf{q}|}) - n(\xi^{s'}_q)}{i\omega_m + \xi^s_{|\mathbf{k}+\mathbf{q}|} - \xi^{s'}_q} F^{ss'}_{ij}(k,q,\theta), \qquad (7.4)\\
F^{ss'}_{ij}(k,q,\theta) &= \left(U^\dagger_{\mathbf{k}+\mathbf{q}} \Delta^s U_{\mathbf{k}+\mathbf{q}}\right)_{ij} \left(U^\dagger_{\mathbf{q}} \Delta^{s'} U_{\mathbf{q}}\right)_{ji},\\
&= \frac{1}{4}\left\{\delta_{ij} + ss'(1-\delta_{ij})\cos\left[N\phi(\mathbf{k}+\mathbf{q}) - N\phi(\mathbf{q})\right]\right\},\\
&= \frac{1}{4}\left\{\delta_{ij} + ss' \frac{(1-\delta_{ij})}{(k^2+q^2+2kq\cos\theta)^{N/2}} \times \right.\\
&\quad \left. \sum_{m=0}^{N} \begin{pmatrix} N \\ m \end{pmatrix} (q+k\cos\theta)^m (k\sin\theta)^{N-m} \cos\left(\frac{1}{2}(N-m)\pi\right)\right\},
\end{aligned}
$$

where θ is the angle between $\mathbf{k}$ and $\mathbf{q}$ and $n(\xi^s)$ is the occupation function of the energy band s. Note that $\cos\left(\frac{1}{2}(N-m)\pi\right) \in \{-1,0,1\}$. For fixed N, we have determined the structure factor $F^{ss'}_{ij}(k,q,\theta)$ analytically. In the two-band model, this factor depends on θ and on the ratio q/k. In the full band model we can only determine this factor numerically. Since it is (in that case) a function of k, q, and θ, it will slow down the calculations.

Zero Fermi energy

Let us first consider the half-filled system for which $E_F = 0$. In this case, the valence band is completely filled, while the conduction band is empty,

$$n(\xi^+_k) = 0, \qquad n(\xi^-_k) = 1.$$

Let us define $x = q/k$; then the expression (7.4) for the polarization can be written as

$$
\begin{aligned}
\Pi^0_{ij}(i\omega_m,k) = \frac{-1}{k^{N-2}} \int \frac{x\,dx\,d\theta}{2\alpha\pi^2}\\
\times \frac{(1+x^2+2x\cos\theta)^{N/2} + x^N - i\omega_m/(\alpha k^N)}{\left[(1+x^2+2x\cos\theta)^{N/2} + x^N\right]^2 + \left(\frac{\omega_m}{\alpha k^N}\right)^2} F^{ss'}_{ij}(1,x,\theta).
\end{aligned}
$$

To arrive at this expression, we made the denominator real and filled in the expression for ξ^s_k. It is now obvious that the polarization is real, as long as $\omega_m = 0$ (static screening). For static screening, one may extract the k dependence of the

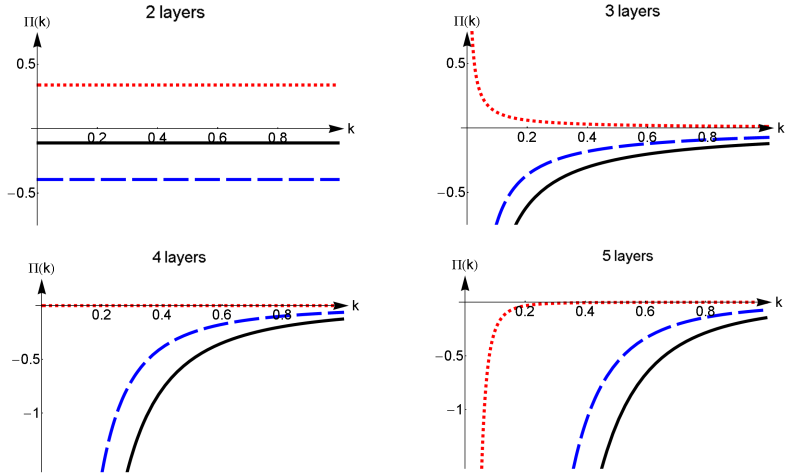

Figure 7.3: Plot of $\alpha\Pi^0_{AA}(\omega = 0, k)$ (blue dashed line), $\alpha\Pi^0_{AB}(\omega = 0, k)$ (red dotted line), and $\alpha\Pi^0_{\text{tot}}(\omega = 0, k)$ (black solid line) in the two-band model for a different number of layers and $k_F = 0$.

polarization out of the integral, which will yield a constant that can be determined numerically. For the ABC-stacked trilayer, one finds that

$$\Pi^0_{AA}(k) = \Pi^0_{BB}(k) = -\left(\frac{5.743}{8\alpha\pi^2}\right)\frac{1}{k} = -\frac{0.0727}{\alpha k},$$
$$\Pi^0_{AB}(k) = \Pi^0_{BA}(k) = \left(\frac{0.955}{8\alpha\pi^2}\right)\frac{1}{k} = \frac{0.0121}{\alpha k},$$
$$\Pi^0_{\text{tot}}(k) \equiv 2\left[\Pi^0_{AA}(k) + \Pi^0_{BA}(k)\right] = -\left(\frac{9.576}{8\alpha\pi^2}\right)\frac{1}{k} = -\frac{0.1213}{\alpha k}.$$

We conclude that for an undoped trilayer, the polarization goes as $\sim 1/k$ and therefore diverges as $k \to 0$. This is expected, because the long wavelength limit of the bubble is proportional to the density of states at the Fermi energy and for an ABC-stacked trilayer the density of states diverges at the Dirac point. This singular behavior is present for all ABC-stacked multilayers with $N \geq 3$, as can be seen in Fig. 7.3.

Nonzero Fermi energy

Now, let us assume a nonzero Fermi energy $E_F > 0$. In this case, the conduction band is partially filled. Hence, the occupation functions become

$$n(\xi^+_k) = \Theta(k_F - k), \qquad n(\xi^-_k) = 1,$$

where $\Theta(x)$ is the Heaviside theta function and k_F is the Fermi momentum. If we write down the expression for the polarization, we recognize the expression for the half filled case, $\Pi^0_{ij}(k)$ plus a correction

$$\begin{aligned}\Pi_{ij}(i\omega_m,k) = \int \frac{qdqd\theta}{4\alpha\pi^2}\Bigg\{ & \frac{\left[n(\xi^+_{|\mathbf{k}+\mathbf{q}|})-n(\xi^-_q)\right]F^{+-}_{ij}(k,q,\theta)}{(k^2+q^2+2kq\cos\theta)^{N/2}+q^N+\frac{i\omega_m}{\alpha k^N}} \\ & - \frac{\left[n(\xi^-_{|\mathbf{k}+\mathbf{q}|})-n(\xi^+_q)\right]F^{-+}_{ij}(k,q,\theta)}{(k^2+q^2+2kq\cos\theta)^{N/2}+q^N-\frac{i\omega_m}{\alpha k^N}} \\ & + \frac{\left[n(\xi^+_{|\mathbf{k}+\mathbf{q}|})-n(\xi^+_q)\right]F^{++}_{ij}(k,q,\theta)}{(k^2+q^2+2kq\cos\theta)^{N/2}-q^N+\frac{i\omega_m}{\alpha k^N}}\Bigg\} \\ = \Pi^0(\omega_m,k)_{ij} + & \\ \frac{1}{k^{N-2}}\int \frac{xdxd\theta}{4\alpha\pi^2}\Bigg\{ & \frac{\Theta(k_F/k-\sqrt{1+x^2+2x\cos\theta})F^{+-}_{ij}(1,x,\theta)}{(1+x^2+2x\cos\theta)^{N/2}+x^N+\frac{i\omega_m}{\alpha k^N}} \\ & + \frac{\Theta(k_F/k-x)F^{-+}_{ij}(1,x,\theta)}{(1+x^2+2x\cos\theta)^{N/2}+x^N-\frac{i\omega_m}{\alpha k^N}} \\ & + \frac{\left[\Theta(k_f/k-\sqrt{1+x^2+2x\cos\theta})-\Theta(k_F/k-x)\right]F^{++}_{ij}(1,x,\theta)}{(1+x^2+2x\cos\theta)^{N/2}-x^N+\frac{i\omega_m}{\alpha k^N}}\Bigg\}.\end{aligned}$$

The term with $F^{--}_{ij}(1,x,\theta)$ vanishes, because both occupation functions are unity and therefore cancel each other out. In the language of Ref. [178], the first three terms form the interband polarization and the last term is the intraband polarization. From the expression above, we learn that only the extra terms with respect to the undoped case depend on the Fermi momentum. These correction terms contain two Heaviside theta functions. One of them, $\Theta(k_F/k-x)$, is nonzero only within a circle of radius $\delta = k_F/k$ around the origin, while the other one, $\Theta(k_F/k-\sqrt{1+x^2+2x\cos\theta})$, is nonzero within a distance δ from the point $(1,0)$. Since $\delta \to 0$ when $k \to \infty$, these correction terms will go to zero for large momenta. We conclude that, within the two band model, the large momentum dependence of the polarization always equals that of the half-filled system. Note that for $k_F/k < 1/2$, i.e. $k > 2k_F$, the two regions where the Heaviside functions are nonzero do not overlap. For $k < 2k_F$ these two regions do overlap and this explains the cusp in the polarization at $k = 2k_F$.

The long wavelength limit of the polarizations are given by

$$\Pi^{\text{tot}}(k\to 0) = -\frac{g_D}{2\pi}k_F\left|\frac{d\xi_p}{dp}\right|^{-1}_{p=k_F}, \tag{7.5}$$

where g_D is the degeneracy factor due to spin and valley. This condition is indeed satisfied by the numerical results we have found for the trilayer case. In Fig. 7.4a

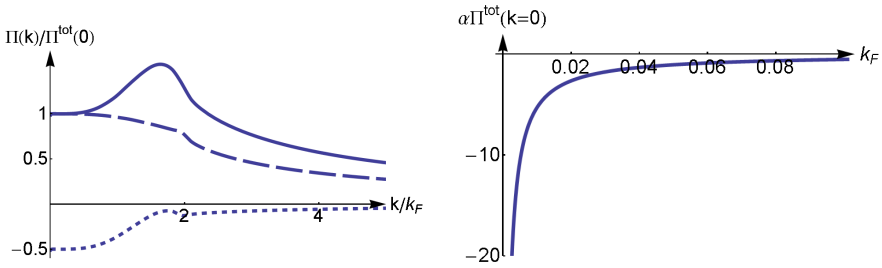

(a) (b)

Figure 7.4: (a) The normalized polarization functions for ABC-stacked trilayer graphene in the two-band model: $\Pi_{AA}(k)$ (dashed line), $\Pi_{AB}(k)$ (dotted line), and $\Pi^{\text{tot}}(k)$ (solid line). This plot is universal as long as $k_F \neq 0$. (b) Plot of $\alpha\Pi^{\text{tot}}(\omega = 0, k = 0)$ as a function of k_F.

the components $\Pi_{ij}(k)$ and $\Pi^{\text{tot}}(k)$ are plotted for a nonzero Fermi momentum in the ABC-stacked trilayer. After scaling the axes as is done in the figure, the plot is universal, i.e. independent of Fermi momentum. The total polarization is also the sum of an intraband and an interband contribution, $\Pi^{\text{tot}}(k) = \Pi^{\text{tot}}_{\text{intra}}(k) + \Pi^{\text{tot}}_{\text{inter}}(k)$. In Ref. [178], both contributions are plotted separately. In their paper, the authors show that for small momenta an expansion can be made. The leading terms of both the intraband and interband polarizations are quadratic and exactly cancel. As a result, $\Pi^{\text{tot}}(k)$ increases slowly as k^4 for small momenta. For large momenta, the interband polarization dominates. This agrees with our argumentation above that for large momenta the polarization converges to the case where $k_F = 0$, because for $k_F = 0$ the intraband contribution to the polarization is zero.

7.3.2 The full-band model

For the full-band model, the expression for the polarization can be derived in a similar way as we did to obtain Eq. (7.4). The main difference is that all the matrices are now $2N \times 2N$ and in general, cannot be calculated analytically anymore. A derivation for the propagator is shown in the appendix of this Chapter

(section 7.A). We have that

$$\begin{aligned}\Pi_{ij}(i\omega_m,\mathbf{k}) &= T\sum_n \int \frac{d^2q}{(2\pi)^2} G_{ij}(i\Omega_n + i\omega_m, \mathbf{q}+\mathbf{k}) G_{ji}(i\Omega_n,\mathbf{q}),\\ &= T\sum_n \int \frac{d^2q}{(2\pi)^2} \sum_{s,s'} \frac{1}{i\Omega_n + i\omega_m - \xi^s_{|\mathbf{k}+\mathbf{q}|}} \frac{1}{i\Omega_n - \xi^{s'}_q} F^{ss'}_{ij}(k,q,\theta),\\ &= \int \frac{d^2q}{(2\pi)^2} \sum_{s,s'} \frac{n(\xi^s_{|\mathbf{k}+\mathbf{q}|}) - n(\xi^{s'}_q)}{i\omega_m + \xi^s_{|\mathbf{k}+\mathbf{q}|} - \xi^{s'}_q} F^{ss'}_{ij}(k,q,\theta),\\ F^{ss'}_{ij}(k,q,\theta) &= \left(U^\dagger_{\mathbf{k}+\mathbf{q}} \Delta^s U_{\mathbf{k}+\mathbf{q}}\right)_{ij} \left(U^\dagger_{\mathbf{q}} \Delta^{s'} U_{\mathbf{q}}\right)_{ji},\end{aligned}$$

where i,j now label the $2N$ different sublattice sites, s and s' label the $2N$ energy bands, and therefore Δ^s are matrices with zero's everywhere, except for a 1 in the s^{th} entry along the diagonal. $U_{\mathbf{k}}$ is the diagonalization matrix of Hamiltonian (7.1). For the full-band model we define $\Pi^{\text{tot}}(k) = \sum_{i,j=1}^{2N} \Pi_{ij}(k)$.

The computation of the static polarization ($\omega = 0$) is very tedious if the number of layers is greater than three. We can argue how $\Pi^{\text{tot}}(k)$ behaves in the short- and long-wavelength limit. The relation (7.5) still holds and therefore we can plot $\Pi(\omega = 0, k = 0)$ as a function of Fermi momentum (Fig. 7.4b). As expected, in the small-k limit the total polarization of the full model agrees with the results we found in the two-band model.

k/k_F	$\Pi^{\text{tot}}(k)$
6	0.018
7	0.021

Table 7.1: Numerical values of $\Pi^{\text{tot}}(k)$ in ABC-stacked trilayer graphene for $k_F = 0.017$.

Although the two band model describes the polarization well for small momenta, the short-wavelength behavior differs dramatically. We found that in the two-band model $\Pi^{\text{tot}}(k \to \infty) \sim 1/k^{N-2}$. This relation was induced by the k^N dispersion. In the full band model, this dispersion relation is only valid for momenta close to the Dirac point. For larger momenta, the dispersion of the bands eventually becomes linear. If k is large, this linear regime of the dispersion dominates the polarization integral and therefore $\Pi(k \to \infty) \sim k$, as is the behavior for monolayer graphene [184]. Hence, the short-wavelength limit of the static bubble is linear. This linearity is independent of N. The slope does depend on the number of layers, but not on the Fermi energy. For trilayer graphene we have confirmed the linear behavior for a fixed Fermi energy ($k_F = 0.017$) through a straight forward numerical calculation. This very time consuming process resulted in two points that align perfectly with the origin (see Table 7.1), confirming that $\Pi^{\text{tot}}(k \to \infty) = -\gamma k$, with $\gamma \approx 0.18$. In Fig. 7.5a, the two limiting regions of $\Pi^{\text{tot}}(k)$ are shown. The low momentum behavior, computed in the two-band model, is universal after scaling. Since the slope of the linear part is fixed, it is not invariant after scaling and therefore depends on

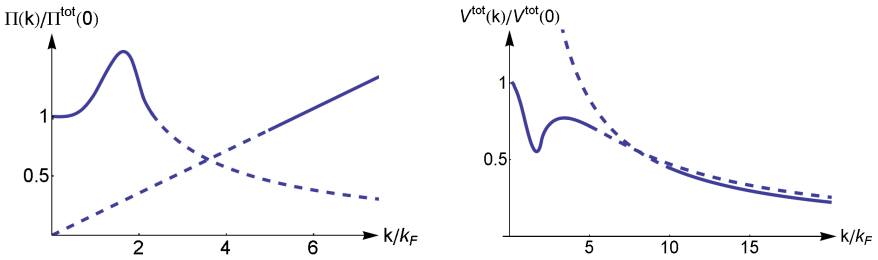

(a) (b)

Figure 7.5: The solid lines sketch (a) the full-band polarization and (b) the full-band screened potential $V^{\text{tot}}(k)$ for ABC-stacked trilayer graphene. The low-k regime is obtained in the two-band model and the high-k regime is obtained through a direct numerical computation. (a) The full-band polarization for $k_F = 0.016$. (b) The full-band screened potential for ($k_F = 0.005$). In the high-k regime the potential becomes a rescaled version of the unscreened potential $V(k) = 1/k$.

k_F. Hence, the total polarization in the full-band model is no longer universal. In Ref. [178], the total polarization for both ABC-stacked and ABA-stacked trilayer graphene is shown for different electron densities n_{el}, i.e., differen Fermi momenta. For high electron densities, related to the Fermi momentum through $k_F = \sqrt{\pi n_{\text{el}}}$, the crossover to the linear regime is at such small k/k_F that the bump of the polarization in the two-band model gets reduced.

In this thesis, we concentrated on the behavior of the polarization in the static limit ($\omega_m \to 0$). A generalization to include the dynamical part would be an interesting topic for further studies.

7.4 The screened potentials

7.4.1 Two-band model

Now that we have obtained the polarization functions, it is possible to determine the screened Coulomb potentials. In the two band model we only have the potentials within the layers and the potential between the first and Nth layer, since the low-energy physics takes place on the $\mathcal{A}_1$ and $\mathcal{B}_N$ sublattice sites. It is difficult to estimate the results for the nearest-layer potentials, $V_{\mathcal{A}_1\mathcal{B}_2}(k)$ for example, since we cannot say anything about the nearest-neighbor polarizations, e.g. $\Pi_{\mathcal{A}_1\mathcal{B}_2}$. In fact, in the full-band model we need all the components of the polarization matrix, if

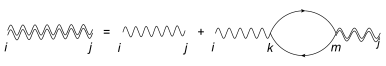

Figure 7.6: The Dyson equation, which is a matrix equation.

we want to calculate any screening potential. Nevertheless, let us use the two band model for now and discuss its limitations later.

The screened potentials are solutions of a Dyson equation (see Fig. 7.6). However, since the potentials carry two layer indices, the Dyson equation is a matrix equation in this case. We focus now on the trilayer case. If one writes down the equations for the intralayer potential $V_{\mathcal{A}_1\mathcal{A}_1}(k) = V_{\mathcal{B}_3\mathcal{B}_3}(k) \equiv V_{AA}(k)$ and the interlayer potential $V_{\mathcal{A}_1\mathcal{B}_3}(k) \equiv V_{AB}(k)$, one notices that they are coupled. By defining Υ as

$$\begin{aligned}\Upsilon(\mathbf{k}) = &\{[V_{AA}(k) - V_{AB}(k)][\Pi_{AA}(k) - \Pi_{AB}(k)] - 1\} \\ &\times \{[V_{AA}(k) + V_{AB}(k)][\Pi_{AA}(k) + \Pi_{AB}(k)] - 1\},\end{aligned}$$

the solutions are given by

$$\begin{aligned}V_{11}(k) &= \frac{V_{AA}(k) - \Pi_{AA}(k)[V_{AA}(k)^2 - V_{AB}(k)^2]}{\Upsilon(\mathbf{k})}, \\ V_{13}(k) &= \frac{V_{AB}(k) - \Pi_{AB}(k)[V_{AB}(k)^2 - V_{AA}(k)^2]}{\Upsilon(\mathbf{k})},\end{aligned}$$

where the bare interactions read

$$\begin{aligned}V_{AA}(k) &= \frac{1}{k}, \\ V_{AB}(k) &= \frac{e^{-2kd}}{k},\end{aligned}$$

and d is the interlayer distance. The screened potentials are shown in Fig. 7.7. For convenience we have also defined $V^{\mathrm{tot}}(k) = 1/[k + \Pi^{\mathrm{tot}}(k)]$, which is the solution to the Dyson equations if we set all exponentials $\exp(-2kd)$ equal to unity, which is a valid approximation when k is small. $V^{\mathrm{tot}}(k)$ has the same features as the real solutions, but because of its much simpler form, it will be convenient to use this potential during more in depth discussions.

Although this approximation describes well the screening for small momenta, the large k behavior of the polarization in the full band model is different than the $1/k^{N-2}$ decay in the two-band model. Hence, the screened potentials in the two-band model will also be incorrect in the large-k limit.

7.4.2 Full-band model

The screened potentials in the full-band model are also solutions of the Dyson equation sketched in Fig. 7.6, which, for trilayer graphene, is now a 6×6 matrix equation. The solution is given by

$$V^{\mathrm{scr}} = (\mathbb{1} - V\Pi)^{-1} V.$$

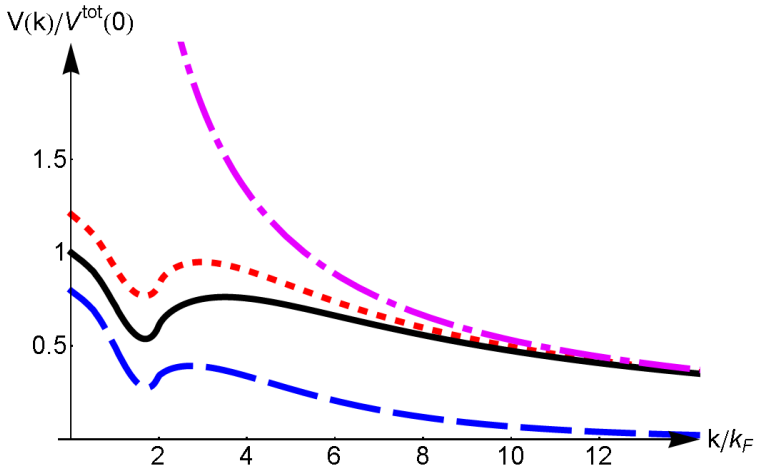

Figure 7.7: The screened potentials in the two-band model: V_{AA} (red dotted line), V_{AB} (blue dashed line), and V^{tot} (black solid line). The unscreened interaction $V(k) = 1/(k)$ is given by the purple dotdashed line. The interlayer distance d is set equal to 1 and $k_F = 0.1$.

It is easy to obtain the screened potentials numerically, once all components of the polarization are known. However, as we have seen previously, the calculation of the components of Π is numerically very time consuming in the full-band model. Nevertheless, we obtained a realistic sketch of $\Pi^{\text{tot}}(k) = \sum_{i,j=1}^{2N} \Pi_{ij}(k)$. As before, when we put the exponentials in the potentials to unity (equivalently put $d = 0$), the screened potential reduces to $V^{\text{tot}}(k) = 1/[k + \Pi^{\text{tot}}(k)]$. Therefore we can sketch $V^{\text{tot}}(k)$ as well, which is done in Fig. 7.5b.

7.5 Discussions

In this Chapter we have derived an expression for the polarization for ABC-stacked multilayer graphene. The calculations were performed within both the full-band model and the two-band model, an effective low-energy model in which the $2N \times 2N$ matrices reduce in size to 2×2. The advantage of the effective model is that it becomes easier to calculate the polarization numerically. The drawback is that the large-k behavior of the polarization becomes flawed. Instead of the linear behavior $\Pi \sim -\gamma k$ at large k, which is imposed by the linearity of the energy bands farther away from the Dirac points, the polarization drops off as $1/k^{N-2}$ in the two-band model. It is very time consuming to calculate the full-band polarization numerically, such that the results of the two-band model are of great help to understand the behavior of $\Pi^{\text{tot}}(k) = \sum_{i,j=1}^{2N} \Pi_{ij}(k)$ in the full-band model. One

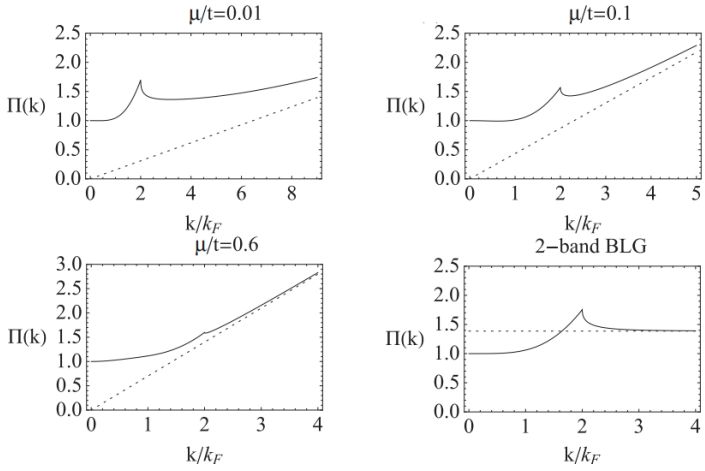

Figure 7.8: Rescaled polarization ($\Pi^{\mathrm{tot}}(k)$) for the graphene bilayer. Picture extracted from Ref. [87]. μ is the Fermi energy and t equals $t_\perp$ in the notation used throughout this Chapter.

has to be aware that in the effective model only the $\mathcal{A}_1$ and $\mathcal{B}_N$ lattice sites are involved. Therefore, we can say nothing about the polarization functions between other lattice sites in this approximation.

We have confirmed the linear behavior of $\Pi^{\mathrm{tot}}(k)$ for the ABC-stacked trilayer by calculating two points in the full-band model at high momenta. These two points align with the origin, confirming the linear asymptote. Although we do not know the exact crossover between the low momentum and the linear regime, we can sketch the total polarization (see Fig. 7.5a). The curves obtained in the two-band model for the polarization are universal after scaling, the crossover to the linear regime is not. This is because the slope of the linear regime is constant. After scaling however, the slope becomes $-\gamma/\Pi^{\mathrm{tot}}(0)$. Since $|\Pi^{\mathrm{tot}}(0)|$ is decreasing as a function of k_F (see Fig. 7.4b), the linear asymptote will become steeper in the scaled plots when k_F is increased. For example, the crossover to the linear regime is around $2k_F$ for $E_F/\alpha = 0.03$ ($k_F = 0.3$), while it is around $8k_F$ for $E_F/\alpha = 0.001$ ($k_F = 0.1$). Hence, the polarization is no longer universal after scaling in the full-band model.

Comparing our results for the ABC-stacked trilayer with the full-band [87] and two-band [185] results for the bilayer, which are shown in Fig. 7.8, we see some similarities. As long as the Fermi energy is nonzero the total polarization is finite everywhere. The $k \to 0$ limit is proportional to the density of states, just as in the bilayer case. This is in fact true for any N-layer ABC-stacked sample. It is important to realize that, although the plots look similar, the absolute values of

$\Pi^{\text{tot}}(k \to 0)$ are much higher for the ABC-stacked trilayer than for the bilayer. This is because the density of states is much higher. The normalized polarization has a peak as k increases and then a crossover to a linear regime takes place if k is further increased. This crossover is not captured by the two-band model. There are also differences in the behavior of bilayer and trilayer samples. The peak in the bilayer is located exactly at $2k_F$ and has a discontinuity in the first derivative. For the trilayer the peak is smoother and the maximum is reached before $2k_F$. The discontinuity in the first derivative at $2k_F$ remains, although it is less pronounced. In Ref. [178] it is pointed out that the cusp at $2k_F$ is characteristic for multilayers with an even number of layers. It arises from an enhancement of $2k_F$ backscattering processes, while for an odd number of layers backscattering is suppressed. For an odd number of layers, the discontinuity at $2k_F$ is not in the first derivative, but in the second derivative. Also for the bilayer the crossing to the linear regime is shifting to smaller momenta (measured in units of k_F) when the Fermi momentum increases. The slope of the linear part is different for the trilayer compared with the bilayer (and the monolayer). This can be explained by the existence of more valence bands which are filled in the trilayer. In general, for an ABC-stacked N-layer system, there are $N-1$ filled valence bands (and also $N-1$ empty conduction bands) further away from zero energy. These bands are expected to give a contribution when computing the full-band polarization. Hence, there is no reason that the slope of the linear asymptote should be independent of layer number N. We expect that the slope of the linear part of the total polarization increases further when N grows larger. The static polarization for monolayer graphene is constant up to $k = 2k_F$ and then becomes linear with a slope $\gamma_{\text{m.l.}} = 1/16$ [184]. Comparing this with the slope of the bilayer $\gamma_{\text{b.l.}} = 1/8 = 2/16$, and the trilayer $\gamma = 0.18 \approx 3/16$, a trend is seen. Although our results are not accurate enough, this is an indication that the slope of the linear part of the polarization scales linearly with the number of layers.

The unscreened Coulomb potential $V(k) = g/k$ with interaction strength g diverges as $k \to 0$. If $k_F = 0$, the polarization diverges as well for $k \to 0$. The screened potential will converge to zero in this limit, $V^{\text{tot}}(k \to 0) = 0$. When $k_F \neq 0$, the potential will be finite and nonzero everywhere. The screened potential has a local minimum and will converge to a renormalized version of the unscreened potential in the large-k limit. Due to the linear behavior of the polarization $\Pi^{\text{tot}}(k) = -\gamma k$ at large momenta, the screened potential is just the unscreened one with a renormalized interaction strength in this regime. The new interaction strength has the form

$$\tilde{g} = \frac{g}{1+\gamma}.$$

Since γ is positive, the interaction strength will be reduced. A sketch of the screened potential is shown in Fig. 7.5b.

With the insights gained in this Chapter, we conclude that the simplified model for the polarization proposed in Chapter 6 can be further refined. Indeed, instead of using the slope for the bilayer, $\gamma = 0.125$, we have found that the precise value for trilayers should be $\gamma = 0.18$. As a result, the critical couplings, and therefore also the critical doping levels, are reduced. The reduction of the interaction parameter g becomes larger when g increases. For $g = 6$ the extra reduction is around 28%. Since the phase boundary $n_{\mathrm{crit}}(g)$ is quite flat for $g > 1$ (see Fig. 6.5), the critical curve in the screened case will not change drastically.

In sum, the results presented here allow one to determine the effect of (static) screening in N layers of ABC-stacked graphene and should thus contribute to more accurate calculations of interaction phenomena in multilayer graphene. The number of trilayer experiments is increasing over the last few years, hence theoretical work is needed as well. By connecting the universal low-momentum part and the known high-momentum linear regime of the polarization, our numerical data could be used to include screening in a more realistic manner in the description of these fascinating materials.

Acknowledgments

The authors acknowledge financial support from the Netherlands Organization for Scientific Research (NWO), as well as useful discussions with L. Fritz and useful correspondence with O.V. Gamayun. The authors thank V. Juričić for proof reading this Chapter.

7.A Green's function

In order to derive the non-interacting Green's function for ABC-stacked multilayer graphene, we can use the Feynman path integral formalism as we did in Chapter 3. Using the definitions in Eq. 7.1, the partition function is given by

$$Z = \int \mathrm{d}[\psi^\dagger]\mathrm{d}[\psi] e^{-S[\psi^\dagger,\psi]/\hbar},$$

where the action is given by

$$S = \int_0^{\hbar\beta} \mathrm{d}\tau \int d^2\mathbf{k}\psi^\dagger(\mathbf{k}) \left(\hbar\frac{\partial}{\partial\tau} + \mathcal{H}_0(\mathbf{k})\right)\psi(\mathbf{k}).$$

In this expression, τ denotes imaginary time. Next, define $U_{\mathbf{k}}$, such that $D(\mathbf{k}) \equiv U_{\mathbf{k}}^\dagger \mathcal{H}_0(\mathbf{k}) U_{\mathbf{k}}$ is diagonal and unitary. $U_{\mathbf{k}}$ is called the *diagonalizer* of the Hamiltonian. For the full-band model it can only be determined numerically. The

diagonalizers induce a change of basis that is used later $\varphi(\mathbf{k}) = U\psi(\mathbf{k})$.

$$\varphi^\dagger_{\mathbf{k},\sigma} \equiv \left(c^\dagger_{\mathbf{k},\sigma,1}, c^\dagger_{\mathbf{k},\sigma,2}, \ldots, c^\dagger_{\mathbf{k},\sigma,2N-1}, c^\dagger_{\mathbf{k},\sigma,2N}\right), \tag{7.6}$$

where $c^\dagger_{\mathbf{k},\sigma,\alpha}$ ($c_{\mathbf{k},\sigma,\alpha}$) creates (annihilates) an electron with momentum $\mathbf{k}$, spin σ in energy band α. The Hamiltonian in Eq. (7.1) can be rewritten as

$$\mathcal{H}_0 = \sum_{\mathbf{k},\sigma} \varphi^\dagger_{\mathbf{k},\sigma} D(\mathbf{k}) \varphi_{\mathbf{k},\sigma}. \tag{7.7}$$

The Green's function is defined as $\langle \psi^\dagger(\mathbf{k})\psi(\mathbf{k})\rangle$, which is in fact equivalent to the inverse of the quadratic part of the action. After performing a Fourier transformation from imaginary time to Matsubara frequencies and neglecting spin, this results into

$$\begin{aligned}
G(i\omega_m, \mathbf{k}) &= \left[i\omega_m \mathbb{1} - \mathcal{H}_0(\mathbf{k})\right]^{-1}, \\
&= \left[i\omega_m \mathbb{1} - U_{\mathbf{k}} D(\mathbf{k}) U^\dagger_{\mathbf{k}}\right]^{-1}, \\
&= \left\{U_{\mathbf{k}} \left[i\omega_m \mathbb{1} - D(\mathbf{k})\right] U^\dagger_{\mathbf{k}}\right\}^{-1}, \\
&= U^\dagger_{\mathbf{k}} \left[i\omega_m \mathbb{1} - D(\mathbf{k})\right]^{-1} U_{\mathbf{k}}, \\
&= \sum_{s=1}^{2N} \frac{1}{i\omega_m - \xi^s_{\mathbf{k}}} U^\dagger_{\mathbf{k}} \Delta^s U_{\mathbf{k}},
\end{aligned}$$

where $\xi^s_{\mathbf{k}}$ are the diagonal entries of $D(\mathbf{k})$, which are the eigenenergies of the Hamiltonian, and Δ^s is a $2N \times 2N$ matrix with zero's everywhere, except for a 1 in the s^{th} entry along the diagonal. In other words, the sum over s is over the different energy bands. This Green's function is a $2N \times 2N$ matrix. The components correspond with sublattice index. Hence, the propagator between two different sites i and j is defined as

$$G_{ij}(i\omega_m, \mathbf{k}) = \sum_{s=1}^{2N} \frac{1}{i\omega_m - \xi^s_{\mathbf{k}}} \left(U^\dagger_{\mathbf{k}} \Delta^s U_{\mathbf{k}}\right)_{ij}.$$

Chapter 8

Conclusions

Throughout this thesis, various magnetic and electric phenomena in monolayer and multilayer graphene systems have been investigated. It was found that in monolayer graphene which is electron doped up to the saddle point in the band dispersion (van Hove singularity), there is a critical coupling at which a spin-density wave forms. Although there is a possibility for a ferromagnetic state at higher couplings (not confirmed), for all temperatures it is the case that a spin-density wave forms first if the interaction strength is increased. This result required calculations in very large meshes. If the mesh size is taken too small, wrong conclusions in favor of ferromagnetism prevail. Our result corrected a previous work in the field [106], which predicted a ferromagnetic ground state.

Next, the band dispersion of bilayer graphene with spin-orbit interactions was calculated. To the best of our knowledge, our work is the first that has included the effect of spin-orbit coupling in bilayer graphene. The intrinsic spin-orbit interaction opens a gap at the Dirac point, as it does for monolayer graphene, which is topological in nature. On the other hand, the Rashba interaction does not open a gap, but lifts the spin degeneracy of the bands and leads to a trigonal warping of the low-energy bands. The intrinsic spin-orbit coupling is expected to be small, but the Rashba spin-orbit interaction is tuneable. The latter interaction modifies one of the (spin-degenerate) parabolic bands at the K point into a cone. This cone is very robust when next-nearest-neighbor hopping parameters are added. Nevertheless, a bias voltage between the layers will open a gap in the spectrum and the cone will be destroyed.

For the low-doped graphene trilayer system it was investigated, through a variational approach, whether there exist a phase transition to a ferromagnetic phase due to the long-range Coulomb interaction. Because of the presence of a linear and parabolic band at the Dirac point in ABA-stacked trilayers, there are three variational parameters (filling parameters of the linear and parabolic bands in the spin up and spin down channels, constrained by particle number conservation) and the possibility of 'band-ferromagnetism' opens up. A ferromagnetic phase

transition was found to exist, but this is completely due to the parabolic bands. The number of electrons in the linear bands is much less than in the parabolic bands, due to higher cost in kinetic energy. The phase transition occurs at lower doping levels than in bilayer graphene.

This is different in ABC-stacked trilayers, where the critical doping levels for the ferromagnetic transition are about 25 times higher than for the bilayer. This factor of 25 is determined in a model that takes the screening of the Coulomb interaction into account in a simplified way. Although it is estimated that a more accurate inclusion of the screening does not change the results too much (less than 20%), it is interesting to determine the momentum dependence of the polarization. We derived integral expressions for the polarization in ABC-stacked multilayer graphene. In the two-band (low-energy) model, the short-wavelength limit is completely off. It is straightforward to compute the full-band polarization numerically, but it turns out to be a very time consuming calculation. However, it is known that the high-k limit of the polarization is linear and we obtained the slope for ABC-stacked trilayer. Below we review the main results of each Chapter in more detail.

Chapter 3 In Chapter 3, a Hubbard model was used to describe an interacting graphene monolayer with a Fermi energy, $E_F \sim t$. At this energy the band dispersion exhibits a saddle point at which the density of state diverges. This divergency is called a 'Van Hove singularity'. Moreover, at this electron doping, the Fermi surface is nested. In fact, there are three nesting vectors in reciprocal space that map the Fermi surface onto itself. The diverging density of states together with the nesting, lead to a diverging susceptibility. Although doping graphene to this high energies is challenging, recent progress shows that this regime is within reach through chemical doping of graphene [102]. Another approach is to lower the van Hove singularity in energy. This can be realized by intercalate gold clusters between graphene and a buffer layer [103], or by using twisted graphene layers [56]. We used to a path integral formalism to determine the susceptibility, which was defined in a way that it reacts on both the electric and the magnetic perturbations.

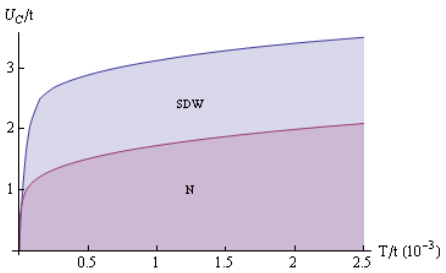

Figure 8.1: Temperature vs interaction strength phase diagram for monolayer graphene doped to the van Hove singularity

It is given by

$$\chi_{\mathbf{k}}^{r,r'}(i\hbar\Omega_n) = \frac{1}{N}\sum_{\mathbf{p},\alpha,\beta}\frac{n_F\left(\tilde{\epsilon}_{\mathbf{p}+\mathbf{k}}^{(\alpha)}\right) - n_F\left(\tilde{\epsilon}_{\mathbf{p}}^{(\beta)}\right)}{\tilde{\epsilon}_{\mathbf{p}+\mathbf{k}}^{(\alpha)} - \tilde{\epsilon}_{\mathbf{p}}^{(\beta)} - i\hbar\Omega_n} T_{\mathbf{p}+\mathbf{k},\mathbf{p}}^{r,r';\alpha,\beta},$$

$$T_{\mathbf{p}+\mathbf{k},\mathbf{p}}^{r,r';\alpha,\beta} = -\frac{1}{4}\mathrm{Tr}[P^r \mathcal{U}_{\mathbf{p}+\mathbf{k}} I^{(\alpha)} \mathcal{U}_{\mathbf{p}+\mathbf{k}}^\dagger P^{r'} \mathcal{U}_{\mathbf{p}} I^{(\beta)} \mathcal{U}_{\mathbf{p}}^\dagger].$$

This susceptibility is a matrix. A Stonerlike criterium states that an instability in the systems appears as soon as the (on-site) interaction is larger than one over the largest eigenvalue of this matrix. The eigenvalues are a function of momentum. Therefore, the criterium is first met at the peak value of the largest eigenvalue, corresponding with a certain momentum $\mathbf{Q}$. The eigenvector corresponding with this eigenvalue determines if a charge, spin, or combined instability is present. In graphene, the instability is always of magnetic nature. Since the peak value of the largest eigenvalue is located at a nonzero $\mathbf{Q}$, the instability is a spin-density wave. There is also a peak at $\mathbf{Q} = 0$, corresponding to a ferromagnetic instability, but this peak is always lower then the spin-density wave peak and is therefore always of subleading order. Although there is a possible ferromagnetic phase transition if the interaction parameter is large enough, we could not determine which phase the systems prefers above the upper solid line in Fig. 8.1.

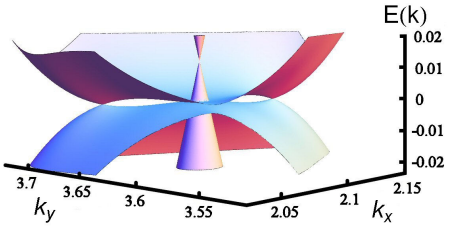

Figure 8.2: Energy dispersion of a graphene bilayer with Rashba spin-orbit interaction and next nearest neighbor hopping parameters.

Chapter 4 Fig. 8.2 shows the main result of Chapter 4. A tight-binding model was used to describe a graphene bilayer with spin-orbit interactions. The intrinsic spin-orbit coupling can effectively be described by a directional next-nearest-neighbor hopping. It conserves the spin of the electrons, but the sign is different, depending if the hopping is clockwise, or anti-clockwise around a honeycomb center. The intrinsic spin-orbit interaction opens a gap in the spectrum, as it does in monolayer graphene, where it causes the system to be in a topological nontrivial phase [78, 79]. The Rashba coupling manifests itself as a spin-flipping nearest-neighbor hopping term. Hence, it does not conserve spin and the spin degeneracy of the energy bands is lifted. Especially the low-energy bands close to the Dirac points are interesting. The parabolic band splits into a cone and a more complicated structure. The cone at the K point is spin polarized, but has a symmetry related partner at the K'

point. The slope of the cone, hence the velocity of the charge carriers, is tuneable by the strength of the Rashba interaction. The other band shows a structure usually associated with trigonal warping; one central cone at the former K point and three satellite points where the conduction and valence band touch. These satellite points are not conelike, but have a higher order crossing. Although a bias voltage opens a gap and destroys this energy dispersion, as long as the bias voltage is zero, the structure remains intact when next-nearest-neighbor hopping parameters from the Slonczewski-Weiss-McClure model are added. The cone is shifted by an on-site energy difference between sites which do have a neighbor in the opposite layer and sites who do not, but does not change shape. The satellite points of the other low-energy band do change, but they keep touching. The particle-hole symmetry-breaking term γ_4 shifts the crossing away from zero and the γ_3 parameter enhances the satellite structure and renders the crossing linear. The combined effect of γ_3 and the Rashba interaction is stronger than both of them separately.

Chapter 5 Next, the ferromagnetic phase transition due to the exchange interaction was studied in trilayer graphene. This phase transition was already analyzed for monolayer [153] and bilayer graphene [154] in the literature, but for trilayer graphene the phenomena is either much richer or more profound. In ABA-stacked trilayers, studied in Chapter 5, both a linear and a parabolic band are present around the K point. Therefore, there are both massless and massive quasi-particles around and the interplay between them allow for something we have dubbed 'band-ferromagnetism', i.e. a state in which the linear and parabolic band fill up differently. Although the electrons gain energy by aligning their spin, they can no longer be in the same momentum state and therefore have to occupy states

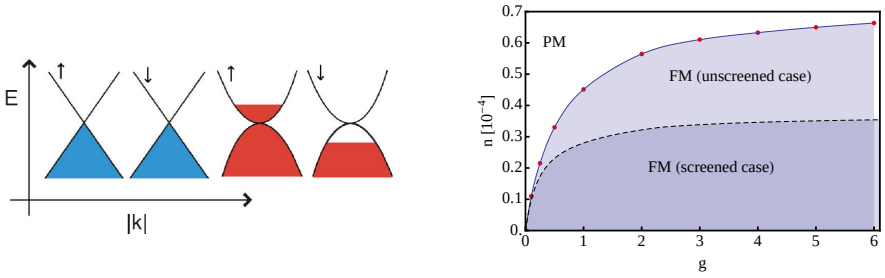

(a) (b)

Figure 8.3: (a) The electron-hole pocket configuration in the ABA-stacked trilayer. (b) Doping vs interaction phase diagram for the ABC-stacked trilayer. Below the solid (dashed) line, the unscreened (screened) system is ferromagnetic.

with higher kinetic energy. It depends on electron doping level and on interaction strength which state is favorable, the paramagnetic or the ferromagnetic state. To determine this, a variational approach was used in which the momenta to where the four bands around the K point (linear or parabolic and spin up or spin down) are filled was varied and the configuration of the parameters was found for which the total energy of the system minimizes. Naively, one would expect ABA-stacked graphene to behave as a combination of monolayer and bilayer graphene. This is only partially true. Although ferromagnetic configurations are found within the parabolic bands, with which is meant that both electron and hole pockets form in the spin-up and spin-down channels, the linear bands stay empty (within our resolution), as is sketched in Fig. 8.3a. The first-order phase transition around high coupling, $g = 5.3$, as seen in monolayers, is absent (for all practical purposes). The presence of the linear bands seems to suppress the ferromagnetic transition, because critical doping levels are around an order of magnitude smaller than in bilayer graphene.

Chapter 6 In Chapter 6 the same transition was investigated in ABC-stacked trilayer. Because the energy bands are much flatter than for bilayer graphene (cubic instead of parabolic), the kinetic energy cost of an electron or hole pocket is much smaller. Hence, one would expect that it would be favorable to align the electron spins in a wider range of the parameter space. Indeed, it is found (Fig. 8.3b) that the critical doping level at a fixed interaction strength is around 50 times larger than in bilayer graphene. This results were obtained numerically. Although there is only one variational parameter, compared to three in the ABA-stacked trilayer, it is no longer possible to diagonalize the Hamiltonian analytically. This is one of the reasons that the computations are very time consuming. It was realized that screening should be taken into account, because of the diverging density of states. The program (written by Richard Olsen) that was used to compute the exchange energy could not deal with the exact expression for the screening, because of divergences in the integrands. An approximation for the screening was used, in which we replace the polarization by a linear function, resulting in a renormalization of the coupling constant g. This approximation was justified by the fact that the polarization becomes linear for large momenta and we integrate over all momenta, hence this is expected to be the dominant part. An estimation of the error shows that the screened results are expected to be within 20 percent accuracy. Screening results reduce the critical electron doping levels by a factor of two, but they are still ~ 25 times higher than for bilayer graphene (see Fig. 8.3b).

Chapter 7 Although the results for the ABC-stacked trilayer are not expected to differ much when the screening is included in a more accurate way, the

determination of the polarization (and the screened potentials) in ABC-stacked trilayer graphene is interesting. In Chapter 7 we derived an expression for the polarization of an ABC-stacked N-layer graphene system. As an example, we determined the small and large momenta limits of the polarization for an ABC-stacked trilayer numerically. For the small-k limit, the effective two-band model could be used. It was shown that the short-wavelength limit of the bubble is completely wrong in the two-band model. Another complication with the two-band model is that all the physics takes place on the outer layers, hence when determining the screened potentials it does not make sense to talk about the potential $V_{12}(k)$ between the outer layers and the middle one. To determine the correct screened potential the full-band model needs to be used. Although this is straightforward to do, the computations are very time-consuming. We know however, that in the long-wavelength limit, $k \to 0$, the total polarization is proportional to the density of states and is correctly reproduced in the two-band model, while for large k the polarization becomes linear. For ABC-stacked trilayer graphene we determined the slope of the linear regime, which is independent of momentum, and drew a realistic sketch of the total polarization. The computation of the components of Π, the exact cross over between the small and large momenta regimes, and the determination of the dynamical part of the polarization are numerically very demanding and beyond the scope of this thesis.

Nederlandse samenvatting

Grafeen is het dunste materiaal wat er bestaat. Het is namelijk maar één atoom dik. Grafeen bestaat uit puur koolstof, net als diamant en grafiet; het materiaal dat in een potlood zit. Het verschil tussen diamant en grafiet is de manier waarop de koolstofatomen geordend zijn. Een koolstof atoom heeft vier elektronen beschikbaar om een (covalente) binding te vormen met elektronen van andere koolstofatomen. In diamant vormen alle vier de beschikbare elektronen de sterkste binding mogelijk (sigma-binding). De energetisch meest voordelige manier om dit te doen is door de koolstofatomen te ordenen als in Fig. 9.1.

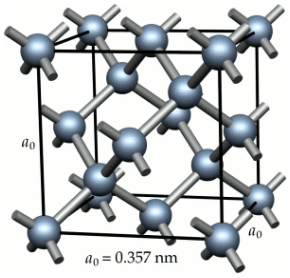

Figure 9.1: In diamant ordenen de koolstofatomen zich op deze manier. Bron: Ref. [186].

Dit is een driedimensionale structuur en omdat alle vier beschikbare elektronen in sterke sigma-bindingen zitten is diamant een elektrische isolator (geleidt geen stroom). In grafiet vormen slechts drie elektronen per koolstof atoom een sigma-binding en het vierde een veel zwakkere pi-binding. De sigma-bindingen bepalen de structuur van het koolstofrooster en in grafiet liggen deze in een vlak onder een hoek van 120° van elkaar. Daarom bestaat grafiet uit lagen koolstof die makkelijk van elkaar afglijden omdat ze slechts met de (zwakke) Vanderwaalskracht bij elkaar gehouden worden (zie Fig. 9.2a). Dit verklaart hoe een potlood werkt: Door grafiet op papier te drukken glijden er lagen koolstof van het grafiet af en hechten aan het papier. Binnen de lagen zijn de koolstofatomen geordend in een honingraatstructuur (zie Fig. 9.2b). Het elektron in de pi-binding is niet sterk gebonden aan een specifiek atoom en kan daarom rond bewegen door het materiaal. Grafiet is dus een geleider.

De gelaagde structuur van grafiet geeft aanleiding tot de vraag hoe dun dit materiaal gemaakt kan worden. In 2004 werd deze vraag voor eens en altijd beantwoord. Novoselov en Geim en hun groep in Manchester lieten zien dat het mogelijk is om grafiet één laag dun te maken. Een naam hiervoor was al in 1987 bedacht: grafeen.

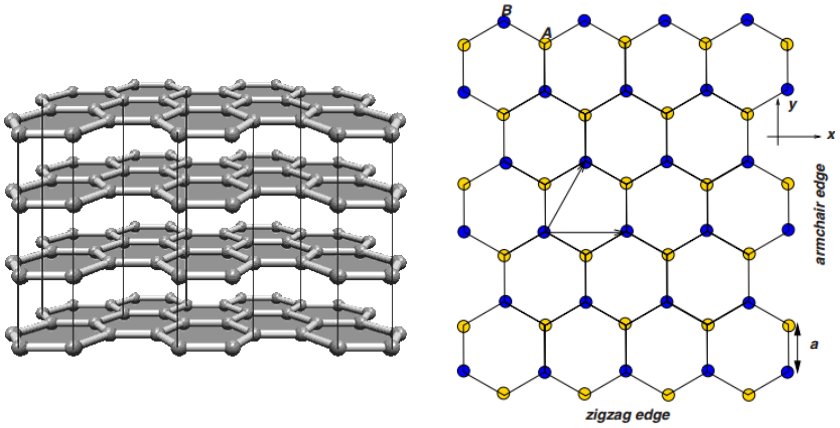

(a) (b)

Figure 9.2: a) Grafiet bestaat uit meerdere lagen grafeen op elkaar. Bron: Ref. [11]. b) De honingraatstructuur van het grafeen rooster. De gele en blauwe punten zijn geometrisch verschillend. Dit is te zien door naar de oriëntatie van de naaste buren te kijken. Bron: Ref. [10].

Voor het isoleren van grafeen kregen Novoselov en Geim al in 2010 de Nobelprijs. Dit is opmerkelijk snel. De methode waarmee ze grafeen produceerden, lijkt op het eerste gezicht vrij simpel. Ze gebruikten plakband om lagen van grafiet af te halen en herhaalden dit zo vaak totdat er een enkele laag overbleef. Dit klinkt misschien erg eenvoudig, maar er is één groot probleem met deze methode: Hoe zie je dat je grafiet zo dun is geworden dat het nog slechts één laag dik is? Met een 'scanning tunneling microscope' kan men de atomen van een materiaal zichtbaar maken. Echter, wanneer de de plakband-methode gebruikt wordt om grafeen te maken ontstaan er overal gebieden met meerdere lagen. De gebieden met grafeen zijn micrometers groot (0.0001 cm), terwijl het gebied waar je moet zoeken een vierkante centimeter is. Alsof je met een blinddoek om op handen en voeten op zoek moet naar een euro munt op een voetbalveld: een tijdrovend klusje en niet erg praktisch. De Nobelprijs werd dan ook niet alleen uitgereikt voor het maken van grafeen, maar ook voor het vinden van een makkelijke manier om het te identificeren.

Novoselov en Geim ontdekten dat als je de stukken grafeen en grafiet van het plakband op een substraat van SiO_2 overbrengt, het mogelijk is om grafeen met een normale (optische) microscoop te detecteren. Hierbij is het belangrijk dat het substraat de juiste dikte heeft. Een afwijking van 5% maakt het grafeen onzichtbaar. Grafeen absorbeert ongeveer 3% van het licht dat erop valt. Twee lagen grafeen op elkaar absorberen het dubbele, drie lagen het drievoudige, enzovoorts.

Op het juiste substraat geeft dit een erg goed contrast en is het eenvoudig om grafeen te identificeren (zie Fig.9.3).

Grafiet is niet het enige materiaal dat een gelaagde structuur heeft en nu de techniek bekend was, werd het ook mogelijk om andere systemen te maken van slechts één laag dik. Toch hebben deze nooit zoveel aandacht gekregen als grafeen. Dit valt te verklaren door de hoge kwaliteit van het geproduceerde materiaal. Zelfs grafeen dat geproduceerd wordt door middel van de plakband-methode heeft zeer goede elektronische eigenschappen. De elektronen hebben een hoge mobiliteit, wat betekent dat ze snel door grafeen kunnen bewegen onder invloed van een elektrisch veld. De hoge mobiliteit en goede geleiding van de elektronen in grafeen maakt het een veelbelovend materiaal om in elektronica te verwerken. Grafeen geleidt altijd een beetje stroom, terwijl halfgeleiders onder bepaalde condities elektrische isolatoren kunnen zijn. Dit zorgt voor problemen als je van grafeen transistors wilt maken. Niettemin heeft grafeen talloze (mogelijke) toepassingen. Vanwege de grote hoeveelheid licht die grafeen doorlaat kan het gebruikt worden in touchscreens. Deze schermen kunnen dan ook flexibel gemaakt worden. Een andere mogelijkheid zijn supersnel oplaadbare batterijen, die gebruikt zouden kunnen worden in elektrische auto's. Ook wordt er onderzoek gedaan naar grafeen als gevoelige sensor om bepaalde gassen te detecteren. Zelfs de problemen met de minimale geleiding kunnen nu worden omzeild en steeds betere transistors van grafeen komen beschikbaar. Het isoleren van één laag grafiet door Novoselov en Geim heeft dit allemaal in gang gezet. Onderzoekers hebben zich massaal op dit materiaal gestort en binnen tien jaar is enorm veel vooruitgang geboekt. De vele praktische mogelijkheden van grafeen hebben ongetwijfeld bijgedragen aan de snelle toekenning van de Nobelprijs .

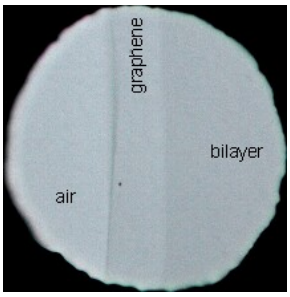

Figure 9.3: Grafeen kan optisch geïdentificeerd worden op het juiste substraat. Bron: Ref. [187].

Om de mogelijke toepassingen van grafeen te benutten is het nodig om grafeen op grote schaal te maken. Met de plakband-methode kunnen slechts stukken grafeen gemaakt worden die ongeveer een micrometer groot zijn. Dit zorgde ervoor dat grafeen in 2008 het duurste materiaal ter wereld was, toen het $\$100,000,000$ per cm^2 kostte. Sindsdien zijn er andere methodes ontwikkeld die grafeen op grotere schaal kunnen produceren. Het is mogelijk om koolwaterstoffen (meestal methaan) bij hoge temperaturen (1000° Celsius) neer te laten slaan op een substraat, gewoonlijk een metaal, waardoor zich een laag koolstof vormt (chemical vapor deposition). Op deze manier hebben wetenschappers in Zuid-Korea een vel grafeen geproduceerd met een diagonaal van 80 cm. Ook kan grafeen gepro-

duceerd worden op een siliciumcarbide (SiC) kristal. Hierbij wordt het SiC verhit tot $1200-2000^\circ$ Celsius, zodat het Silicium het kristal verlaat en er een laag grafeen boven op het kristal ontstaat. Deze productiemethodes maken het mogelijk om grafeen op een betaalbare wijze geschikt te maken voor praktische toepassingen.

Ondanks al deze praktische toepassingen, draagt een theoretisch fysicus meestal niet direct bij aan het produceren van touchscreens of het maken van grote vellen grafeen. Als theoreticus bestudeert men de eigenschappen van grafeen. Enerzijds om het experiment te verklaren, anderzijds om voorspellingen te doen die later in het experiment kunnen worden bevestigd. De wisselwerking tussen theorie en experiment leidt niet alleen tot concrete toepassingen, maar ook tot een beter begrip van de onderliggende fundamentele natuurkunde.

Ook voor de fundamentele natuurkunde is grafeen een heel bijzonder materiaal. Door de honingraatstructuur van het rooster (zie Fig. 9.2b), gedragen de elektronen zich uitzonderlijk. In een systeem met deeltjes bestaat er een relatie tussen het momentum van een deeltje en de energie die het deeltje heeft, de energie-momentum of dispersierelatie. Voor een klassiek en alledaags voorwerp, bijvoorbeeld een tennisbal, is het momentum (of impuls) proportioneel aan de snelheid. De energie die de bal heeft is gelijk aan $E = p^2/(2m)$, waar E de energie van de bal is, m de massa en p de impuls. Deze energie-momentum relatie is kwadratisch. In een kristal zijn atomen gelokaliseerd in een vast patroon. Als niet alle elektronen sterk gebonden zijn aan een specifiek atoom zijn er elektronen die van het ene naar het andere atoom kunnen bewegen. Het trillen van de atomen en de elektrische potentiaal die ze afgeven beïnvloed echter de elektronen. Gelukkig is het meestal zo dat de elektronen in een dergelijk systeem beschreven kunnen worden alsof de atomen er helemaal niet zijn, alsof ze vrij kunnen bewegen. Echter, de atomen hebben wel degelijk invloed en wanneer je net doet of ze er niet zijn moet er wel een prijs worden betaald: De energie-momentum relatie van de elektronen moet worden aangepast. Vaak is het zo dat de energie-momentum relatie weliswaar verandert, maar nog steeds kwadratisch is. Dat betekend dat de elektronen zich gedragen alsof ze een andere massa hebben. Dit heet de effectieve massa van de elektronen. In grafeen gebeurt iets bijzonders. De energie-momentum relatie van de elektronen is niet meer kwadratisch, maar lineair $E = v_F p$. Een lineaire dispersierelatie geldt ook voor fotonen (licht deeltjes). Omdat fotonen massaloos zijn concluderen we dat elektronen in grafeen zich gedragen alsof ze geen massa hebben. Massaloze deeltjes bewegen altijd met dezelfde snelheid. In grafeen is deze snelheid $v_F = 1,000,000$ m/s, wat 300 keer kleiner is dan de lichtsnelheid.

De dispersie van grafeen heeft dus de vorm van een kegel. Omdat er geometrisch twee verschillende rooster punten zijn (zie Fig. 9.2b), bestaan er ook twee verschillende energie banden: Een elektron met een zeker momentum kan twee verschillende energieën hebben. Deze twee energie banden worden de valentieband en de geleidingsband genoemd. Wanneer er net zoveel elektronen in het

systeem kunnen bewegen als dat er koolstofatomen zijn, is de valentieband volledig gevuld, terwijl de geleidingsband volledig leeg is (zie Fig. 9.4). Dit is een referentie toestand, waarbij de totale lading van het systeem nul is. Als er elektronen aan deze toestand worden toegevoegd komen die in de geleidingsband. Als er elektronen uit het systeem worden weggenomen, dan ontstaat er een gat in de valentieband. Hoewel een gat dus eigenlijk de afwezigheid van een elektron is gedraagt het zich als een deeltje met een tegenovergestelde lading als het elektron. Je kunt dus zowel over elektronen als over gaten praten. Als elektronen energie krijgen door bijvoorbeeld een foton, kunnen ze uit de valentieband in de geleidingsband terecht komen. Er wordt dan dus zowel een elektron als een gat gecreëerd.

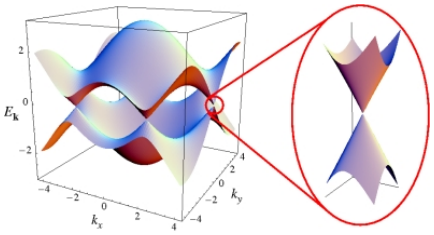

Figure 9.4: De volledige energie-momentum relatie van grafeen. Uitvergroot is het lineaire gedeelte. De band beneden het punt waar de twee kegels raken heet de valentieband en de band boven dit punt is de geleidingsband. Bron: Ref. [89].

Wanneer je lagen grafeen op elkaar stapelt krijg je uiteindelijk grafiet. De overgang naar grafiet gebeurt echter niet op het moment dat je een tweede laag grafeen op de eerste legt. Pas bij elf lagen grafeen verschilt de energie-momentum relatie minder dan tien procent met grafiet. Een systeem met enkele lagen grafeen gedraagt zich niet alleen heel anders dan grafiet, maar ook heel anders dan grafeen. Sterker, de eigenschappen van meerlaags grafeen hangen niet alleen af van het aantal lagen, maar ook van de manier waarop ze op elkaar gestapeld zijn. Meerlaags grafeen kan nog steeds beschreven worden als een tweedimensionaal systeem. Hoewel de elektronen kunnen bewegen tussen de verschillende lagen, ligt het momentum van de elektronen altijd in het vlak. De manier van stapelen bepaald de energie-momentum relatie van de elektronen.

Meerlaagse grafeen systemen worden niet gemaakt door het handmatig stapelen van lagen grafeen. Ze ontstaan bij experimenten. In de plakband-methode, bijvoorbeeld, ontstaan er naast enkele gebieden met grafeen, heel veel flarden meerlaags grafeen. Bij de andere productiemethodes kan het aantal lagen in meer of mindere maten gecontroleerd worden. Twee manieren van stapelen zijn energetisch voordelig en deze komen het meeste voor. Grafeen heeft drie punten van symmetrie, namelijk de twee verschillende rooster posities (de gele en blauwe punten in Fig. 9.2b) en het midden van de zeshoeken die door de roosterpunten gevormd worden. Wanneer men deze punten verbindt met elkaar, vormt dit een vlak met gelijkzijdige driehoeken. Wanneer lagen grafeen gestapeld worden moeten de punten van deze driehoeken boven elkaar komen te liggen. Wanneer je

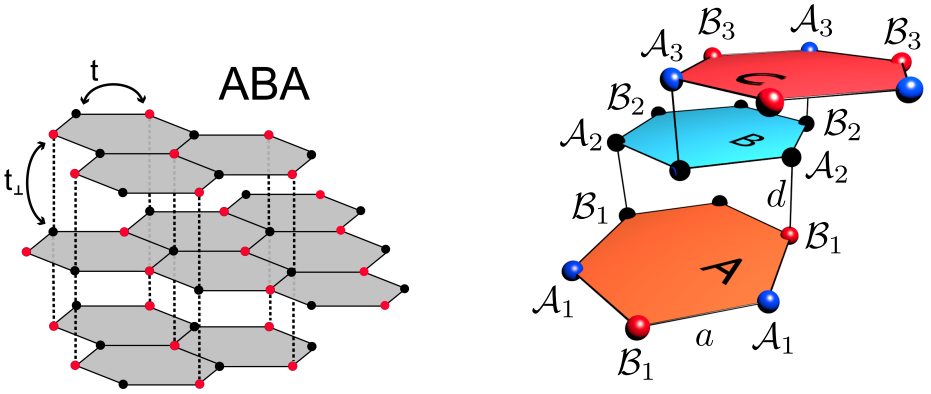

(a) (b)

Figure 9.5: (a) ABA gestapeld drielaags grafeen. (b) ABC gestapeld drielaags grafeen.

meerdere lagen grafeen hebt en de oriëntatie bekijkt van een bepaalde laag **ten opzichte van de onderste**, zijn er dus drie mogelijkheden.

- Mogelijkheid `A`: geel op geel, blauw op blauw, midden op midden.
- Mogelijkheid `B`: geel op blauw, blauw op midden, midden op geel.
- Mogelijkheid `C`: geel op midden, blauw op geel, midden op blauw.

Per definitie oriënteert de onderste laag zich als mogelijkheid `A`. Bij de fabricatie van meerlaagse grafeen systemen komen twee mogelijkheden het meeste voor. Systemen waar de lagen zich stapelen als `ABAB`..., dit heet Bernal stapeling of AB stapeling en systemen waar de lagen zich oriënteren als `ABCABC`..., dit rhombohedral stapeling of ABC stapeling. Voor een systeem met N lagen zijn er $2N$ energie banden (dispersierelaties). Voor Bernal gestapelde systemen zijn deze energie banden allemaal kwadratisch of lineair. De lineaire banden zijn alleen aanwezig als het systeem uit een oneven aantal lagen bestaat. In dit geval kunnen de elektronen zich zowel als massaloze en als massa-hebbende deeltjes gedragen. Voor ABC gestapelde systemen gaat de energie-momentum relatie als $E \sim p^N$. Dus, voor drie lagen ABC grafeen hangt de energie van de elektronen af van de derde macht van het momentum. Hier kun je niet spreken over een effectieve massa, omdat dit begrip enkel met een kwadratische energie banden geassocieerd wordt.

Er is nog één belangrijk ding nodig om de resultaten van dit proefschrift te begrijpen. De energie banden van grafeen zijn lineair zolang als de momenta van de elektronen klein is. Voor grotere momenta en grotere energieën ziet de energie-momentum relatie eruit als in Fig. 9.4. Meestal is enkel het lineaire deel nodig

voor een theoretisch model van het systeem. In dit proefschrift is echter in twee Hoofdstukken (Hoofdstuk 3 en Hoofdstuk 4) de volledige dispersie gebruikt.

In dit proefschrift heb ik (elektro-)magnetische eigenschappen van grafeen en van meerlaags grafeen onderzocht. Elektronen hebben een eigenschap die spin heet. Deze spin kan omhoog of omlaag wijzen en is eigenlijk een klein magnetisch moment. Spin is een kwantummechanische eigenschap van het elektron is. Hoewel het iets weg van een draaiing van het elektron om zijn eigen as, heeft het geen analogie in de klassieke natuurkunde. Het is een interne vrijheidsgraad van het elektron, die twee waardes kan aannemen. Voor een verzameling van elektronen zullen de spins willekeurig omhoog of omlaag wijzen en gemiddeld zullen er evenveel spin omhoog als spin omlaag elektronen zijn. Onder bepaalde omstandigheden kunnen de spins van de elektronen zich ordenen. Wanneer er meer spins omhoog wijzen dan omlaag zal het systeem magnetisch worden. Wanneer verdeling van spins overal hetzelfde is noemen we dit ferromagnetisme. Wanneer de gemiddelde spin periodiek over het oppervlak van het systeem fluctueert heet dit een spin dichtheidsgolf.

In Hoofdstuk 3 is onderzoek gedaan naar het ontstaan van spin dichtheidsgolven in één laag grafeen. De energie-momentum relatie in grafeen heeft een zadelpunt. Dit zadelpunt ligt precies tussen de twee punten in waar de valentieband en de geleidingsband elkaar raken in Fig. 9.4. De grafiek buigt hier in de k_y richting omhoog en in de k_x richting naar beneden. Wanneer er elektronen aan het systeem worden toegevoegd, zullen deze steeds hogere energieën krijgen, omdat twee elektronen niet in dezelfde toestand kunnen zitten (dit heet het Pauli exclusie principe). Als je genoeg elektronen toevoegt zullen ze een energie krijgen die correspondeert met het zadelpunt (de van Hove singulariteit). Op dit punt wordt de toestandsdichtheid oneindig groot (er zijn heel veel mogelijke toestanden met deze energie) en dit kan aanleiding geven tot een fase overgang. In principe zijn er verschillende fase overgangen mogelijk. Er kan een lading dichtheidsgolf vormen, of ferromagnetisme kan ontstaan. In Hoofdstuk 3 wordt echter aangetoond dat als de sterkte van de kracht tussen de elektronen toeneemt zich als eerste een spin dichtheidsgolf vormt. Deze spin dichtheidsgolf is voor alle temperaturen de dominante instabiliteit.

Het totale impulsmoment (draaiing) van een elektron bestaat uit het orbitaal impulsmoment (draaiing van het elektron om een atoom) en het spin impulsmoment. Het is mogelijk om orbitaal impulsmoment en spin impulsmoment uit te wisselen. Dit fenomeen heet spin-baanwisselwerking. In Hoofdstuk 4 hebben we onderzoek gedaan naar spin-baanwisselwerking in tweelaags grafeen. Er zijn twee soorten spin-baanwisselwerking in grafeen. De intrinsieke spin-baanwisselwerking opent een gat tussen de valentie en de geleidingsband. Dit was het geval voor één laag grafeen en wij hebben aangetoond dat dit effect ook in tweelaags grafeen

gebeurd. Het belangrijkste resultaat uit dit Hoofdstuk is echter dat de tweede soort spin-baanwisselwerking, de Rashba spin-baanwisselwerking, ervoor zorgt dat de spin-omhoog elektronen zich anders gedragen dan de elektronen met hun spin omlaag. Zoals hierboven besproken is de energie-momentum relatie in twee lagen grafeen kwadratisch. Echter, als de Rashba wisselwerking groot genoeg is, dan wordt de dispersie voor de helft van de elektronen lineair, terwijl voor de andere helft van de elektronen de valentieband en geleidingsband elkaar raken op vier verschillende punten, in plaats van één. Zelfs als het model verfijnd wordt door tweede orde processen mee te nemen (directe overgang van elektronen naar roosterpunten die niet naast elkaar liggen), blijft dit gedrag behouden. Wanneer er echter een voltage verschil tussen de twee lagen wordt aangebracht zal er een gat ontstaan tussen de valentieband en de geleidingsband en de lineaire dispersie verdwijnen.

In Hoofdstuk 5 en 6 is onderzocht of drielaags grafeen magnetisch kan worden. Wanneer twee elektronen hun spin in dezelfde richting hebben levert dit een energie winst op. Dit heet het *exchange mechanisme*. Omdat elektronen met dezelfde spin niet in dezelfde toestand kunnen zitten vanwege het Pauli exclusie principe, moet een van de twee elektronen een hogere kinetische energie krijgen. Wanneer de energie winst van het gelijk brengen van de spins groter is dan de extra kinetische energie die nodig is om dit te realiseren, dan zal het systeem magnetisch worden.

Zowel Bernal gestapeld als ABC gestapeld drielaags grafeen kunnen magnetisch worden onder de juiste omstandigheden. Omdat er in Bernal gestapeld drielaags grafeen zowel een kwadratische als lineaire energie band is zijn er meer exotische toestanden van het systeem mogelijk. We zien dat alleen de elektronen in de kwadratische energie banden hun spin in dezelfde orintatie brengen. Als het totaal aantal elektronen in het systeem een kritische grens overschrijdt dan gebeurd dit niet langer. Dit wordt veroorzaakt doordat de extra kinetische energie die nodig is om te voorkomen dat twee elektronen in dezelfde toestand zitten groter wordt naarmate er al meer elektronen in het systeem zitten, vanwege de kwadratische dispersie. In ABC gestapeld drielaags grafeen is de energie momentum relatie kubisch. Dit zorgt ervoor dat de extra kinetische energie die nodig is als twee elektronen hun spin hetzelfde richten kleiner is en dat het kritische aantal elektronen waarbij het magnetisme verdwijnt ongeveer 50 keer hoger ligt dan voor tweelaags grafeen, een systeem dat door anderen al eerder onderzocht was.

In ABC gestapeld grafeen divergeert de toestandsdichtheid als er precies één elektron per koolstof atoom in het systeem aanwezig is. De elektromagnetische kracht (Coulomb kracht) tussen twee deeltjes wordt beïnvloed door de aanwezigheid van andere geladen deeltjes (*screening*). Wanneer de toestandsdichtheid groot is zal de modificatie van de Coulomb kracht groter zijn. Omdat in grafeen en tweelaags grafeen de toestandsdichtheid begrensd blijft is screening minder belangrijk. Voor ABC gestapeld meerlaags grafeen moeten we dit effect echter meenemen. In Hoofdstuk 6 hebben we een versimpeld model voor de screening

gebruikt en hebben we aangetoond dat het kritisch aantal elektronen waarbij magnetisme verdwijnt ongeveer een factor twee kleiner wordt, maar nog steeds 25 keer groter is dan in tweelaags grafeen.

In Hoofdstuk 7 hebben we verder onderzoek gedaan naar screening in meerlaags ABC gestapeld meerlaags grafeen. Om de screening te bepalen moet men eerst de polarisatie berekenen. De polarisatie beschrijft onder andere hoe het systeem reageert op elektromagnetische verstoringen, maar wordt ook gebruikt om de afgeschermde potentiaal te berekenen in de *Random Phase Approximation* (RPA). Hoewel de formules voor de polarisatie vrij gemakkelijk zijn op te schrijven, is het niet zo eenvoudig om ze uit te rekenen. De polarisatie wordt gegeven door een integraal over momentum. Voor N-laags grafeen bestaat de integrant uit het product van $2N \times 2N$ matrices, die enkel numeriek kunnen worden bepaald. Zelfs voor maar drie lagen is dit zeer tijdrovend. Gelukkig is het mogelijk om voor kleine momenta een effectief model te gebruiken, waarin we de polarisatie snel numeriek kunnen bepalen. Voor grote momenta geeft deze benadering het verkeerde gedrag voor de polarisatie. We kunnen echter beargumenteren dat voor grote momenta de polarisatie lineair moet worden. Voor ABC gestapeld drielaags grafeen, hebben we via een directe, tijdrovende, berekening in dit gebied twee punten bepaald, waaruit we de helling van de polarisatie konden berekenen. Zo hebben we uiteindelijk een realistische schets voor de afgeschermde potentiaal kunnen maken, die gebruikt kan worden om effecten waarbij de Coulomb kracht in drielaags grafeen belangrijk zijn beter te beschrijven.

Dankwoord

Mijn promotie is er niet gemakkelijker op geworden sinds de eerste dag van mijn contract als promovendus. Deze eerste dag was namelijk een tweede pinksterdag en het echte leven als promovendus werd voor mij dus nog een dagje uitgesteld. Toen ik de dag erna dan toch aan de slag mocht ging het snel en nu, bijna vier jaar later, is mijn dissertatie bijna klaar. Er rest enkel nog dit dankwoord, zeker niet het gemakkelijkste gedeelte van deze thesis. Er zijn gedurende de afgelopen vier jaar vele mensen geweest die hebben bijgedragen aan de totstandkoming van dit proefschrift. Niet alleen via een directe bijdrage aan de inhoud van dit werk, maar zeker ook op indirecte wijze, zoals het mij laten uitrazen als die lange berekening niet bleek uit te komen.

The first person I want to thank is my supervisor Cristiane. I was very lucky to have you as a supervisor. You convinced me to change from high-energy physics to condensed matter, which turned out to be a very good decision. I appreciate your enthusiasm for physics, your interest in both what I was doing and how I was doing, and the advice you offered not only on work related matter, but also on issues outside the office. I value ~~all the presents that I have won at~~ your sinterklaas parties, which were always very much fun.

I am very grateful to the co-authors of the articles that form the basis for this thesis: Dima, Lih-King, Rafael, and Richard. It is very enjoyable to discuss a common physics problem together and our cooperation helped me to get a better insight of the physics. For the same reason I want to thank Wouter. Our discussions did not lead to a published paper yet, but the work we did about twisted bilayers can hopefully be used in the future. Also, I want to thank the other members of the group: Achilleas, Oliver, and Marco. Thank you for the fruitful comments on my work during group meetings and other gatherings.

Ik wil graag mijn collega's op het instituut bedanken. Het was altijd leuk om samen een biertje te drinken op de vrijdagmiddagborrel, te karten, te voetballen, maar ook om gewoon een praatje te maken. Door de jaren heen zijn er zoveel mensen gekomen en gegaan in het intituut dat het er teveel zijn om op te noemen. Toch wil ik enkele expliciet noemen. Ik wil Alice, Hedwig en Martijn bedanken

voor de gezellige lunches en pauzes en omdat ze naast collega's ook vrienden zijn (geworden). Dit geldt natuurlijk ook voor Jasper, maar ik moet jou toch even extra bedanken. Zonder jou had ik Lianne nooit ontmoet, als gevolg daarvan geen huis gekocht en misschien nog wel steeds op mijn studentenkamer gewoond. Dat is toch wel een extra bedankje waard. Bij dezen dus. Ook wil ik de administratieve staf bedanken, omdat zij degenen zijn die zorgen dat het instituut blijft functioneren, Biene, Els, Geertje, Joost, Marion, Olga, Riny en Wilma.

Ook buiten het instituut zijn er mensen die hebben bijgedragen aan deze thesis. Naast Jasper, wil ik ook Sander bedanken voor het zijn van mijn paranimf. Ik wil Marc bedanken voor het corrigeren van de Nederlandse samenvatting. Na 4 jaar alleen maar schrijven in het Engels bleek je hulp nodig. Ik bedank mijn vrienden die nog niet aan bod zijn gekomen voor steun en advies en natuurlijk voor alle leuke momenten die hielpen om te ontspannen van werk. Ook mijn ouders en zusje wil ik expliciet bedanken. Ik waardeer het dat jullie er altijd zijn als dat nodig is. Familie en vrienden die nog steeds geen idee hebben wat ik de laatste vier jaar heb gedaan raad ik trouwens aan om de Nederlands samenvatting eens te lezen.

Er mist nog één iemand die ik nog niet bedankt heb, maar waar ik de meeste dank aan verschuldigd ben. Lianne, ik wil je bedanken voor al het geduld dat je met mij hebt gehad de laatste jaren. Niet alleen was ik soms chagrijnig vanwege werk dat moeizaam verliep, ook heb ik veel bewondering voor de manier waarop je omging met andere lastige kwesties. Bovendien wil ik je bedanken voor het lezen en corrigeren van grote delen van dit proefschrift. Bedankt voor alles!

Bibliography

[1] K.S. Novoselov, A.K. Geim, S.V. Morozov, D. Jiang, Y. Zhang, S.V. Dubonos, I.V. Grigoriev, and A.A. Firsov, Science **306**, 666 (2004).

[2] L.D. Landau, Phys. Z. Sowjetunion **11**, 26 (1937).

[3] R.E. Peierls, Ann. I. H. Poincare **5**, 177 (1935).

[4] N.D. Mermin and H. Wagner, Phys. Rev. Lett. **17**, 22 (1966).

[5] N.D. Mermin, Phys. Rev. **176**, 250 (1968).

[6] K.S. Novoselov, D. Jiang, F. Schedin, T.J. Booth, V.V. Khotkevich, S.V. Morozov, and A.K. Geim, Proc. Natl. Acad. Sci. USA **102**, 10451 (2005).

[7] N. Garcia, Arxiv:cond-mat/0703515 (2007).

[8] A. Fasolino, J.H. Los, and M.I. Katsneldon, Nature Mater. **6**, 858 (2007).

[9] J.C. Meyer, A.K. Geim, M.I. Katsnelson, K.S. Novoselov, T.J. Booth, and S. Roth, Nature **446**, 60 (2007).

[10] A.H. Castro Neto, F. Guinea, N.M.R. Peres, K. Novoselov, and A.K. Geim, Rev. Mod. Phys. **81**, 109 (2009).

[11] http://www.nano-enhanced-wholesale-technologies.com/images/structure-graphite.gif.

[12] A. Krishnan, E. Dujardin, M.M.J. Treacy, J. Hugdahl, S. Lynum, and T.W. Ebbesen, Nature **388**, 451 (1997).

[13] T.A. Land, T. Michely, R.J. Behm, J.C. Hemminger, and G. Comsa, Surf. Sci. **264**, 261 (1992).

[14] J.C. Schelton, H.R. Patil, and J.M. Blakely, Surf. Sci. **43**, 493 (1974).

[15] A. Nagashima, K. Nuka, H. Itoh, T, Ichinokawa, and C. Oshima, Surf. Sci. **291**, 93 (1993).

[16] F. Bonaccorso, Z. Sun, T. Hasan, and A.C. Ferrari, Nature Photon. **4**, 611 (2010).

[17] A.K. Geim and K.S. Novoselov, Nature Mater. **6**, 183 (2007).

[18] A.C. Ferrari, J.C. Meyer, V. Scardaci, C. Casiraghi, M. Lazzeri, F. Mauri, S. Piscanec, D. Jiang, K.S. Novoselov, S. Roth, and A.K. Geim, Phys. Rev. Lett. **97**, 187401 (2006).

[19] A. Gupta, G. Chen, P. Joshi, S. Tadigadapa, and P.C. Eklund, Nano Lett. **6**, 2667 (2006).

[20] Z.H. Ni, H.M. Wang, J. Kasim, H.M. Fan, T. Yu, Y.H. Wu, Y.P Feng, and Z.X. Shen, Nano Lett. **7**, 2758 (2007).

[21] F. Schedin, A. K. Geim, S. V. Morozov, D. Jiang, E. H. Hill, P. Blake, and K. S. Novoselov, Nature Mater. **6**, 652 (2007).

[22] J.-H Chen, C. Jang, S. Xiao, M. Ishigami, and M.S. Fuhrer, Nature Nanotech. **3**, 206 (2008).

[23] K.I. Bolotin, K.J. Sikes, Z. Jiang, M. Klima, G. Fudenberg, J. Hone, P. Kima, and H.L. Stormer, Solid State Comm. **146**, 351 (2008).

[24] E.V. Castro, H. Ochoa, M. I. Katsnelson, R. V. Gorbachev, D. C. Elias, K. S. Novoselov, A. K. Geim, and F. Guinea, Phys. Rev. Lett. **105**, 266601 (2010).

[25] P.J. Zomer, S.P. Dash, N. Tombros, and B.J. van Wees, Appl. Phys. Lett. **99**, 232104 (2011).

[26] K.S. Novoselov, A.K. Geim, S.V. Morozov, D. Jiang, M.I. Katsnelson, I.V. Grigorieva, S.V. Dubonos, and A.A. Firsov, Nature **438**, 197 (2005).

[27] J. Martin, N. Akerman, G. Ulbricht, T. Lohmann, J.H. Smet, K. von Klitzing, and A. Yacoby, Nature Phys. **5**, 144 (2008).

[28] Y.-M. Lin, C. Dimitrakopoulos, K.A. Jenkins, D.B. Farmer, H.-Y. Chiu, A.Grill, and P. Avouris, Science **5**, 327 (2010).

[29] Y. Zhu, L. Li, C. Zhang, G. Casillas, Z. Sun, Z. Yan, G. Ruan, Z. Peng, A.-R.O. Raji, C. Kittrell, R.H. Hauge, and J.M. Tour, Nature Commun. **3**, 1225 (2012).

[30] R. Mukherjee, A.V. Thomas, A. Krishnamurthy, and N. Koratkar, ACS Nano **6**, 7867 (2012).

[31] S. Bae, H. Kim, Y. Lee, X. Xu, J.-S. Park, Y. Zheng, J. Balakrishnan, T. Lei, H.R. Kim, Y.I. Song, Y.-J. Kim, K.S. Kim, B. Özyilmaz, J.-H. Ahn, B.H. Hong, and S. Iijima, Nature Nanotech. **5**, 574 (2010).

[32] A.H. Castro Neto, F. Guinea, N.M. Peres, Phys. World **19**, 33 (2006).

[33] M.I. Katsnelson, K.S. Novoselov, and A.K. Geim, Nature Phys. **2**, 620 (2006).

[34] T. Tudorovskiy, K.J.A. Reijnders, and M.I. Katsnelson, Phys. Scr. **T146**, 014010 (2012).

[35] Y. Zhang, Y-W Tan, H.L. Stormer, and P. Kim, Nature **438**, 201 (2005).

[36] K. S. Novoselov, Z. Jiang, Y. Zhang, S. V. Morozov, H. L. Stormer, U. Zeitler, J. C. Maan, G. S. Boebinger, P. Kim, A. K. Geim, Science **315**, 1379 (2007).

[37] X. Du, I. Skachko, F. Duerr, A. Luican, and E.Y. Andrei, Nature **462**, 192 (2009).

[38] K.I. Bolotin, F. Ghahari, M.D. Schulman, H.L. Stormer, and P. Kim, Nature **462**, 196 (2009).

[39] W. Yao, S.A. Yang, and Q. Niu, Phys. Rev. Lett. **102**, 096801 (2009).

[40] K.S. Sivudu and Y. Mahajan, Nanotech Insights **3**, 6 (2012).

[41] A.N. Obraztsov, Nature Nanotech. **4**, 212 (2009).

[42] A.N. Obraztsov, E.A. Obraztsova, A.V. Tyurnina, and A.A. Zolotukhin, Carbon **45**, 2017 (2007).

[43] K.S. Kim, Y. Zhao, H. Jang, S.Y. Lee, J.M. Kim, K.S. Kim, J.-H. Ahn, P. Kim, J.-Y. Choi, and B.H. Hong, Nature **457**, 706 (2009).

[44] A. Reina, X. Jia, J. Ho, D. Nezich, H. Son, V. Bulovic, M.S. Dresselhaus, and J. Kong, Nano Lett. **9**, 30 (2009).

[45] C. Mattevi, H. Kim, and M. Chhowalla, J. Mater. Chem. **21**, 3324 (2011).

[46] X. Li, W. Cai, J. An, S. Kim, J. Nah, D. Yang, R. Piner, A. Velamakanni, I. Jung, E. Tutuc, S.K. Banerjee, L. Colombo, and R.S. Ruoff, Science **324**, 1312 (2009).

[47] P.N. First, W.A. de Heer, T. Seyller, C. Berger, J.A. Stroscio, and J.-S. Moon, MRS Bulletin **35**, 296 (2010).

[48] W.A. de Heer, C. Berger, X. Wu, P.N. First, E.H. Conrad, X. Li, T. Li, M. Sprinkle, J. Hass, M.L. Sadowski, M. Potemski, and G. Martinez, Solid State Comm. **143**, 92 (2007).

[49] W.A. de Heer, C. Berger, X. Wu, M. Sprinkle, Y. Hu, M. Ruan, J.A. Stroscio, P.N. First, R. Haddon, B. Piot, C. Faugeras, M. Potemski, and J.-S. Moon, J. Phys. D: Appl. Phys. **43**, 374007 (2010).

[50] M. Sprinkle, J. Hicks, A. Tejeda, A. Taleb-Ibrahimi, P. Le Fvre, F. Bertran, H. Tinkey, M.C. Clark, P. Soukiassian, D. Martinotti, J. Hass, W.A. de Heer, C. Berger, and E.H. Conrad, Arxiv:1001.3869.

[51] C. Riedl, C. Coletti, T. Iwasaki, A. A. Zakharov, and U. Starke, Phys. Rev. Lett. **103**, 246804 (2009).

[52] D.V. Kosynkin, A.L. Higginbotham, A. Sinitskii, J.R. Lomeda, A. Dimiev, B.K. Price, and J.M. Tour, Nature **458**, 872 (2009).

[53] S. Pei and H.-M Cheng, Carbon **50**, 3210 (2011).

[54] I.-Y. Jeon, Y.-R. Shin, G.-J. Sohn, H.-J. Choi, S.-Y. Bae, J. Mahmood, S.-M. Jung, J.-M. Seo, M.-J. Kima, D.W. Chang, L. Dai, and J.-B. Baek, PNAS **109**, 5588 (2012).

[55] M. Koshino and E. McCann, Phys. Rev. B **87**, 045420 (2013).

[56] G. Li, A. Luican, J.M.B. Lopes dos Santos, A.H. Castro Neto, A. Reina, J. Kong, and E.Y. Andrei, Nature Phys. **6**, 109 (2009).

[57] K.S. Novoselov, E. McCann, S.V. Morozov, V.I. Fal'ko, M.I. Katsnelson, U. Zeitler, D. Jiang, F. Schedin, and A.K. Geim, Nature Phys. **2**, 177 (2006).

[58] E. McCan and V.I. Fal'ko, Phys. Rev. Lett. **96**, 086805 (2006).

[59] M.O. Goerbig, Arxiv:0909.1998. Lecture notes for the Singapore session "Ultracold Gases and Quantum Information" of Les Houches Summer School, 2009.

[60] E.V. Castro, K.S. Novoselov, S.V. Morozov, N.M.R. Peres, J.M.B. Lopes dos Santos, J. Nilsson, F. Guinea, A.K. Geim, and A.H. Castro Neto, Phys. Rev. Lett. **99**, 216802 (2007).

[61] M. Koshino and E. McCann, Phys. Rev. B **80**, 165409 (2009).

[62] L. Zhang, Y. Zhang, J. Camacho, M. Khodas, and I. Zaliznyak, Nature Phys. **7**, 953 (2011).

[63] J.W. McClure, Phys. Rev. **108**, 612 (1957).

[64] J.C. Slonczewski and P.R. Weiss, Phys. Rev. **109**, 272 (1958).

[65] E. McCann and M. Koshino, Phys. Rev. B **81**, 241409(R) (2010).

[66] M. Koshino and E. McCann, Phys. Rev. B **83**, 165443 (2011).

[67] Chun Hung Lui, Zhiqiang Li, Kin Fai Mak, Emmanuele Cappelluti, and Tony F. Heinz, Nature Phys. **7**, 944 (2011).

[68] B. Partoens and F.M. Peeters, Phys. Rev. B **74**, 075404 (2006).

[69] P. B. Visscher and L. M. Falicov, Phys. Rev. B **3**, 2541 (1971).

[70] S.V. Morozov, K.S. Novoselov, F. Schedin, D. Jiang, A.A. Firsov, and A.K. Geim, Phys. Rev. B **72**, 201401(R) (2005).

[71] N. Levy, S.A. Burke, K.L. Meaker, M. Panlasigui, A. Zettl, F. Guinea, A. H. Castro Neto, and M. F. Crommie, Science **329**, 544 (2010).

[72] T. low and F. Guinea, Nano Lett. **10**, 3551 (2010).

[73] F. Guinea, M.I. Katsnelson, and A.K. Geim, Nature Phys. **6**, 30 (2010).

[74] P. Esquinazi, D. Spemann, R. Höhne, A. Setzer, K.H. Han, and T. Butz, Phys. Rev. Lett. **91**, 227201 (2003).

[75] O.V. Yazyev, Rep. Prog. Phys. **73**, 056501 (2010).

[76] R.R. Nair, M. Sepioni, I.-L. Tsai, O. Lehtinen, J. Keinonen, A.V. Krasheninnikov, T. Thomson, A. K. Geim, and I.V. Grigorieva, Nature Phys. **8**, 199 (2012).

[77] S. Konschuh, M. Gmitra, and J. Fabian, Phys. Rev. B **82**, 245412 (2010).

[78] C.L. Kane and E.J. Mele, Phys. Rev. Lett. **95**, 146802 (2005).

[79] C.L. Kane and E.J. Mele, Phys. Rev. Lett. **95**, 226801 (2005).

[80] B.A. Bernevig, T.L. Hughes, and Z.-C. Zhang, Science **314**, 1757 (2006).

[81] M. König, S. Wiedmann, C. Brüne, A. Roth, H. Buhmann, L.W. Molenkamp, X.-L. Qi, and S.-C. Zhang, Science **318**, 766 (2007).

[82] D. Makogon, R. van Gelderen, R. Roldán, and C. Morais Smith, Phys. Rev. B **84**, 125404 (2011).

[83] D. Makogon, I.B. Spielman, and C. Morais Smith, EPL **97**, 33002 (2012).

[84] R. van Gelderen and C. Morais Smith, Phys. Rev. B **81**, 125435 (2010).

[85] R. van Gelderen, L.-K Lim, and C. Morais Smith, Phys. Rev. B **84**, 155446 (2011).

[86] R. Olsen, R. van Gelderen, and C. Morais Smith, Phys. Rev. B **87**, 115414 (2013).

[87] O. V. Gamayun, Phys. Rev. B **84**, 085112 (2011).

[88] Ralph van Gelderen, Richard Olsen, and C. Morais Smith, Arxiv:1304.5501 (2013).

[89] http://faraday.fc.up.pt/cfp/Members/evcastro/figs/imag.jpg/view.

[90] P.R. Wallace, Phys. rev. **71**, 622 (1947).

[91] L.M. Zang, Z.Q. Li, D.N. Basov, M.M. Fogler, Z. Hao, and M.C. Martin, Phys. Rev. B **78**, 235408 (2008).

[92] E. McCann and M. Koshino, Arxiv:1205.6953 (2012).

[93] R. Kundu, Mod. Phys. Lett. B **25**, 163 (2011).

[94] S. Reich, J. Maultzsch, C. Thomsen, and P. Ordejón, Phys. Rev. B **66**, 035412 (2002).

[95] A.H. Castro Neto, F. Guinea, and N.M.R. Peres, Phys. Rev. B **73**, 205408 (2006).

[96] N.M.R. Peres, F. Guinea, and A.H. Castro Neto, Phys. Rev. B **73**, 125411 (2006).

[97] N.M.R. Peres, A.H. Castro Neto, and F. Guinea, Phys. Rev. B **73**, 195411 (2006).

[98] F. Zhang, B. Sahu, H. Min and A. H. MacDonald, Phys. Rev. B **82**, 035409 (2010).

[99] T. Taychatanapat, K. Watanabe, T. Taniguchi, P. Jarillo-Herrero, Nature Phys. **7**, 621 (2011).

[100] J. González, F. Guinea, and M.A.H. Vozmediano, Nucl. Phys. B **424**, 595 (1994).

[101] L. van Hove, Phys. Rev. **89**, 1189 (1953).

[102] J.L. McChesney, A. Bostwick, T. Ohta, T. Seyller, K. Horn, J. González, and E. Rotenberg, Phys. Rev. Lett. **104**, 136803 (2010).

[103] M. Cranney, F. Vonau, P.B. Pillai, E. Denys, D. Aubel, M.M.D. Souza, C. Bena, and L. Simon, EPL. **91**, 66004 (2010).

[104] For a comprehensive review of the van Hove scenario in the context of High-T_c superconductors, see: R.S. Markiewicz, J. Phys. Chem. Solids **58**, 1179 (1997).

[105] W. Kohn and J.M. Luttinger, Phys. Rev. Lett. **15**, 524 (1965).

[106] N. M. R. Peres, M. A. N. Araujo, and Daniel Bozi, Phys. Rev. B **70**, 195122 (2004).

[107] J. González, F. Guinea, and M.A.H. Vozmediano, Nucl. Phys. B **485**, 694 (1997).

[108] R. Roldán, M.P. López-Sancho, and F. Guinea, Phys. Rev. B **77**, 115410 (2008).

[109] T. Stauber, Phys. Rev. B **82**, 201404(R) (2010).

[110] B. Valenzuela and M. A. H. Vozmediano, New Journal of Physics **10**, 113009 (2008).

[111] C.A. Lamas, D.C. Cabra, and N. Grandi, Phys. Rev. B **80**, 075108 (2009).

[112] T. Wehling, E. Sasioglu, C. Friedrich, A. Lichtenstein, M. Katsnelson, and S. Blügel, Phys. Rev. Lett. **106**, 236805 (2011).

[113] M. Zarea and N. Sandler, Phys. Rev. B **79**, 165442 (2009).

[114] Y. Yao, F. Ye, X.-L. Qi, S.-C. Zhang, and Z. Fang, Phys. Rev. B **75**, 041401(R) (2007).

[115] M. Zarea and N. Sandler, Phys. Rev. Lett. **99**, 256804 (2007).

[116] S. Trickey, *Lecture Notes on Electronic States and Excitations on Nanostructures* (PASI School, Zacatecas, Mexico, 2007).

[117] J.C. Boettger and S.B. Trickey, Phys. Rev. B **75**, 121402(R) (2007).

[118] H. Min, J.E. Hill, N.A. Sinitsyn, B.R. Sahu, L. Kleinman, and A.H. MacDonald, Phys. Rev. B **74**, 165310 (2006).

[119] D. Huertas-Hernando, F. Guinea, and A. Brataas, Phys. Rev. B **74**, 155426 (2006).

[120] A.H. Castro Neto and F. Guinea, Phys. Rev. Lett. **103**, 026804 (2009).

[121] Yu. S. Dedkov, M. Fonin, U. Rudiger, and C. Laubschat, Phys. Rev. Lett. **100**, 107602 (2008).

[122] T. Ohta, A. Bostwick, T. Seyller, K. Horn, and E. Rotenberg, Science **313**, 951 (2006).

[123] J.B. Oostinga, H.B. Heersche, X. Liu, A.F. Morpurgo, and L.M.K. Vandersypen, Nature Mater. **7**, 151 (2007).

[124] E. McCann, Phys. Rev. B **74**, 161403(R) (2006).

[125] E.V. Castro, K.S. Novoselov, S.V. Morozov, N.M.R. Peres, J.M.B. Lopes dos Santos, J. Nilsson, F. Guinea, A.K. Geim, and A.H. Castro Neto, J. Phys.: Condens. matter **22**, 175503 (2010)

[126] F. Guinea, A.H. Castro Neto, and N.M.R. Peres, Phys. Rev. B **73**, 245426 (2006).

[127] Y. Zhang, T.-T. Tang, C. Girit, Z. Hao, M.C. Martin, A. Zettl, M.F. Crommie, Y.R. Shen, and F. Wang, Nature **459**, 820 (2009).

[128] M. Zarea, C. Büsser, and N. Sandler, Phys. Rev. Lett. **101**, 196802 (2008).

[129] S.A. Brazovskii, Zh. Eksp. Teor. Fiz. **68**, 175 (1975) [Sov. Phys. JETP **45**, 85 (1975)].

[130] T.D. Stanescu, B. Anderson, and V. Galitski, Phys. Rev. A **78**, 023616 (2008).

[131] T. Stauber, N.M.R. Peres, F. Guinea, and A.H. Castro Neto, Phys. Rev. B **75**, 115425 (2007).

[132] H.-A. Engel, E.I. Rashba, and B.I. Halperin, *Theory of Spin Hall Effects in Semiconductors*, Handbook of Magnetism and Advanced Magnetic Materials, (John Wiley & Sons Ltd, Chichester, UK, 2007).

[133] L.M. Malard, J. Nilsson, D.C. Elias, J.C. Brant, F. Plentz, E.S. Alves, A.H. Castro Neto, and M.A. Pimenta, Phys. Rev. B **76**, 201401(R) (2007).

[134] S.Y. Zhou, G.-H. Gweon, J. Graf, A.V. Fedorov, C.D. Sparau, R. D. Diehl, Y. Kopelevich, D.-H. Lee, S. G. Louie, and A. Lanzara, Nature Phys. **2**, 595 (2006).

[135] G. Grynberg, B. Lounis, P. Verkerk, J.-Y. Courtois, and C. Salomon, Phys. Rev. Lett. **70**, 2249 (1993).

[136] J.T. Stewart, J.P. Gaebler, D.S. Jin, Nature **454**, 744 (2008).

[137] E. V. Castro, N.M.R. Peres, J.M.B. Lopes dos Santos, A.H. Castro Neto, and F. Guinea, Phys. Rev. Lett. **100**, 026802 (2008).

[138] M. Koshino and E. McCann, Phys. Rev. B **81**, 115315 (2010).

[139] Hongki Min and A.H. MacDonald, Phys. Rev. B **77**, 155416 (2008). Hongki Min and A.H. MacDonald, Prog. Theor. Phys. Suppl. **176**, 227 (2008).

[140] F. Zhang, H. Min, M. Polini, and A. H. MacDonald, Phys. Rev. B **81**, 041402 (2010).

[141] O. Vafek and K. Yang, Phys. Rev. B **81**, 041401 (2010).

[142] S. Latil and L. Henrard, Phys. Rev. Lett. **97**, 036803 (2006).

[143] B.E. Feldman, J. Martin and A. Yacoby, Nature Phys. **5**, 889 (2009).

[144] R.T. Weitz, M.T. Allen, B.E. Feldman, J. Martin and A. Yacoby, Science **330**, 812 (2010).

[145] F. Freitag, J. Trbovic, M. Weiss and C. Schönenberger, Phys. Rev. Lett. **108**, 076602 (2012).

[146] A.S. Mayorov, D.C. Elias, M. Mucha-Kruczynski, R.V. Gorbachev, T.Tudorovskiy, A. Zhukov, S.V. Morozov, M.I. Katsnelson, V.I. Fal'ko, A.K. Geim, and K.S. Novoselov, Science **333**, 860 (2011).

[147] R. Nandkishore and L. Levitov, Phys. Rev. Lett. **104**, 156803 (2010).

[148] R. Nandkishore and L. Levitov, Phys. Rev. B **82**, 115124 (2010).

[149] I. Amidror, *The Theory of the Moiré Phenomenon*, Vol. I (Springer, London, 2009).

[150] W. Bao, L. Jing, J. Velasco Jr, Y. Lee, G. Liu, D.Tran, B. Standley, M. Aykol, S.B. Cronin, D. Smirnov, M. Koshino, E. McCann, M. Bockrath, and C.N. Lau, Nature. Phys. **7**, 948 (2011).

[151] M. Koshino and E. McCann, Phys. Rev. B **79**, 125443 (2009).

[152] A. Kumar, W. Escoffier, J.M. Poumirol, C. Faugeras, D.P. Arovas, M.M. Fogler, F. Guinea, S. Roche, M. Goiran, and B. Raquet, Phys. Rev. Lett. **107**, 126806 (2011).

[153] N.M.R. Peres, F. Guinea, and A.H. Castro Neto, Phys. Rev. B **72**, 174406 (2005).

[154] J. Nilsson, A.H. Castro Neto, N.M.R. Peres, and F. Guinea, Phys. Rev. B **73**, 214418 (2006).

[155] S. Das Sarma, S. Adam, E.H. Hwang, and E. Rossi, Rev. Mod. Phys. **83**, 407 (2011).

[156] Helin Cao, Qingkai Yu, Robert Colby, Deepak Pandey, C. S. Park, Jie Lian, Dmitry Zemlyanov, Isaac Childres, Vladimir Drachev, Eric A. Stach, Muhammad Hussain, Hao Li, Steven S. Pei, and Yong P. Chen, J. Appl. Phys. **107**, 044310 (2010).

[157] J. L. Tedesco, B. L. VanMil, R. L. Myers-Ward, J. M. McCrate, S. A. Kitt, P. M. Campbell, G. G. Jernigan, J. C. Culbertson, C. R. Eddy, Jr., and D. K. Gaskill, Appl. Phys. Lett. **95**, 122102 (2009).

[158] Kenjiro K. Gomes, Warren Mar, Wonhee Ko, Francisco Guinea, and Hari C. Manoharan, Nature **483**, 306 (2012).

[159] S. H. Jhang, M. F. Craciun, S. Schmidmeier, S. Tokumitsu, S. Russo, M. Yamamoto, Y. Skourski, J. Wosnitza, S. Tarucha, J. Eroms, and C. Strunk, Phys. Rev. B **84**, 161408(R) (2011).

[160] R. Ma, L. Sheng, M. Liu, and D.N. Sheng, Phys. Rev. B **86**, 115414 (2012).

[161] S. Bala Kumar and Jing Guo, Appl. Phys. Lett. **100**, 163102 (2012).

[162] Fan Zhang, Jeil Jung, Gregory A. Fiete, QIan Niu, and Allan H. MacDonald, Phys. Rev. Lett. **106**, 156801 (2011).

[163] Jia-An Yan, W. Y. Ruan, and M. Y. Chou, Phys. Rev. B **77**, 125401 (2008).

[164] Zhiqiang Li, Chun Hung Lui, Emmanuele Cappelluti, Lara Benfatto, Kin Fai Mak, G. Larry Carr, Jie Shan, and Tony F. Heinz, Phys. Rev. Lett. **108**, 156801 (2012).

[165] Fan Zhang, Dagim Tilahun, and A. H. MacDonald, Phys. Rev. B **85**, 165139 (2012).

[166] Kin Fai Mak, Jie Shan, and Tony F. Heinz, Phys. Rev. Lett. **104**, 176404 (2010).

[167] Jia-An Yan, W. Y. Ruan, and M. Y. Chou, Phys. Rev. B **83**, 245418 (2011).

[168] J. Borysiuk, J. Soltys, and J. Piechota, Nature **109**, 093523 (2011).

[169] Mikito Koshino, Phys. Rev. B **81**, 125304 (2010).

[170] We are using the letter a to denote both, the lattice constant and the valley degree of freedom, as it is usually done in the literature.

[171] Masatake Mori and Masaaki Sugihara, J. Comput. Appl. Math. **127**, 287 (2001).

[172] Michael G. Duffy, SIAM J. Numer. Anal. **19**, 1260 (1982).

[173] William H. Press, Saul A. Teukolsky, William T. Vetterling, and Brian P. Flannery, *Numerical Recipes*, Cambridge, 2007.

[174] Henrik Bruus and Karsten Flensberg, *Many-Body Quantum Theory in Condensed Matter Physics*, Oxford, 2004.

[175] There is a factor of $1/(2\pi)$ difference from the article of Gamayun, due to differing conventions of the Fourier transform.

[176] Richard Olsen, *Ferromagnetism in ABC-trilayer graphene*, Master's thesis (2012), http://web.science.uu.nl/ITF/Teaching/2012/Richard%20Olsen.pdf.

[177] D.-H Xu, J. Yuan, Z.-J Yao, Y. Zhou, J.-H Gao, and F.-C Zhang, Phys. Rev. B **86**, 201404(R) (2012).

[178] H. Min, E.H. Hwang, and S. Das Sarma, Phys. Rev. B **86**, 081402(R) (2012).

[179] F. Ghahari, Y. Zhao, P. Cadden-Zimansky, K. Bolotin, P. Kim, Phys. Rev. Lett. **106**, 046801 (2011).

[180] C.R. Dean, A.F. Young, P. Cadden-Zimansky, L. Wang, H. Ren, K. Watanabe, T. Taniguchi, P. Kim, J. Hone, K.L. Shepard, Nature Phys. **7**, 693 (2011).

[181] S. Yuan, R. Roldán, and M.I. Katsnelson, Phys. Rev. B **84**, 125455 (2011).

[182] D.C. Elias, R.V. Gorbachev, A.S. Mayorov, S.V. Morozov, A.A. Zhukov, P. Blake, L.A. Ponomarenko, I.V. Grigorieva, K.S. Novoselov, F. Guinea, and A.K. Geim, Nature Phys. **7**, 701 (2011).

[183] W. Bao, Z. Zhao, H. Zhang, G. Liu, P. Kratz, L. Jing, J. Velasco Jr., D. Smirnov, and C. N. Lau, Phys. Rev. Lett. **105**, 246601 (2010).

[184] E.H. Hwang and S. Das Sarma, Phys. Rev. B **75**, 205418 (2007).

[185] E.H. Hwang and S. Das Sarma, Phys. Rev. Lett. **101**, 156802 (2008).

[186] http://www.e6cvd.com/cvd/uploaded_files/diamond-conventional-unit-cell.gif

[187] http://upload.wikimedia.org/wikipedia/en/1/19/Graphene_visible.jpg.

Ralph van Gelderen

Curriculum vitae

I was born in on the eighth of June 1985 in Dordrecht. I grew up there and followed secondary school at the "Johan de Witt gymnasium". I have always had a broad interest, but was particulary attracted to the exact sciences. Therefore, I decided to attend the TWIN program at Utrecht University in 2003. This program gives the opportunity to obtain two Bachelor of Science degrees, one in physics and one in mathematics. After I wrote my bachelor thesis under supervision of prof.dr.ir. Henk Stoof, I obtained both of them in 2006 (*cum laude*). Next, I enrolled in the master of theoretical physics in Utrecht. After I completed my master thesis under supervision of prof.dr. Gerard 't Hooft in April 2009, I became a Master of Science. I made the switch from high-energy physics to condensed matter after I got an offer from prof.dr. Cristiane Morais Smith to work under her supervision as a PhD candidate. In June 2009 I started this project and this thesis shows the results of these last four years.